Research article

Time-domain Brillouin scattering for evaluation of materials interface inclination: Application to photoacoustic imaging of crystal destruction upon non-hydrostatic compression

Sathyan Sandeep [a], Samuel Raetz [a,*], Nikolay Chigarev [a], Nicolas Pajusco [a], Théo Thréard [a], Mathieu Edely [b], Alain Bulou [b], Andreas Zerr [c], Vitalyi E. Gusev [a,*]

[a] *Laboratoire d'Acoustique de l'Université du Mans (LAUM), UMR 6613, Institut d'Acoustique – Graduate School (IA-GS), CNRS, Le Mans Université, France*
[b] *Institut des Molécules et Matériaux du Mans (IMMM), UMR 6283, CNRS, Le Mans Université, France*
[c] *Laboratoire de Sciences des Procédés et des Matériaux (LSPM-CNRS UPR-3407), Université Sorbonne Paris Nord (USPN), Villetaneuse, 93430, France*

ARTICLE INFO

ABSTRACT

Time-domain Brillouin scattering (TDBS) is a developing technique for imaging/evaluation of materials, currently used in material science and biology. Three-dimensional imaging and characterization of polycrystalline materials has been recently reported, demonstrating evaluation of inclined material boundaries. Here, the TDBS technique is applied to monitor the destruction of a lithium niobate single crystal upon non-hydrostatic compression in a diamond anvil cell. The 3D TDBS experiments reveal, among others, modifications of the single crystal plate with initially plane-parallel surfaces, caused by non-hydrostatic compression, the laterally inhomogeneous variations of the plate thickness and relative inclination of opposite surfaces. Our experimental observations, supported by theoretical interpretation, indicate that TDBS enables the evaluation of materials interface orientation/inclination locally, from single point measurements, avoiding interface profilometry. A variety of observations reported in this paper paves the way to further expansion of the TDBS imaging use to analyze fascinating processes/phenomena occurring when materials are subjected to destruction.

1. Introduction

Laser-based photoacoustics has accumulated a rather long and fruitful history of applications in high pressure research, where the measurements of the minerals elasticity are required for developing a model of the Earth's structure based on the seismological data. This is mostly due to such well known feature of laser ultrasonics as an opportunity to characterize materials remotely in harmful conditions such as, for example, extremely high temperatures [1–3] or nuclear radiation [3–5]. High pressures are also harmful for the application of piezo-electrical ultrasound transducers in direct contact with the tested materials, as they would be mechanically modified and destroyed. Thus, the application of various opto-acousto-optic techniques for the generation and detection of the acoustic waves in materials under high pressure is a natural choice for their ultrasonic evaluation. This choice is particularly suited due to essential transparency of the diamond anvils, providing optical access to the sample compressed between them to high and extremely high pressures in diamond anvil cells (DACs) [6,7].

Ultrasonic waves can be monitored (generated and detected) in optically transparent materials in a DAC by transient laser grating technique, where the generation of the coherent ultrasound occurs via electrostriction mechanism, while the detection is via acousto-optic (photoelastic) effect [8–10]. Transient gratings can also monitor interface acoustic waves, when they are created at the interfaces of the transparent and opaque materials compressed in a DAC [11,12] where the generation of the ultrasound is caused by light absorption in opaque medium via one or another physical mechanism of photoacoustic (optoacoustic) conversion [13]. In opaque materials placed in a DAC, the incident pulsed nanosecond/sub-nanosecond laser radiation can generate not only coherent interface waves but also bulk coherent acoustic pulses (CAPs) at ultrasound frequencies, which are launched and propagate both in opaque and transparent materials [14,15]. The subsequent detection of the ultrasonic echoes provides information on the acoustic velocities in the material and its thickness as a function of pressure. Both longitudinal and shear acoustic wave propagation can be monitored.

Quite recently femtosecond to picosecond (fs to ps) laser pulses have started their applications in the high pressure photoacoustics [16–22]. Although they can be applied similar to sub-nanosecond pulses to

---

* Corresponding authors.
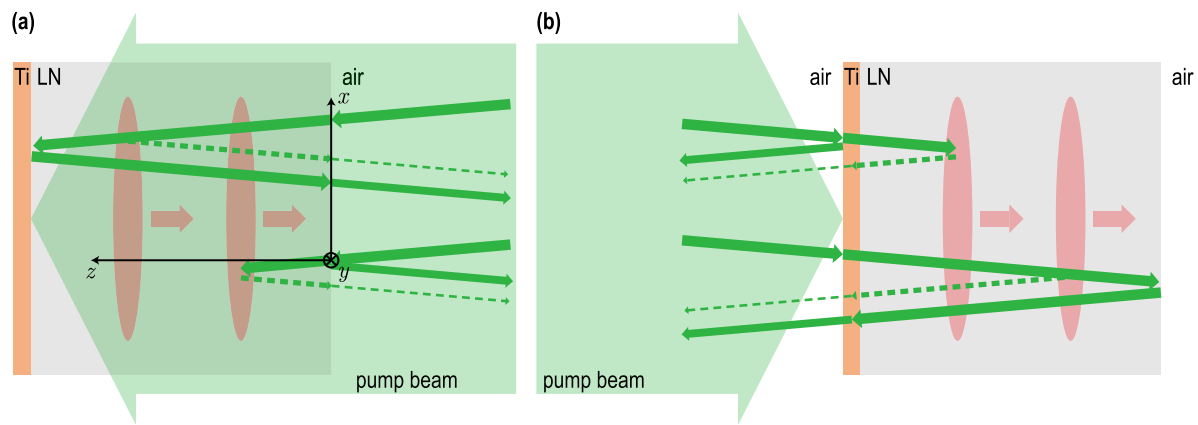*E-mail addresses:* samuel.raetz@univ-lemans.fr (S. Raetz), vitali.goussev@univ-lemans.fr (V.E. Gusev).

Fig. 1. Schematics of the pump and probe light paths in our time-domain Brillouin scattering experiments on free-standing lithium niobate, LiNbO$_3$ (LN), single crystal plate with the deposited thin Ti optoacoustic transducer for launching coherent acoustic pulses (CAPs) into the transparent crystal. The CAPs are depictured as semitransparent red ellipses. The pump and probe laser beams presented by thick continuous green rays, are incident on the same side of the sample. However, the experiments can be conducted from both sides of the sample, *i.e.*, from the LN side (a) and from the Ti side (b). Dashed green rays indicate weak scattering of probe light by the CAPs while continuous green rays also indicate stronger reflections of the probe light by stationary material interfaces of the sample. Only those reflected probe rays, which can interfere with the acoustically-scattered probe light, are presented. As followed from our experiments, the coherence length of the probe laser pulses in the LN crystal is about half of its thickness. Because of this, when the CAP propagates in the right or left half of the plate, it is detected due to heterodyning at the photodetector of the scattered light by the probe light reflected either by the LN/air interface or by the LN/Ti interface, respectively. Note that not only CAPs and pump light, but also probe light, propagate along the normal to the plate faces. The rays of the probe light are inclined in the figures only for convenience of their presentation. The pump light is presented as a wide beam, while probe light as a ray only for convenience; in experiments, the diameters of the pump and probe laser beams were equal.

generate CAPs and detect the echo arrivals, *e.g.*, in Refs. [17,19,22,23], their main additional feature is in the fact that the spectrum of ps acoustic pulses photo-generated by fs–ps pump laser pulses contains GHz frequencies and sub-micrometer wavelengths that could cause efficient Brillouin scattering of light, when the CAPs are propagating in the media transparent for probe laser pulses [24–26]. Thus, application of fs to ps laser pulses provides not only the opportunity to detect CAPs at their arrivals on the material interfaces, but, the most advantageous, to follow their propagation inside the transparent media. Fig. 1 illustrates the paths of the incident, reflected by the stationary interfaces and scattered by CAPs optical rays in a transparent crystal plate where the CAPs are generated via absorption of the pump laser pulses in the deposited metallic optoacoustic transducer. This figure illustrates our experiments conducted at ambient conditions, *i.e.*, at atmospheric pressure which results will be described below in Section 3.1.

In these ultrafast photoacoustic experiments, *i.e.*, with fs–ps laser pulses, the transient reflectivity of the probe laser pulse is measured as a function of the time delay of the probe pulse relative to the pump laser pulse. On the photodetector, the interference of the probe light scattered by the continuously moving CAP and the probe light reflected by the stationary interfaces of the sample takes place [24,25]. Linear-in-time phase shift between the scattered and reflected probe light, when a CAP propagates at constant velocity in a homogeneous medium, contributes to transient probe reflectivity signal as an oscillatory component composed of a single or several frequencies, corresponding to the Brillouin frequency shifts caused by inelastic scattering of probe light photons by acoustic phonons. Unlike classical frequency-domain Brillouin scattering [27], which involves probe light scattered by thermal phonons and its frequency shifts detected by spectrometers, the applied-here ultrafast photoacoustics employs coherent phonons, generated by pump light, to scatter the probe light. This results in the interference on the photodetector of the scattered and reflected probe light and the oscillations in the registered signal as a function of the time delay between the pump and the probe. Measurements based on these so-called Brillouin oscillations (BOs) in ultrafast transient reflectivity experiments are called picosecond acoustic interferometry [24, 25] or time-domain Brillouin scattering (TDBS) [26]. Measurements of the BO frequencies provide information on the product of acoustic velocities and refractive indices at the wavelength of the probe light. Amplitudes of the BOs depend on photoelastic constants which control

the strength of the Brillouin light scattering in the material. TDBS technique has been already applied for examination of liquids, *e.g.*, in Refs. [16,17], single crystals, *e.g.*, in Refs. [19,22], and polycrystalline solids, *e.g.*, in Refs. [17,18,28–31], compressed in a DAC. Fig. 2 presents a simplified schematic of paths of the pump and probe light in the sample volume in a DAC where a transparent lithium niobate, LiNbO$_3$ (LN), single crystal plate with the deposited metallic optoacoustic transducer is surrounded by water-ice VII, as was expected in our experiments conducted at P = 10.4 GPa. Results of these measurements will be presented in Section 3.2.

When, in these experiments, the laser-generated picosecond CAPs were arriving at the interface of two materials, they were partially reflected from the interface and partially transmitted through it. Generally, this event resulted in changes in both the amplitude and frequency of the BOs. These changes occurred because the amplitudes and propagation directions of the transmitted and reflected CAPs differed from those of the incident CAP, and the transmitted CAP propagated through a different material. These effects permit 1D localization, as shown for example in Refs. [32–35], 2D profilometry of the buried inclined interface depth (see [36] for example), and even 3D profilometry of interfaces [37–39], if the TDBS measurements are conducted in a single spatial position or with a scanning of the co-focused pump and probe laser beams along the sample surface in one or two directions, respectively. Obviously, performing TDBS-based measurements at several lateral positions provides information on the inclination of the interfaces. At high pressures, the observation of the TDBS signal modifications, accompanying CAP arrivals at material interfaces, has already been applied to the localization of the interface between the transparent sample and the diamond anvil, as reported, for example, in Refs. [18,20], and between two different water ice phases [20]. It has also been applied to 2D profilometry of the inclined interface between opaque and transparent media [20] and to the 3D-imaging of a sample of polycrystalline water ice containing two co-existing high-pressure phases [21].

Here, we apply the TDBS technique in order to monitor the degradation of a single crystal to polycrystal upon non-hydrostatic compression in a DAC. Our 3D TDBS imaging experiments reveal modifications of the thickness profile of the crystal with initially plane-parallel surfaces as well as of one of its faces profile caused by the non-hydrostatic compression. Moreover, our experimental observations, supported by
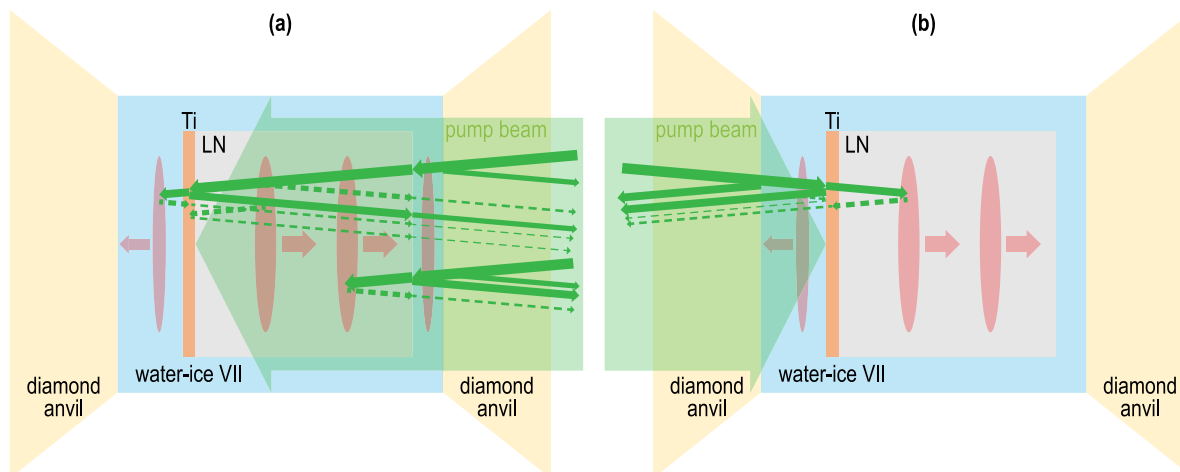
Fig. 2. Schematics of the pump and probe light paths in our TDBS experiments on a single crystal of LiNbO$_3$ (LN) covered on one side with the thin Ti optoacoustic transducer and surrounded by water-ice VII in a DAC. The pump and probe laser beams are incident through a diamond anvil and a water ice layer on the same side of the sample. However, the experiments can be conducted from both sides of the sample, *i.e.*, from the LN side (a) and from the Ti side (b). Dashed lines indicate weakly scattered probe light by CAPs that are depictured as semitransparent red ellipses. Solid lines indicate the incident pump and probe beams, as well as much stronger reflections of the probe light by stationary interfaces of the sample. We present optical paths of only the strongest reflected probe rays, which can interfere with the acoustically-scattered light and made detectable contributions to the TDBS signals in our experiments (Section 3.2). We also present only those scatterings of the probe light by CAPs which contributions to the TDBS signals were revealed in our experiments.

our theoretical interpretation, indicate that the TDBS imaging provides opportunity for the evaluation, in a DAC, of the materials interface orientation/inclination locally from single point measurements, *i.e.*, avoiding interface profilometry. We have observed that, depending on the local inclination of the buried interface, its spatial position can be revealed either through the modifications of the BOs in the absence of the detectable CAPs, or through the detection of the CAP echoes arrivals at the interface in the absence of BOs, or simultaneously through both features. Thus, the ratio of the CAP and BO amplitudes can be one of the parameters for the estimation of the local interface inclination/orientation relative to that of the diamond anvils, additional to the parameters related to the modifications of the BOs amplitude and frequency. By employing an analytical model and fitting the TDBS signals detected at a single lateral point, it becomes possible to simultaneously estimate both the depth position and inclination of the interface at that point.

The manuscript is structured as follows. In Section 2, the sample under study and the experimental setup are presented. In Section 3, the results of the TDBS experiments at atmospheric pressure are described (Section 3.1), followed by results of the measurements in a DAC upon several compression steps, preceding the crystal damage and, finally, the 3D TDBS imaging of the split LN-crystal at P = 10.4 GPa (Section 3.2). In Section 4, the recently developed theory of the TDBS for probe light and acoustic beams propagating at an arbitrary angle [40] is adapted to our experimental geometry to interpret our observations. Section 5 is devoted to the comparison of our experimentally observed TDBS signals with those reported earlier in various samples both at atmospheric pressure and compressed in DAC, to conclusions on our research results and the perspectives of the TDBS technique application to investigate materials destruction. Appendices A–E present not only the experimental parameters and the estimates of characteristic deformations of the crystal plate under loading, but also more details on some experimental observations, which are evidencing the single crystal destruction and spatial inhomogeneity induced by the non-hydrostatic loading of the sample in the DAC, which are just briefly mentioned in the main text.

2. Materials and methods

Investigation of destruction/failure of solid materials subjected to different types of mechanical loading is of high importance for the understanding of limits of functioning of the industrial devices employing these materials. Ferroelectric lithium niobate, LiNbO$_3$ (LN), is widely applied in acousto-electronics and in integrated and guided-wave optics because of its favorable elastic, optical, photoelastic, electro-optic, piezoelectric, and photorefractive properties [41]. Thus, the knowledge of resistance of solids having LN-type structure to mechanical stresses, which could be initiated by natural phenomena, such as earthquakes, tsunamis, nonuniform loading, is highly required in the information and communication technologies. Not surprisingly, there is also interest in the modifications of LN by shock waves, as discussed in Ref. [42] for example, and the properties of intact LN compressed to high hydrostatic pressures (see [43,44] and the references therein).

In contrast to the above research directions, here we are interested in investigating the degradation of an LN single crystal under gradually increasing non-hydrostatic compression/stresses. Such stresses develop in the solid Earth's interior upon its convection, leading to the tectonic plate motion and collisions released in the form of weak-to-disastrous earthquakes. Accordingly, degraded crystals of minerals transported to the Earth's surface can be used as records of the past tectonic events that occurred in the Earth's mantle. Similarly, texture and appearance of particular phases can be used to characterize the shock conditions in meteorites and different types of projectiles. For example, the LiNbO$_3$-type phase of Mg$_3$Al$_2$Si$_3$O$_{12}$ may be formed in shocked meteorites upon back-transformation from the high-pressure perovskite-type structure, and thus indicate the shock conditions around 45 GPa and 2000 K [45]. The presence of LiNbO$_3$-type phases of MgTiO$_3$ or FeTiO$_3$ as inclusions in superdeep diamonds [46] or in shock-melt veins after a meteorite impact [47] can be used to evaluate the P–T conditions of the origin and mineral environment of such diamonds or of the shock pressures during the impact. Permanent tensile stresses form also in neodymium doped MgO:LiNbO$_3$ crystal upon irradiation with femtosecond radiation of a Ti:sapphire laser used for the micropatterning of the crystal [48]. Such stresses can cause irreversible degradation of the crystal if subjected to temperature or stress gradients. Similarly, non-hydrostatic stress is harmful for piezoelectric ultrasound transducers in high pressure experiments in direct contact with the tested materials, as they would be mechanically modified and destroyed.

These are our motivations to perform experiments on visualizing the degradation of a LiNbO$_3$ single crystal, which is described in Section 2.1, to a polycrystal upon non-hydrostatic loading. In order to generate and control the degree of non-hydrostatic loading and to be able to monitor the single crystal degradation, we utilized a diamond
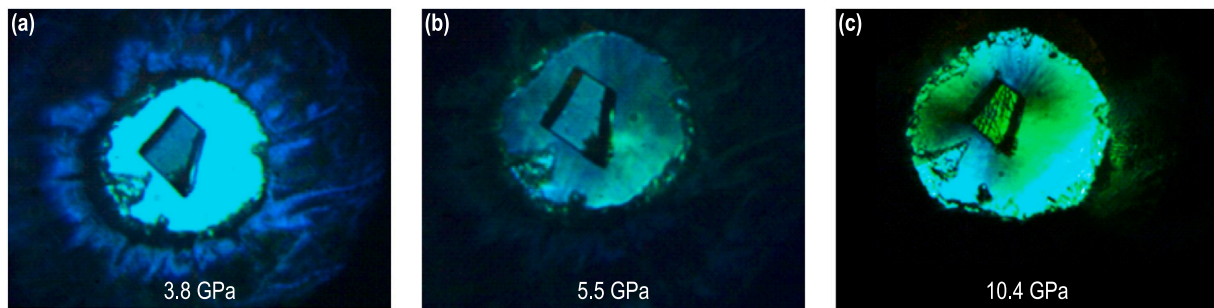
Fig. 3. Optical microscope images under white light illumination of the sample in the diamond anvil cell (DAC) from the lithium niobate, LiNbO$_3$ (LN), side, *i.e.*, right side in Figs. 1 and 2, as a function of increasing pressures, (a) 3.8 GPa, (b) 5.5 GPa, and (c) 10.4 GPa, revealing the destruction of the LN-sample at 10.4 GPa pressure.

anvil cell (DAC) [6], presented in Section 2.2, due to the following reasons: (i) the essential transparency of diamond anvils provides optical access to the sample compressed between them; (ii) application of pressure transmitting media of different rigidity permits variation of the uniaxial stress component acting on the single crystal (see [49] for example); (iii) embedding of the degrading crystal in a solid pressure medium in a DAC precludes falling apart of the crystal and thus preserves the cracks geometry. This insures also the full contact between the crystal parts and thus propagation of the acoustic and laser pulses through the crack boundaries which permits, accordingly, visualization of the crystal parts in the degraded state applying the opto-acousto-optic method of time-domain Brillouin scattering (TDBS), presented in Section 1, with the experimental setups described in Section 2.3.

2.1. Description of the LN single crystal sample

The single crystal of LN examined in this work was prepared from a nominally 20 μm-thick single-crystal disk (x-cut) of 722 mm in diameter. The supplying company (NanoLN, Jinan, China) specified the nominal surface roughness to be 1 nm for a 10 μm^2 surface providing the data on local measurements of surface height along a 3 μm-long line scan with points separated by 0.07 μm. The maximum variation of surface height between two neighbor points was 0.7 nm, providing the estimate of 0.6° for the maximum surface inclination at sub-μm scale. At the same time, the average height variation at about 1.5 μm distances did not exceed 0.5 nm. The averaged angle of the surface inclination of the delivered LN single crystal at the μm-scale hence did not exceed 0.02°. Therefore, at the spatial scale of the pump and probe laser foci in our experiments (1.25 μm radii at $1/e^2$ level of intensity), the average surface inclination was negligibly small while the surface roughness was much smaller than acoustic wavelengths in LN and water-ice VII (both larger than 100 nm at Brillouin frequency, see Section 3) and the wavelengths of the pump and probe laser beams (twice larger than acoustic wavelengths, Section 2.3). It could be concluded that the surfaces of the starting LN single crystal, *i.e.*, at atmospheric pressure, were of sufficiently high quality for the TDBS experiments.

The LN-disk was broken in smaller pieces and the one that matched the lateral dimensions of the sample volume of the used DAC was selected. The examined piece had the shape of a trapezoid (trapezium) with the width of about 40 μm and two parallel sides of approximately 30 μm and 20 μm (see the microscope image of the LN sample in the DAC in Fig. 3).

One side of the LN-crystal was coated with a 70 nm-thick Ti layer which served mostly as the optoacoustic generator in our TDBS measurements. The Ti layer was not completely opaque, but it exhibited a stronger reflection of the probe beam compared to the interfaces between transparent materials present in the sample volume such as LN/H$_2$O-ice or H$_2$O-ice/diamond. As will be explained below, this proves advantageous for the heterodyning of the acoustically-scattered probe light. Ti was chosen because of its acoustic impedance that matches perfectly that of LN, leading to a very small reflection of the CAPs at the Ti/LN interface of about 5% (for the CAP incident along the x-direction of our LN crystal). It also excluded the resonance ringing of the optoacoustic transducer, which could potentially bias the BOs if their frequencies were close to the frequencies of the Ti transducer eigenmodes. The densities and longitudinal acoustic velocities of LN and Ti ($\rho_{LN} = 4.628$ g/cm^3, $v_{LN} = 6.55$-6.57 μm/ns, which is the range found in the literature, $\rho_{Ti} = 4.506$ g/cm^3, $v_{Ti} = 6.070$ μm/ns) at atmospheric pressure were taken from [41,50,51] and pp. 12–40 and 14–41 in [52], respectively. Note that the density and the longitudinal acoustic velocity of Ti in our sample may differ from that considered in handbooks as our 70 nm-thick Ti layer might not be equivalent to bulk Ti. The reflection coefficient of the CAPs at the Ti/LN interface may hence deviate from the estimated 5% but will still remain small enough to avoid the resonance ringing of the Ti transducer.

2.2. Diamond anvil cell

In order to generate non-hydrostatic compression of our LN sample, we used a commercial DAC of the Boehler-Almax design with diamond anvils of type Ia exhibiting low fluorescence. The anvils had culets of 0.3 mm in diameter. The gasket was prepared from a 0.2 mm-thick steel disk pre-indented to the thickness of 40–50 μm. A hole of 120 μm in diameter, drilled in the center of the imprint, served as the sample volume. Prior to the sample loading, the whole gasket was processed for 30 min in O$_3$ atmosphere to improve the adhesion of water to steel, necessary for sample preparation. Then the LN single crystal was placed in the sample volume in contact with one of the diamond anvils, the remaining space was filled with water and the DAC was quickly closed, preventing the water leaking. Immediately after that, the pressure was increased to $P = 1.5$ GPa where water solidified to polycrystalline ice-VI. Pressure in the sample volume was monitored using the calibrated shift of the R1-fluorescence line of ruby micro-grains sticking to borders of the sample volume.

The pressure in the DAC was subsequently increased to $P = 3.8$ GPa, at which point the water ice had already transformed into its phase VII. Finally, the pressure was raised to $P = 10.4$ GPa. At the last step, fracturing of the LN crystal become visible in the optical microscope (Fig. 3). The fracturing could not be caused by bridging of the crystal between the diamond anvils because they were separated by 21.5 ± 0.5 μm. The latter was measured by optical ellipsometry at several places around the sample, where only transparent ice VII was present (Fig. 3). Moreover, the measurements did not reveal any inclination of the diamond anvils with respect to each other. This distance between the anvils was obtained using he refractive index of ice VII of $n = 1.63$ previously measured at high pressures in the wavelength interval of $\lambda = 540$–740 nm [53]. At the same pressure, the thickness of the LN crystal was estimated to be $H = 19.5$ μm which indicated diminishing,

with respect to that at the atmospheric pressure, H_0, by $\delta H/H_0 = 2.5\%$ (Appendix B). The nominal thickness of the LN-sample, *i.e.*, 20 μm, diminishes down to 19.5 μm. Thus, the LN crystal was separated from both diamond anvils (or at least from one of them) by a layer of water ice VII as shown in Fig. 2.

It is a subject of general knowledge that any liquid or gas compressed to sufficiently high pressure solidifies and, as any solid, it resists further change of its shape. This resistance is described through the value of the yield strength, σ_y, or hardness of the deformed material. Presently, a vast majority of the experiments in a DAC is performed on solids embedded in a soft (quasi-hydrostatic) pressure transmitting medium (PTM) exhibiting low σ_y such as solid helium, neon or argon. However, it is also possible to compress a sample non-hydrostatically in a DAC by "squeezing" it between the diamond anvils (*e.g.*, [54] and the references therein) or by embedding it in a PTM with a significant σ_y. In our experiments, we used liquid water as the PTM because it completely filled the sample volume around our LN crystal at atmospheric pressure without any voids. This precluded the sample damage upon initial compression and solidification of water to the high-pressure water ice VI phase. Upon further compression and transformation to water ice VII, this PTM became non-hydrostatic and started generating a uniaxial stress component which charged and finally damaged our LN single crystal at the average pressure of 10.4 GPa. Although our TDBS experiments conducted at this pressure (Section 3.2) revealed the presence of water-ice VII between the LN crystal and the diamond anvils in a dominant part of the sample, with a water-ice thickness extremely thin (few tens of nanometers at most) on one side of the LN sample (right side of LN in Fig. 2, see also below), the possibility of direct contacts between the non-coated LN sample surface and the diamond anvil in the experimental points with noisy or undetectable TDBS signals cannot be completely excluded. Undetectable or at the noise level TDBS signals are possible signatures of the direct LN/diamond contact/interface, leading to too weak probe light reflection for effective heterodyning of the acoustically-scattered light. Therefore, we believe that potentially both non-hydrostatic loading and the weak bending of the diamond anvil could have contributed to the splitting of the LN sample, development of the cracks and further degradation of the LN single crystal, ultimately leading to its polycrystalline state. Visualization of the resulting assembly of the $LiNbO_3$ grains is presented in Fig. 3(c) and below in Section 3.2.1 and Appendix D.

2.3. Ultrafast lasers setups

Two laser setups have been applied for the TDBS experiments on the LN sample. The first, preliminary, TDBS experiments in several isolated points (1D) or scanning along a line (2D) were always conducted using our pump–probe setup with a Ti:Sapphire laser and a mechanical delay line to achieve the time delayed of pump and probe pulses arrival at the sample location. Detailed description of this setup can be found in Ref. [18], with the only differences being that the laser pulse duration was shortened from 2.7 ps to 150 fs and that pump laser path was going through the mechanical delay line instead of the probe one.

More detailed final experiments in 1D, 2D, or 3D configurations, the latter corresponding to pump and probe foci scanning in 2D at the surface of the Ti generator, have been conducted using a commercial picosecond laser ultrasonics microscope (JAX-M1, Neta, Onto Innovation, Pessac, France) based on asynchronous optical sampling (ASOPS). Detailed description of this setup can be found in Ref. [21] and a summary of experimental parameters for each experimental condition described below is provided in Table A.2 in Appendix A.

3. Results of the TDBS experiments on lithium niobate plate: from a single crystal at atmospheric pressure to a fractured crystal at 10.4 GPa pressure

The data, accumulated in the conducted TDBS experiments, provide opportunity to reveal the influence of non-hydrostatic loading on the

LN state modification along the complete paths of the CAP in the sample, as earlier reported for transparent polycrystalline solids with depth inhomogeneity/texture, *e.g.*, in Refs. [18,28]. However, the accent in the research results presented below is on revealing the lateral and not depth inhomogeneity of the sample due to the crystal degradation, through the TDBS measurements/estimates of: (i) lateral variations of the sample thickness (thickness profilometry); (ii) Brillouin oscillation frequencies and amplitudes, averaged over the sample thickness; and (iii) surface inclinations of the parts of the split crystal relative to the diamond-anvil surfaces. Most of the experimental results presented below for the single point measurements or for the line scans were, first, documented with Ti:sapphire (blue pump/red probe) femtosecond laser setup (Section 2.3, Appendix C). However, in the main text, we present only the results which have been obtained later with the ASOPS-based JAX-M1 picosecond laser ultrasonics microscope (Section 2.3), which allows to get signals of higher signal-to-noise ratio in a shorter time of acquisition, thanks to the ASOPS technique. 3D TDBS images of the degraded crystal at $P = 10.4$ GPa have been obtained only with the JAX-M1 system, while the measurements at the intermediate pressures of 3.4 GPa and 5.5 GPa were accomplished only with the setup based on the Ti:sapphire laser. All the experiments at $P < 10.4$ GPa were conducted from the LN side of the sample as depicted in Fig. 2(a).

3.1. Basic features of the TDBS signals in the free-standing LN crystal at atmospheric pressure (P = 1 atm.)

The first experiments at $P = 1$ atm. ≈ 0 GPa were single point measurements, *i.e.*, 1D or depth profiling experiments, conducted with varying the polarization of the probe light (Fig. 4). They have confirmed that, in the x-cut LN, it is possible to detect, in the time domain, regular modulations of the BOs amplitude (Fig. 4(a)) due to the interference of up to three different Brillouin frequencies (BFs) (Fig. 4(b)), caused by the propagation of the longitudinal CAP in the direction of the LN optical birefringence [55].

In comparison with TDBS experiments in thick (half space) LN crystals in [55], our TDBS signals in the sample of finite thickness indicate the return of the launched CAP to the Ti transducer after the reflection at the LN/air interface, via the presence of a local minimum in the BOs amplitude around 5.8 ns time delay of the probe relative to the pump arrival. At the same time, even the zooming in the BOs around 2.93 ns time delay, where the CAP arrival at LN/air interface is expected, revealed an absence of any sharp local variations in the BOs amplitude, presumably due to high local parallelism of the opposite surfaces of LN sample (see Section 4 for the detailed theoretical interpretation of the experimental observations) and a weak scattering of the incident CAP by the low roughness of the LN crystal, both preventing an abrupt diminishing in the BOs amplitude. Broad peak around 2.9 ns was revealed only by an evaluation of the BO frequency dependence on time via time–frequency analysis with a continuous wavelet transform employing a Morlet wavelet with a time resolution of 3 BOs cycles (inset in Fig. 5(c)).

The lateral homogeneity of the LN sample has been evaluated by 2D TDBS measurements, *i.e.*, by conducting a 1D scan of the sample along a straight line at 12 points separated by 2 μm and by collecting each time a TDBS signal. The 12 signals are shown in Fig. 5(a) and the corresponding power spectrum densities in Fig. 5(b). At a first glance, both the TDBS signals and their power spectrum densities seem the same, confirming the lateral homogeneity of the LN sample.

In Fig. 5(d), the zoom in of the signals around 5.856 ns time delay, time of the CAP return to the Ti transducer, yet reveals the shift of the arrival times, *i.e.*, lateral variations in the sample thickness. The center of the time interval of about 0.02–0.03 ns in duration during which the BOs are smoothed provides a feature of CAP echo return to the transducer. This center shifts less than 0.01 ns along the 24 μm-long scan. In the literature, the reported values of the longitudinal acoustic velocities of 6.55–6.57 μm/ns [50,51] for the x-cut of LN
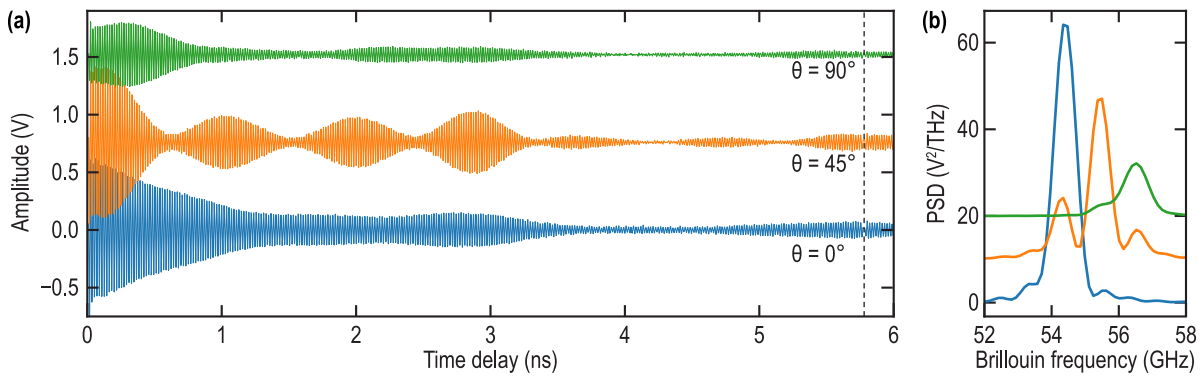
Fig. 4. (a) Acoustic parts of the relative reflectivity change (TDBS signals) obtained at different probe polarization angle θ after deletion of the transient non-oscillating decaying component, caused by transient heating of Ti and LN, via filtering between 10 and 150 GHz using a 6th-order Butterworth band-pass filter, and (b) their power spectral densities (PSD). The angle θ of probe polarization is at 0° when it is aligned with the optical axis of LN. In (a), the vertical dashed line indicates the CAP return to the Ti transducer, which indicates a weak damping of the CAP over this 40 μm-long propagation path in this high quality homogeneous sample. The signals in (a) and the PSD in (b) are vertically shifted to facilitate their comparison.
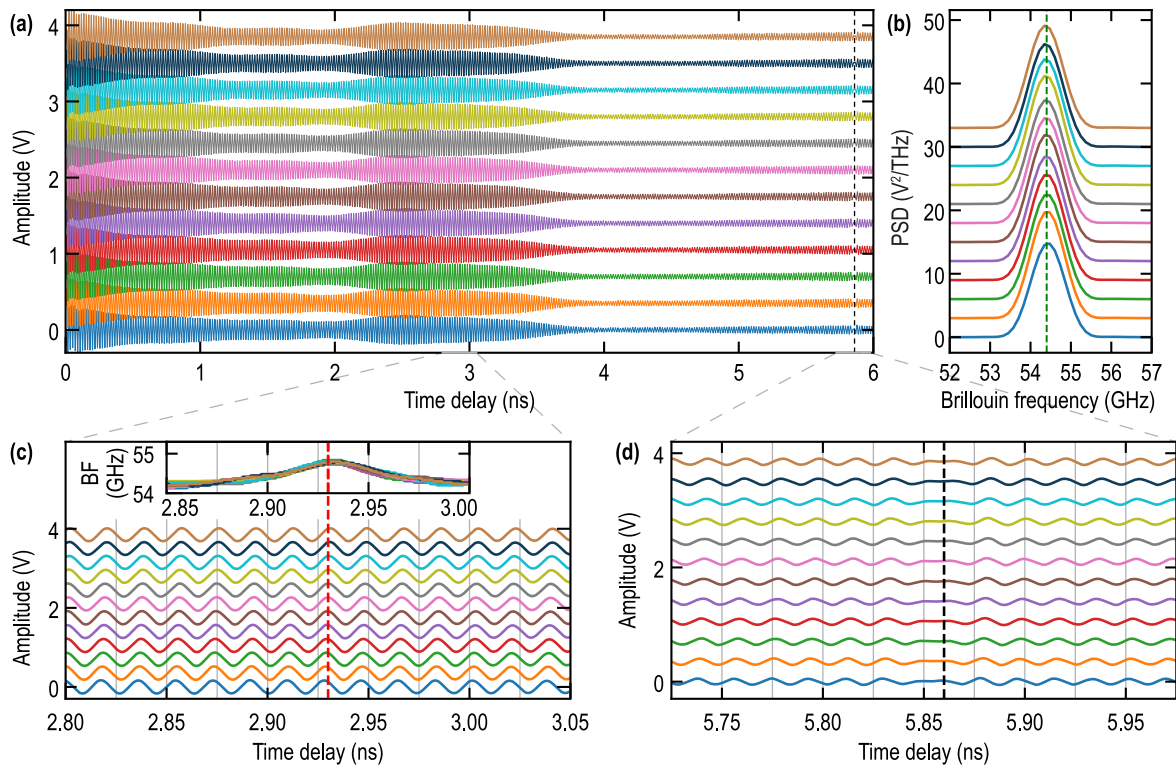

Fig. 5. (a) TDBS signals from the 1D scan (2D TDBS measurements) done at $P = 1$ atm. and (b) their power spectral densities (PSD). (c–d) Zoom in of the BOs around the expected time of the CAP arrival at the LN/air interface (c) and the CAP return at the LN/Ti interface (d). In (a) and (d), the vertical dashed lines indicate the CAP return to the Ti transducer. In (c), the red vertical dashed line indicates the time of CAP arrival at the LN/diamond interface, unresolved on the TDBS signals but revealed by the slight local increase in the Brillouin frequency (BF) around 2.93 ns in the time–frequency analysis results (inset). The signals in (a), (c) and (d), and the PSD in (b) are vertically shifted to facilitate their comparison.

allows to estimate the local thickness of the crystal and the inclination angle between its opposite surfaces. The estimated local thickness of 19.17–19.24 μm is about 4% smaller than nominal. In view of the well documented sound velocities in LN, we would use in the following the thickness of the sample measured by TDBS, *i.e.*, 19.2 μm, where the sample thickness is required in our estimates. The inclination angle of one face of the crystal relative to the opposite one is estimated

as 0.08°, while inclination of each of the faces relative to the mid-plane as 0.04°, which is comparable to the inclination at the microscale estimated earlier in Section 2.1 (0.06°), using the information from the LN supplier.

The BFs in the range from 54.4–56.5 GHz (Fig. 4(b)) correspond to longitudinal acoustic waves in x-cut LN of about $\lambda_{BO} \approx 0.12$ μm wavelengths. Then, for the radii of pump and probe laser beams in

our experiments ($a_{\text{probe}} = a_{\text{CAP}} \equiv a = 1.25$ μm at $1/e^2$ intensity level, Appendix A), the estimate of the diffraction length of these acoustic waves, which are efficient in Brillouin scattering, gives $l_{\text{diffr}}^{\text{ac}} \equiv \frac{\pi a^2}{\lambda_{\text{BO}}} \approx$ 40 μm, confirming that the BOs can be detectable even when the CAP propagates through the LN sample twice (see Figs. 4(a) and 5(a)). Note, that our experiments revealed that acoustic absorption/scattering at the Brillouin frequencies in LN did not prevent the detection of BOs at such long distances. At the same time, the diffraction length of the probe light is just twice shorter, because in the case of close-to $-180°$ backward Brillouin scattering [24–27] realized in our experimental geometry, the probe light wavelength in the medium is twice longer than acoustical Brillouin wavelength, $\lambda_{\text{probe}}/(2n) = \lambda_{\text{BO}}$. Using the middle BF from the above interval and the mean value, 6.56 μm/ns, of the longitudinal acoustic velocities for the x-cut of LN reported in the literature [50,51], the latter relation, provides opportunity to estimate the refractive index of LN for the green probe light with $\lambda_{\text{probe}} = 0.535$ μm to be $n_{\text{LN}}(P = 1$ atm.$) \simeq 2.26$, in good agreement with the earlier reported values of 2.23 to 2.33 for the extraordinary and ordinary refractive indices at atmospheric pressure, respectively [41, 56]. The knowledge of the probe light refractive index, of the duration of the probe laser pulses, $\tau_L \approx 130$ fs (Appendix A) and of the light speed in vacuum, c_0, permits the estimation of the probe coherence length, $l_{\text{coh}} = \frac{c_0 \tau_L}{2n_{\text{LN}}} \approx 10$ μm. At larger separation distances than l_{coh} between the CAP, scattering the probe light, and a stationary interface, reflecting the probe light for heterodyning the scattered light, the TDBS signals are significantly diminished because of the disappearing temporal overlap of the acoustically-scattered and reflected light at the photodetector [57]. Thus, the above estimates demonstrate that the coherence length of the probe laser pulses limits the imaging depths in the conducted experiments. As qualitatively presented in Figs. 1 and 2, because of the coherence requirements, the CAPs propagating in the left and right half of the LN crystal are detected due to the probe light reflected at left and right surfaces of the sample, respectively.

For a confident demonstration of the coherence length effect, the 2D TDBS measurements (see Fig. 5) have been conducted with a probe polarization preventing beatings in the BO amplitude by inducing a single optical mode propagation. Fig. 5(a) illustrates increase (maximum) in the BOs amplitudes when a CAP is approaching one of the crystal surfaces (at delay times of about 0, 2.9 and 5.8 ns) and decrease (minimum) when the CAP is close to the middle of the crystal (at delay times of about 1.45 and 4.35 ns)

3.2. Basic features of the TDBS signals upon fracturing/degradation of a single crystal of lithium niobate compressed non-hydrostatically in a DAC at 10.4 GPa

The experiments conducted on the LN crystal in a DAC at 10.4 GPa (Fig. 3(c)) have revealed several features of the TDBS signals that can be related to its degradation to a polycrystal. Note that, for the given sample thickness of 19.2 μm measured by TDBS in Section 3.1 at $P = 1$ atm., the linear shrinkage by 2.5% at $P = 10.4$ GPa (Appendix B) results in the thickness reduction to 18.7 μm, indicating that the total thickness of the water-ice layer(s) separating the sample from the diamond anvils (Fig. 2) could approach 3.1 ∓ 0.3 μm.

3.2.1. TDBS signals in the experiments conducted from the uncoated side of the LN crystal

The signals detected from the LN side, *i.e.*, when pump and probe are incident from the sample side free of the Ti transducer, denoted as the LN side in Section 1 (Fig. 2(a)), exhibit the major feature of the multi-frequency BOs in LN, similar to that at $P = 1$ atm., unless the polarization of the probe is tuned to avoid beatings between the BFs in LN. Apart from this similarity, the TDBS signals in the geometry of Fig. 2(a), *i.e.*, in the case of the LN crystal compressed in a DAC at 10.4 GPa, have features drastically distinguishing them from the signals in the geometry of Fig. 1(a), *i.e.*, in the case of the free-standing LN crystal.

For comparison with the results at $P = 1$ atm., shown in Fig. 5, we present in Fig. 6 the results of the similar 2D TDBS imaging experiment, *i.e.*, a lateral 1D scan along a line.

Fig. 6(a) demonstrates a lateral inhomogeneity of the fractured LN crystal as all the signals detected in different points are different one from another by one or several features, *e.g.*, the presence/absence of echoes and BOs in the time domain, the modulation of BOs in amplitude and the contribution of the BFs in LN to the complete spectra. Below, we list the features, distinguishing the 2D TDBS imaging signals in the experiments at $P = 10.4$ GPa (Fig. 6) from those at $P = 1$ atm. (Fig. 5) and we describe what is added to this comparison by the results of the subsequent 3D TDBS imaging at $P = 10.4$ GPa (Figs. 7 and 8).

a. Analysis of times of flight, averaged and local surfaces inclinations: The moments of the CAP arrival at the right face of the sample, after crossing the latter once, are easily distinguishable in Figs. 6(a) and (c) in most of the experimental points by the observation of the CAPs temporal profiles alone, *i.e.*, without BOs, or accompanied by abrupt variation in the amplitude of detectable BOs accompanying the CAPs. Further confirmations of this statement could be found in a variety of the temporal signals selected from the 3D imaging experiments results shown in Fig. 7.

We remind here that the profiles of the CAPs reflecting at the right face of the LN plate were not detectable at $P = 1$ atm. (Fig. 5(a)). The variation in the times of flight of the CAPs across the plate (once) between some of the neighbor points separated laterally by the 2 μm steps of the 2D TDBS measurements in Figs. 6(a) and (d) is larger than 0.05 ns. This variation is significantly larger than the ~ 0.01 ns CAP arrival times difference for twice the flying distance (back and forth in the sample) between the end points of the 24 μm-long scan at $P = 1$ atm. shown in Figs. 5(a) and (c). Thus, rough estimate indicates that the local inclination angle of one of the sample surfaces relative to the other one in the fractured crystal can be more than 100 times larger than in the intact single crystal. Two orders of magnitude increase in the inclination angle between the crystal plate faces is one of the most important fingerprints of the crystal fracturing in our experiments.

Our experimental observations provide opportunity for an even more precise estimate. The observable differences between the various complete signals in time domain in Fig. 6(a) are visible in the frequency domain as the differences in the dominant spectral lines in Fig. 6(b). Comparison of the spectra in Fig. 6(b) and Fig. 5(b) reveals lateral inhomogeneity of the fractured crystal. Although, the variations in the BF in 2D TDBS measurements could be attributed to several factors, including the variation in the direction of CAP propagation relative to the probe light direction [26,27], which can be caused by locally varying angle between the opposite faces of the fractured crystal parts (see Fig. 9 and theoretical Section 4), the average BF can be used for the estimate of the longitudinal acoustic velocity of x-cut LN at 10.4 GPa. Assuming that in average the experimental geometry is close to 180° backward Brillouin scattering, *i.e.*, as it is at $P = 1$ atm., the acoustical Brillouin wavelength $\lambda_{\text{BO}} = \lambda_{\text{probe}}/(2n)$ is not expected to change with the pressure increase to $P = 10.4$ GPa, because the first principles calculations indicate negligible deviation of the refractive index from its value at atmospheric pressure [43]. Therefore, the acoustic velocity increases with pressure proportionally to the measured BF. The maximal BF increases from 56.5 GHz in Fig. 4(b) up to 63.5 GHz in Fig. 6(b). Consequently, the sound velocity increases by 12.4% and reaches the values of 7.34–7.37 μm/ns. To our knowledge, this is the first ever reported measurement of acoustic velocity in LN at such a high pressure (see also Appendix C for the estimation of the acoustic velocity in LN at $P = 3.8$ GPa). For our current experimental estimates, this measurement provides opportunity to transform the maximum time difference between echo arrivals in two neighbor points in Fig. 6(c) (0.08 ns) into variation in plate thickness, 0.59 μm, and, finally, in the local inclination angle of 16° between the opposite surfaces, *i.e.*, about 8° inclination of the surfaces relative to the sample mid-plane.
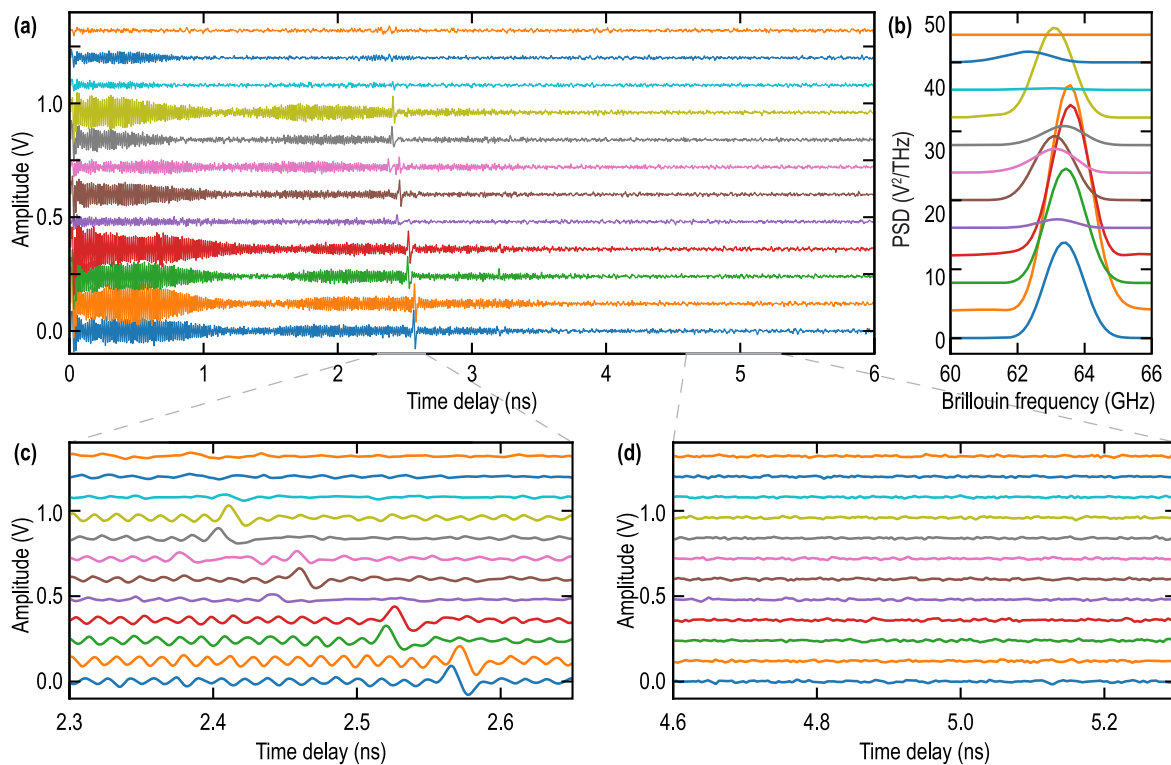
Fig. 6. (a) Acoustic parts of the TDBS signals from the 1D scan (2D TDBS measurements) done at $P = 10.4$ GPa and (b) their power spectral densities (PSD). (c–d) Zoom in of the BOs around the expected time of the CAP arrival at the LN/diamond interface (right side in Fig. 2(a)) (c) and the CAP return at the LN/Ti interface (d). Both BOs and CAP features are visible in (c), while it is not in (d). The signals in (a), (c) and (d), and the PSD in (b) are vertically shifted to facilitate their comparison.

The latter angle is 200 times larger than that estimated in the intact LN crystal at atmospheric pressure, a clear consequence of the crystal destruction.

These conclusions are confirmed by the map of the CAP arrival times obtained in the 3D imaging (Fig. 8(a)). Fig. 8(a) reveals that in the fractured sample the propagation time across its thickness can vary by a maximum of 0.5 ns or about 20%, corresponding to $\sim$ 3.7 μm variations in the sample thickness. These variations take place at about 30 μm lateral distances, providing opportunity to estimate the long scale average inclination between the faces of the fractured LN crystal to be of 7° which is just about twice smaller than the maximal local inclination revealed above in the 2D TDBS measurements. At the same time, the maximal local inclinations that can be estimated between the neighbor points of the 3D TDBS measurements are close to those revealed in the 2D TDBS measurements. Thus, 3D TDBS imaging confirms the strong inhomogeneity in the profile of the LN sample thickness. The related possible presence of large inclination angles between the opposite surfaces of the sample is an important signature of the LN crystal degradation/fracture.

b. Qualitative discussion of different features encountered in TDBS signals measured in the destructed LN crystal: The time moments of the CAP return to the Ti transducer after a round-trip in LN are not distinguishable in Figs. 6(a) and (c) of the 2D TDBS measurements, despite the observation of the abrupt changes in the BOs as it was possible in Fig. 5(a) and (c). Moreover, the BOs are not detectable in Fig. 6(a) and (c) in the left part of the LN sample, when the CAP returns there after the reflection. 3D TDBS imaging revealed that this is also the case in a largely dominant part of the signals detected over the complete surface of the fractured crystal in 3D images (Fig. 7(a)–(e)). Additionally, our 3D TDBS imaging confirmed that among these signals, those with BOs undetectable only after the return of the reflected CAP to the left part of the sample (Fig. 6(a)), are the most common (Fig. 7(a)), while the signals where the BOs are not detectable at all (the upper

signal in Fig. 6(a) and Fig. 7(b)), are rare. Importantly, the 3D imaging revealed another group of rather common signals, missed in the 2D TDBS measurements (Fig. 6(a)), where the BOs are detectable only in the left part of the sample and only when the CAP is traveling from the Ti transducer to the mi-plane of the sample (Fig. 7(c)–(e)). Note, that in Fig. 7(e) the BOs are detectable but not the CAP arrival on the right surface of the LN sample.

Another general conclusion on the results of the 3D imaging is that, in the fractured sample, the BOs were never observed after the return of the CAP to the Ti transducer, unlike the signals shown in Figs. 5(a) and (c) measured at atmospheric pressure in the intact sample. The signals, where the CAP return to the Ti transducer can be identified by an abrupt disappearance of the BOs, were detected in just several lateral positions (Fig. 7(f)). Additionally, only several lateral positions in the complete TDBS signals detected from the LN side present the feature caused by a second CAP traveling in the LN sample (Fig. 7(g)). To confirm that the features marked in Fig. 7(g) are indeed due to a second CAP, it is necessary to correlate each signal of this type measured from the LN side with the signal detected in the close lateral position from the opposite side of the sample (Section 3.2.2). This second CAP is indeed expected to be initially launched by the Ti transducer in the water-ice (Figs. 2(a) and 9) and transmitted into the LN sample only after the reflection at the water-ice/diamond interface and transmission across the Ti transducer, hence it should be also detectable from the opposite side. This correlation analysis is conducted below in Section 3.2.3.

Most of the different temporal signals detected in the fractured/degraded LN sample in the DAC, if not all, can be interpreted taking into account possible different local inclinations, relative to the diamond anvils, of the right and left faces of the LN sample, the latter being the Ti-coated one. In essence, the inclinations, revealed by the TDBS observations of the variations in the CAP times of flight, can lead to modification of the direction of the acoustically-scattered probe light relative to the direction of the reflected probe light heterodyning
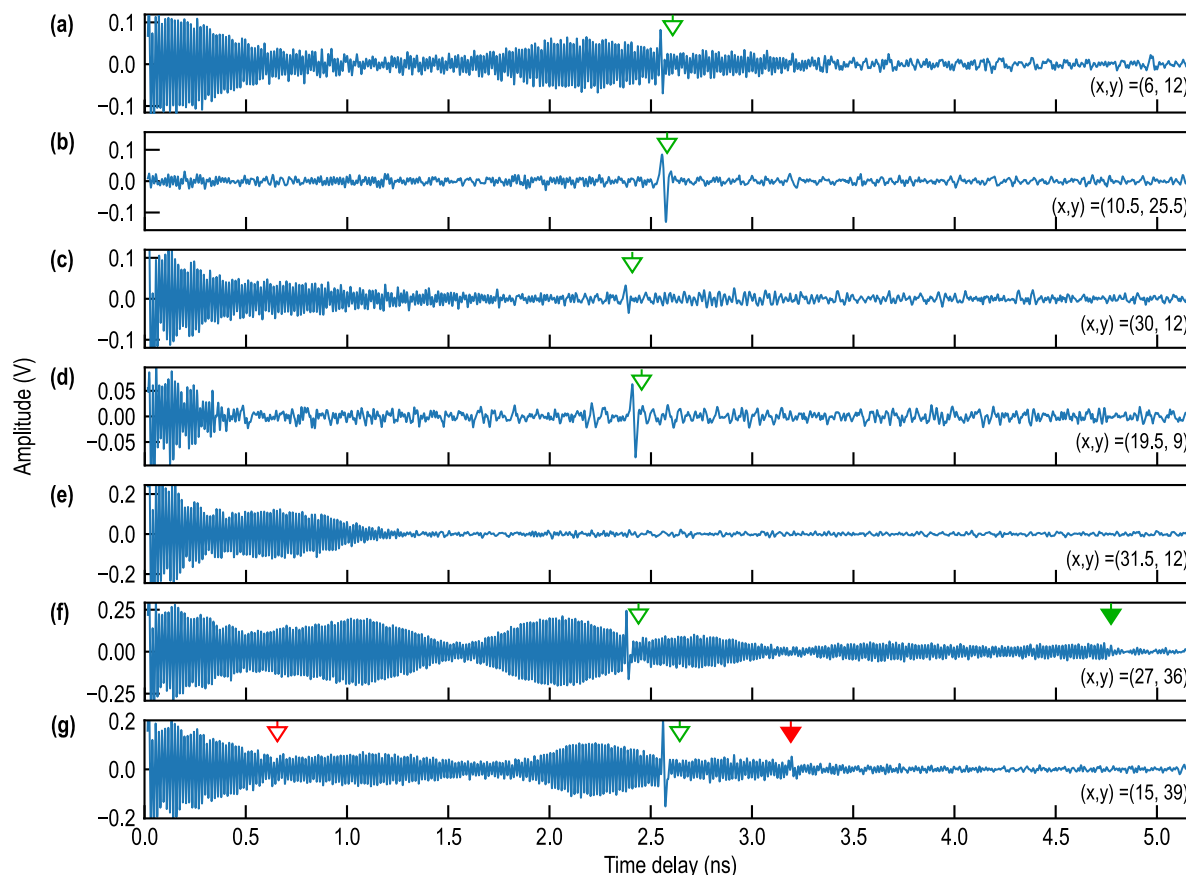
Fig. 7. Examples of shapes/forms of the TDBS signals in the fractured LN crystal sample. (a) Echo arrival on the uncoated face of the LN sample (marked here and later by a green empty arrow) is accompanied by the detectable BOs in the whole sample, when a CAP propagates from the Ti transducer to the right face of the sample, and only in the right part of the sample, after the CAP reflection. (b) Only the echo arrival without any BOs is detectable. (a) and (b) illustrate that the shapes of signals, which are the most typical to the 2D imaging signals in Fig. 6(a), are typical to 3D imaging signals as well. The other type of the signals, which are typical for the 3D imaging but are missed in the 2D scan in Fig. 6(a) are presented in (c)–(e). (c)–(d) BOs are detectable only in the left part of the LN sample and only before the CAP reflection, while the echo in the right part of the sample is not accompanied by the BOs. (e) Only the BOs in the left part of the sample and only when the CAP propagates from left to right are detectable. An uncommon type of the signals for 3D imaging, observed just in few experimental positions are presented in (f) and (g). (f) BOs are observed along the complete path of the CAP propagation from the Ti transducer to the right face of the LN sample and back. They disappear when the CAP returns to the Ti transducer (arrival time is marked by a green filled arrow). (g) BOs contain the features marked by red empty and red filled arrows, which are due to the CAP which initially is launched by the Ti transducer in water-ice VII but later (after the reflection at water-ice/diamond interface) is transmitted through the Ti transducer into the LN sample and arrives at the uncoated face of the LN sample, respectively (see Section 3.2.3). Even more atypical signals, which have been registered along the splits/cracks of the LN sample, are presented and discussed in Appendix D.
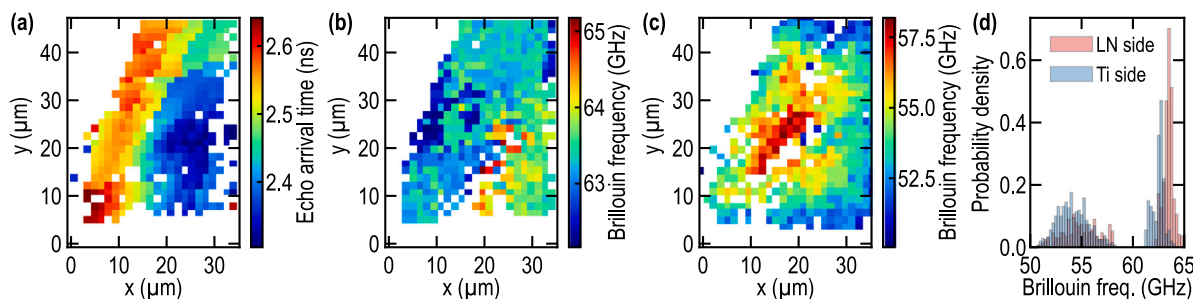

Fig. 8. (a) 2D map of the CAP arrival time at the LN/diamond interface and (b) spectral 2D map of the Brillouin frequency corresponding to LN, both obtained from the 3D TDBS measurements from the LN side of the sample, where the Brillouin oscillations in LN are dominating in amplitude. (c) Spectral 2D map of the Brillouin frequency corresponding to water-ice, obtained from the 3D TDBS measurements from the Ti side of the sample, where the Brillouin oscillations in water-ice are dominating in amplitude (see Section 3.2.2). (d) Histograms of the Brillouin frequency distributions in water-ice and LN obtained from the measurements from both LN (transparent red) and Ti (transparent blue) sides. In Appendix D, we additionally discuss the correlation between the images of the fractured crystal obtained by TDBS and by optical microscope (Fig. 3(c)).

it. The deviation of the acoustically-scattered probe light from the heterodyning direction can lead to an abrupt diminishing and even a complete disappearance of the BOs. For the case of the non-diffracting Gaussian probe light beam interacting with the non-diffracting Gaussian CAP beam, the theory was suggested in [40] and predicted a strong Gaussian diminishing of the BOs amplitude with increasing angle between scattered and heterodyning probe light directions. We will adapt the equations of this theory to describe rather quantitatively some of our experimental configurations in the DAC in Section 4. Just now, we will present graphical illustrations of the deviations in the propagation paths of the probe light and CAPs that are expected in our sample with inclined interfaces by updating the simple scheme previously shown in Fig. 2. The update of that scheme is depicted in Fig. 9(a) in order to qualitatively explain the absence of the detectable BOs when CAP propagates in some parts of the sample (right, left or both), as revealed in Figs. 6 and 7.

Note that the scheme in Fig. 9(a), illustrating the case with no layer of water-ice VII between the LN crystal and diamond anvil, is expected to be the closest to our experiment in most of the lateral positions, because no obvious signatures of the water-ice presence, either in the time domain or in the frequency domain, were recognized in the TDBS imaging signals (except some isolated points near the lateral edges of the LN sample). Our TDBS observations indicate that the water did not penetrate much between the LN and diamond surfaces (see Section 4 for detailed discussion) during the sample preparation, *i.e.*, during the steps when the LN crystal was put on the surface of one of the diamond anvils, the cell was filled with water and, after closing the cell with the second diamond, the pressure was increased. In Fig. 9, α denotes the local inclination angle between the opposite faces of the LN sample which, under the assumption of a homogeneous and very thin water-ice layer between LN and diamond on the right side, is also the inclination angle between the Ti transducer and the diamond anvil, confining the layer of water-ice VII with a varying thickness on the left side. We remind here that the schemes in Fig. 9 are a local view of the sample, *i.e.*, at the scale of laser focus. Laterally, along the sample, the inclination of the Ti transducer and the thickness of the water-ice layer vary in the left part, while the inclination is zero in the right part but the thickness of the confined thin water-ice layer can vary.

In the case of the experiments conducted from the right side (LN side) of the sample, of our interest here, the pump and probe laser beams are assumed, for simplicity, to be incident normally to the LN/diamond interface. Pump laser beam (not shown in Fig. 9), follows the path of the probe beam. When absorbed by the Ti transducer, pump laser pulse launches CAPs both in LN and in water-ice in the direction normal to the transducer surface, *i.e.*, at an angle α with respect to the direction of the probe light incident on the Ti transducer. Before the reflection of the launched CAPs at the interfaces inclined to their propagation directions, the CAPs-scattered probe light propagates at an angle 2α with respect to the direction of the incident probe light and parallel to the direction of the probe light reflected by the Ti transducer. The later (depicted by {1} in Fig. 9(a)) is therefore efficient in heterodyning the light scattered in the left half of our sample. However, the BOs are detectable only if the light propagating in this direction is transmitted across the inclined sample interfaces and directed by the experimental optics to the detector. This could be not the case for large α. When the CAP, propagating in LN, penetrates in the right part of the sample, the contribution of the above-described optical paths to the signal becomes negligible because of the coherence length effect (Section 3.1). In the right part of the sample, the heterodyning is accomplished by the probe light reflected at the LN/diamond interface (depicted by {2} in Fig. 9(a)) in 180° backward direction. Note that in the absence of the water-ice thin layer between LN and diamond on the right side, the amplitude reflection coefficient of the probe electric field is estimated to be of about 1.7–3.7% only, while the presence of a 20 nm-thick water-ice layer is sufficient for increasing the reflection coefficient up to 14.0–14.4% hence making the second channel of

heterodyning comparable in efficiency to the first one. This explains the comparable amplitudes of the TDBS signals, when the CAP is near the Ti transducer or is close to LN/water-ice/diamond interfaces structure, in many experimental points. Fig. 9(a) demonstrates that light, scattered by the CAP before and after reflection at this interface, propagates in both cases at an angle 2α to this direction inside LN and even at larger angle

$$\alpha' = \sin^{-1}\left[\frac{n_{\text{diamond}}}{n_{\text{air}}}\sin(2\alpha)\right],$$

when transmitted into air from diamond (if the angle deviation upon transmission from LN into diamond is neglected for simplicity). Therefore, the absence of the detectable BOs, when the CAP propagates in the right half of the sample (upper signals in Fig. 6, Fig. 7(b)–(d)), can be explained by the angle of the acoustically-induced probe light scattering that is too large relative to the heterodyning direction in the lateral positions of the sample with a sufficiently large inclination angle α (see [40] and Section 4). When the reflected CAP returns in the left part of the sample, its heterodyning also becomes less efficient than when it was propagating there before the reflection. In fact, the reflected CAP, propagating in the left part of the sample towards the Ti transducer, scatters the probe light at an angle 2α relative to the direction of the incident probe light and at an angle 4α with respect to the direction of the heterodyning probe light reflected from the Ti transducer. Therefore, the heterodyning efficiency is expected to be strongly reduced in the sample location with a sufficiently large inclination angle α, explaining why the BOs are nearly never detectable in the respective time interval, with the exception of a few points throughout the sample (Fig. 7(f)).

The simplest estimates of the critical angle γ for the disappearance of the TDBS signal, caused by the lost spatial overlap between the heterodyning (reflected) and acoustically-scattered light beams on the photodetector, can be accomplished by the evaluation of their far-field half-angle of divergence [58], $\theta_{FF}^{\text{reflected}} \equiv \frac{\lambda}{\pi a_{\text{ref}}}$ and $\theta_{FF}^{\text{scattered}} \equiv \frac{\lambda}{\pi a_{\text{sc}}}$, where λ is the light wavelength in the medium. In our experiments, where $a_{\text{probe}} = a_{\text{pump}} \equiv a$, the radius of the reflected light beam, a_{ref}, is equal to a, while the radius of the acoustically-scattered probe beam is smaller, $a_{\text{sc}} = a/\sqrt{3}$, because the scattered light field is due to the interaction of the probe light beam with radius a and the acoustic strain beam with radius $a_{\text{CAP}} = a/\sqrt{2}$, both at $1/e$ level. Here we have taken into account that the radial distribution of strain in the CAP is induced by the intensity distribution of the pump light and we have neglected the corrections to the CAP radius caused by the inclination of the optoacoustic transducer (Ti layer). These corrections are of the order $1 - \cos\alpha = 2\sin^2(\alpha/2) \ll 1$ in our experiments. Neglecting the lateral shift of the scattered light relative to the reflected one (Fig. 9), *i.e.*, assuming formally $H = 0$ in Fig. 9 in order to select the angle-dependent but thickness-independent effects, the heterodyning by the probe light reflected from the LN/diamond interface is expected to abruptly diminish when $\gamma \geq \theta_{FF}^{\text{reflected}} + \theta_{FF}^{\text{scattered}} = \frac{\sqrt{3}+1}{\pi}\frac{\lambda_{\text{probe}}}{a n_{\text{LN}}}$. In the right part of the LN sample, $\gamma = 2\alpha$, leading to the estimate of the critical inclination angle, $\alpha_{cr} = \frac{\sqrt{3}+1}{2\pi}\frac{\lambda_{\text{probe}}}{a n_{\text{LN}}} \approx 0.078$, corresponding to an angle of about 4.5°.

The duration of the detected wave packets of the BOs in Figs. 6(a) and 7 can be qualitatively interpreted by examining how the volume of the spatial overlap of the CAP and probe light beams, where they could interact, changes with the inclination angle and radii of the beams (Fig. 9(b)). In comparison with Fig. 9(a), the radius of the probe light beam a_{probe} is increased and that of the CAP beam is decreased to $a_{\text{probe}}/\cos\alpha$ to make them nearly equal in Fig. 9(b), as in our experiments due to equal radii of the probe and pump laser beams: $a_{\text{probe}} = a_{\text{pump}} \equiv a$. The Gaussian beams are replaced schematically by the cylinders. The acousto-optic interaction, *i.e.*, the probe light scattering by the CAP, could take place only in the regions of the intersection of the green and red nearly-transparent cylinders. In Fig. 9(b), we present the situation, where the CAP can scatter the
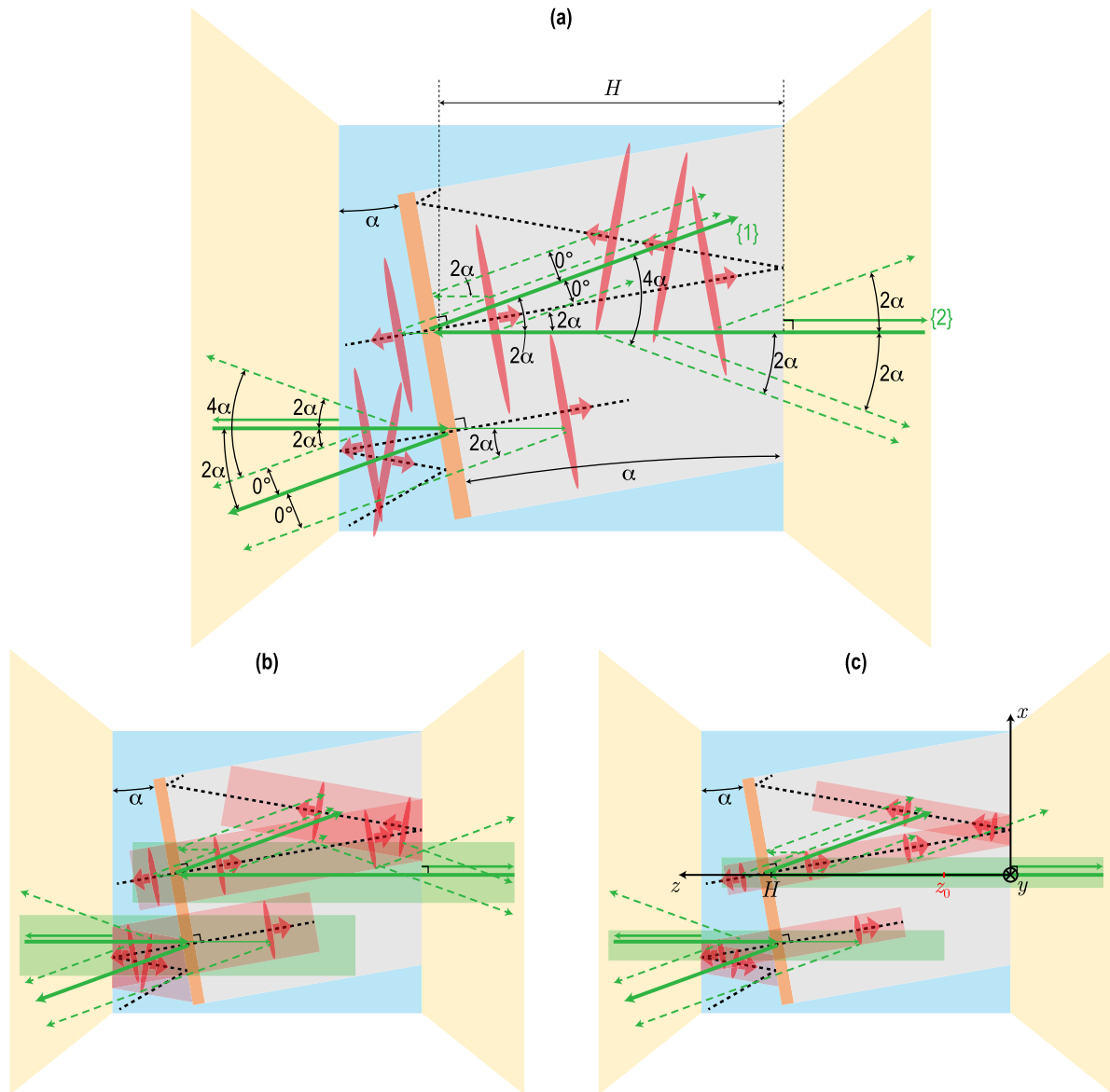
Fig. 9. (a)–(c) Schematics of the CAP and probe light paths in our TDBS experiments from LN side (upper part of the figures) and Ti side (lower part of the figures), where α stands for the local inclination angle of the Ti transducer relative to the diamond anvil surfaces. The two channels of heterodyning are illustrated for the CAP (transparent red ellipses) at different locations along its propagation path in both cases shown by the black dashed lines, the CAP propagation directions being given by the transparent red arrows. Green solid arrows indicate the incident probe beams and reflections of the probe light by stationary interfaces of the sample. Green dashed arrows indicate weakly scattered probe light by CAPs. We present optical paths of only the strongest reflected probe rays, which can interfere with the acoustically-scattered light and made detectable contributions to the TDBS signals in our experiments at $P = 10.4$ GPa. We also present only those scatterings of the probe light by CAPs which contributions to the TDBS signals were revealed in our experiments. For the experiments from LN side, the two channels of heterodyning are denoted {1} and {2}. In (b) and (c), the Gaussian CAP and probe beams are depictured by transparent red and green cylinders, respectively, with a larger radius in (b) compared to (c), which allows to illustrate the effect of the missing overlap (see z_0 in (c)) between both beams leading to fewer scattered probe light rays in (c).

probe light when traveling from left to right faces of the LN sample, but also during and after the reflection on the right side, and even when it starts to penetrate in the left part after the reflection at the LN/diamond interface. Only the return of the CAP to the Ti transducer is not detectable. When the radii of the beams are diminished about twice by retaining their inclinations (Fig. 9(c)), the only opportunity for the interaction is then in the left part of the sample after launching the CAP by the Ti transducer and just after the CAP penetration in the right part of the sample, while the arrival of the CAP on the right surface of the sample and its later propagation are not detectable. The same would happen if, instead of diminishing the beams radii, we would increase the inclination angles. The sketches of the type depicted in Figs. 9(b) and (c) are useful to estimate the conditions of the detectability of the CAP along its propagation path. For example, from Fig. 9(c), it follows that the overlap between the CAP and probe beams disappears at coordinate $z = z_0$, when $(H - z_0)\tan\alpha \geq 2a$. Particularly, when the CAP arrives at the LN/diamond interface, the drastic diminishing of the signal amplitudes, relative to their magnitudes expected in the absence of an inclination, is predicted for $\tan\alpha \geq 2a/H$. For our experimental conditions, this estimate transforms into $\alpha \geq 7.6°$. In view of our earlier estimates of the possible inclination angles in our sample, of similar magnitude, the latter estimate confirms that, in our experiments, significant variations could be caused by variations in the local inclination of the Ti transducer in the TDBS signals from one experimental point to another, including significant variations in their durations. In the opposite case, the decrease of the inclination angle provides an opportunity to detect the BOs even when the CAP returns to the Ti transducer (Fig. 7(f)), a rather uncommon observation. Of course, the detectability of the CAP returning to the Ti transducer also depends on the thickness of the material layer, separating the transducer and the interface reflecting the CAP, as it follows from the comparison of the sketches in the upper parts (in LN) and in the lower parts (in water-ice VII) in Fig. 9 (see also Section 3.2.2 and Section 4).

Thus, the schematic presentation in Figs. 9(b) and (c) provides insight that the different durations of the BOs packets in different lateral points of the sample (Figs. 6 and 7) can be related to the lateral inhomogeneity of the inclination angles between the opposite faces of the sample. However, for more quantitative evaluation of the variation of BOs packets with the inclination angles and beam radii, an analytical approach developed for Gaussian beams in [40] and Section 4 is preferable. In Section 4 we would adapt the theory from [40] to simulate the temporal shape of some of the detected TDBS signals, particularly to interpret our experimental detection at the right surface of the LN sample, either only of BOs (Figs. 5(a) and (d)) or only of the CAP (upper signals in Fig. 6, Fig. 7(b)–(d)), or of both BOs and CAP together (most of the signals in Fig. 6, Figs. 7(a), (f) and (g)). This variety of different signals can be also due to lateral variations of the inclination angle.

c. Different contributions explaining the lateral inhomogeneity of the Brillouin frequency: The variations of the BF in LN mapped in Fig. 8(b) obtained due to 3D imaging, are also indications of the sample 2D lateral inhomogeneity, confirming the earlier conclusions based on the comparison of Figs. 5(b) and 6(b). However, BF variations are only of about 6% over the complete scan, *i.e.*, more than 3 times smaller in comparison with the variations in the echo arrival times in Fig. 8(a). There can be multiple physically different contributions to observed lateral inhomogeneity of the BF. The most obvious are the contributions caused by lateral inhomogeneity of the optical refractive index, n_{LN}, and of the acoustical velocity, v_{LN}, and the lateral variations in the relative propagation directions of the probe light and the CAP. We remind here that in the 180° backward Brillouin scattering, for example, when the plane probe light wave is propagating parallel the plane acoustic wave, the BF is proportional to the product of refractive index and sound velocity. In the general case of the backward Brillouin scattering, the BF shift in scattering of the plane light wave by a plane

acoustic wave additionally diminishes proportionally to cosine of the angle, when the angle between the probe light and acoustic waves propagation directions, β, increases from zero [26,27]. We now turn to the three above-mentioned contributions to BF inhomogeneity one by one.

Even if, in the initial point of the scan, we choose the probe polarization to approach the regime of degeneracy between the ordinary and extraordinary optical modes of the probe in LN, the non-hydrostatic deformation of the LN crystal potentially causes the relative deformation of the index ellipsoid in the other lateral points of the 3D image, resulting in the birefringent TDBS [55] and shifting of the dominant BF. Similar effect could be caused by the rupture of the sample, when it is accompanied by the lateral variations of sample surfaces orientation relative to the incident probe beam, because the light transmission through inclined interface of optically anisotropic media would, in general, modify both the directions of the light propagation and the polarization of light. Actually, in our 3D imaging experiments, it was impossible to suppress birefringence in all lateral points. Instead, beatings related to birefringence were detectable and continuously varying laterally. Comparing from this point of view the signals in Figs. 7(a), (c), (d), and (f) provides another signature of the lateral inhomogeneity of the damaged LN crystal. However, although the optical birefringence of LN is among the strong ones, *i.e.*, $2\frac{n_e - n_o}{n_e + n_o} \simeq 3.5\%$ [41] at our probe wavelength, it cannot be responsible in full for the observed 6% variation in BF (Fig. 7(b)), even if the rotation on the crystallites in the damaged sample relative to the incident probe polarization is done by all possible angles.

The situation with the contribution to the BF variations from the acoustical anisotropy of LN is different, because the longitudinal acoustic velocity in LN can vary by about 10% with the wave propagation direction [50], for example when the propagation direction changes by 90° from the x-direction to the z-direction. However, such strong variations in sound propagation direction are not expected in our experiments. Assuming that the CAP is initially launched by the Ti transducer close to the x-direction, even if the opposite face of the LN sample is inclined relative to the Ti film by the maximum angle of 16° earlier estimated (in point *a*), the inclination of the CAP reflected at the interface of LN with diamond from the x-direction would not exceed 32°, and the expected influence on the BF values will be, consequently, significantly smaller than 10%.

Fig. 9 illustrates that, during CAP propagation in the LN sample with inclined faces from left to right or from right to left (before its return to the Ti transducer), the direction of the CAP beam changes relative to the probe light beam direction, but not the magnitude of the angle between these directions, *i.e.*, only the sign. The modulus of the "interaction" angle is equal to α both before and after the CAP reflection from LN/diamond interface. Note, that it would increase to 3α only after the CAP reflection from the Ti transducer, but we are not detecting BOs after this reflection. To describe the 6% diminishing of the BF, the angle β between the propagation directions of plane acoustic wave and the plane probe light wave should increase from 0° to 20°. Thus, even with the maximal local inclination angle between the LN sample surfaces of $\alpha \approx 16°$, the considered effect alone cannot be responsible for the variations of the BFs revealed in Fig. 8(a). So, presumably, all three discussed effects should be combined to explain the map of the BFs revealed in the fractured LN sample in Fig. 8(b).

d. Periodic modulations of the Brillouin oscillations amplitude unrelated to birefringence but due to CAPs propagation in two different media simultaneously: In most of the experimental points of a 2D TDBS measurement (and later in the 3D TDBS measurement), a periodic modulation of the BOs amplitude is visible for the observation times smaller than about 0.5 ns. Such modulations are of significantly shorter period than those caused by birefringence and can be attributed to the beating between the BOs detected simultaneously in LN and in water-ice VII (see Fig. 2(a) and Fig. 9), when the CAPs are launched by the Ti

optoacoustic transducer in two opposite directions. In Fig. 6(a) and Fig. 6(c)–(f), the period of the modulation is of about 100–125 ps, corresponding to the beating frequency of f_{beat} = 10-8 GHz, which is the difference frequency between the BFs in LN and water-ice VII. This simple estimate, combined with the spectral 2D-map, presented in Fig. 8(b) (which is obtained from the 3D-imaging from the LN side where the BOs in LN are dominating in amplitude), suggests that the spectrum of the BFs in water-ice is expected in the spectral band approximately from 52 to 57 GHz. This simple estimate is in complete correlation with the spectral 2D-map presented in Fig. 8(c) (which is obtained from the 3D-imaging from the Ti side where the BOs in water-ice are dominating in amplitude, Section 3.2.2), as well as with the shift between the histograms of the BFs in water-ice and LN in Fig. 8(d). The revealed frequency band of the BOs in water-ice, includes the BF of 52.5 GHz reported in Fig. 2 of [59] for the polycrystalline water-ice VII at the pressure of interest in frequency-domain Brillouin scattering experiments (FDBS). This confirms the expectations that water-ice, squeezed between the diamond anvil and the Ti transducer, is indeed water-ice VII. Additional information on the parameters of this polycrystalline ice, which is revealed by our experiments, is presented in Appendix E.

In the next section we present the results of the 3D TDBS experiments from the opposite side of the sample, which are highly complementary to those reported above.

3.2.2. TDBS signals in the experiments conducted from the Ti-coated side of the LN plate

The signals detected from the Ti side (Fig. 10), *i.e.*, when pump and probe beams are incident from the sample side covered by the Ti transducer (Fig. 2(b)), are different from the signals detected from the opposite side of the sample (Fig. 7). This observation stands, although the schemes presented to the left and right of the Ti transducer in Fig. 9 are equivalent from a geometrical point of view if one assumes that the LN is replaced by water-ice and vice versa. The basic difference is due to a much smaller (an order of magnitude) thickness of the water-ice VII layer between the diamond anvil and the Ti generator, than the thickness of the LN sample. Because of this, the propagation of a CAP and its reflections inside the ice layer, as well as the propagation

of the CAP in the left part of the LN sample, can be followed by heterodyning the acoustically-scattered light by the light reflected only at the left part of the sample volume, *i.e.*, from the diamond/water-ice and water-ice/Ti interfaces (Fig. 2(b)). However, it is expected that the signals detected from the Ti side should also have the features that could be attributed to the manifestation of relative inclination of the surfaces/interfaces.

The typical TDBS signals detected in the considered configuration of the 3D TDBS imaging are presented in Fig. 10. The origin of the beating patterns in the BOs up to 0.25–1 ns of the observation time in Fig. 10 (left part) is the same as in Section 3.2.1, *i.e.*, the mixing of the BOs coming from the CAPs detected at the same time in the water-ice layer and in the LN sample, although the amplitude of the BOs in water-ice dominates now in the beginning of the signals, as opposed to the previous case (Section 3.2.1) where the BOs in LN did. This statement is confirmed by the temporal evolution of the signal spectrum presented in the right part of Fig. 10, where the lower and the higher frequencies depicted by white dashed horizontal lines correspond to the ones in water-ice VII and LN, respectively. The most typical observation in the TDBS experiments from the Ti side (Fig. 10) is an abrupt diminishing or a complete disappearance of the BOs in water-ice after a critical time of 0.25–0.5 ns. It is also the most important for the current investigation, because it can be associated with the arrival of the CAPs at the boundaries of the confined water-ice layer and, thus, can provide information on the profile and local inclinations of the Ti transducer after the LN sample rupture. Note that, before the critical time in the time–frequency representation (*i.e.*, in the left part of the right-column figures of Fig. 10(a)–(c)), there are each time a lower frequency content (at one frequency in (a) and (c) and at two frequencies in (b)) that we attribute to the presence of shear acoustic waves propagating in the water-ice VII layer of polycrystalline nature, as already observed previously at lower pressure, around 2 GPa, in other experiments [21].

The estimates of the maximal reflection coefficients of a CAP at the water-ice/diamond, $r^{ac}_{ice/C}$, and water-ice/Ti, $r^{ac}_{ice/Ti}$, interfaces were accomplished using the available parameters, gathered in Table 1, of diamond [60] and Ti [61], the density of water-ice VII at 10.4 GPa from the extrapolation reported in [59] and the lowest (longitudinal) acoustic velocity detected in the water-ice VII of our sample, revealed to
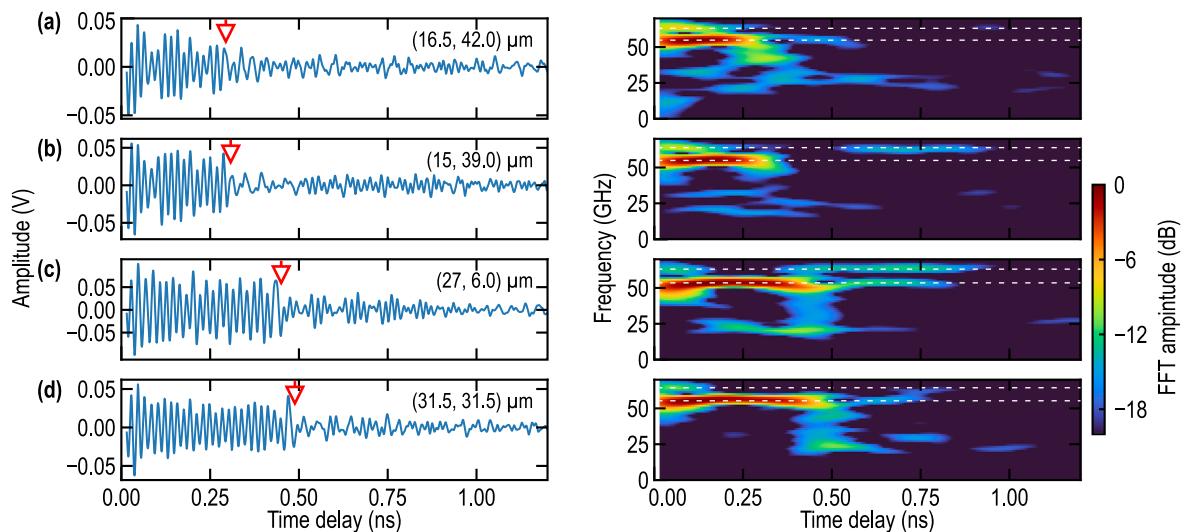

Fig. 10. Examples, measured at different locations (a)–(d), of the shapes/forms of the TDBS signals (left part) and their frequency spectra revealed using a short-time Fourier transform with 0.3 ns Hann window (right part) in the experiments conducted from the Ti side at *P* = 10.4 GPa. The red empty triangles indicate the moments of the CAP reflection at the water-ice/diamond interface, where the BOs amplitude strongly diminishes. The strong difference in the duration of the BOs in the water-ice VII in (a) and (b) in comparison with that in (c) and (d) indicates the lateral inhomogeneity of the water-ice layer thickness and inclination between the Ti transducer and the diamond anvil surfaces, caused by the rupture on the LN sample. The lower and the higher frequencies depicted by white dashed horizontal lines correspond to the Brillouin frequencies in water-ice VII and LN, respectively.

Table 1
Parameters of the materials composing the sample (diamond, Ti, water-ice VII, LN) at $P = 10.4$ GPa used in the estimates.

	ρ (g/cm^3)	v (μm/ns)	n
diamond	3.603 ± 0.094[a]	17.80 ± 0.57[a]	2.421 ± 0.005[b]
Ti	5.01[c]	7.0 ± 0.7[c]	$(2.38 + 3.30j) \pm (0.12 + 0.08j)$[d]
water-ice VII	1.88 ± 0.04[e]	$[8.29 \pm 0.06 - 9.60 \pm 0.07]$[f]	1.63 ± 0.01[g]
LN	4.967[h]	7.365[i]	2.248 (e), 2.342 (o)[j]

[a] From Table 2 (ρ) and Table 3 ($v = \sqrt{c_{11}/\rho}$ in [60], our diamond anvil being (100)-oriented.

[b] Estimated from Fig. 4 in [62], at $\lambda_{\text{probe}} = 0.535$ μm.

[c] From [61] assuming ω-Ti structure: the density is calculated using the third-order Birch–Murnaghan isothermal equation of state and parameters tabulated in Table 2; the longitudinal acoustic velocity is from Table 6 at 10 GPa and its associated uncertainty of $\pm 10\%$ is proposed by us to account for the difference between bulk mechanical properties of Ti and those of thin coated layer of Ti.

[d] Estimated from Fig. 6 in [63], at $\lambda_{\text{probe}} = 0.535$ μm and disregarding the data from Lynch et al..

[e] Estimated from Fig. 3 in [59].

[f] Estimated from our experimental results obtained from the Ti side (see Appendix E).

[g] Extrapolated from [59,64] and in agreement with [53].

[h] Estimated from [65].

[i] Estimated from our experimental results from the LN side, using the mean value between the ordinary and extraordinary refractive indices estimated at $P = 10.4$ GPa.

[j] From our measurement at $P = 1$ atm., the measured BFs (Fig. 4) have been used to estimate ordinary and extraordinary refractive indices, n_o and n_e, respectively, at atmospheric pressure in our LN sample. We then use the theoretical expected increase of indices estimated from [43] in order to obtain n_o and n_e at $P = 10.4$ GPa. Note that the mean value is used in our estimates/fits because it is not possible to know which combination of the optical modes we actually detect at $P = 10.4$ GPa: $n = 2.295$.

be $v_{\text{water-ice}} \approx 8.3$ μm/ns in Appendix E. These estimates lead to $r^{\text{ac}}_{\text{ice/C}} \approx 0.61$ and $r^{\text{ac}}_{\text{ice/Ti}} \approx 0.38$. Thus, at least two reflection moments could be expected to be visible in the time-domain signals before any significant reduction of the signal amplitude, even in the presence of the beatings, if the inclination of the Ti transducer relative to the diamond anvil is not accounted for. Yet, the inclination of the Ti transducer leads to the inclination of the strongest heterodyning light beam, i.e., the one reflected from the Ti transducer, relative to the diamond surface (Fig. 9). It also leads to an oblique incidence of the CAP on this surface. As a consequence, the direction of the acoustically-scattered light with respect to the direction of this strongest heterodyning beam deviates significantly from the case of collinearity after the reflection. After the CAP reflection, the acoustically-scattered light direction is inclined with respect to the direction of the strongest heterodyning light at an angle which is four times larger than the inclination of the Ti transducer (Fig. 9). For the range of the inclination angles we estimated earlier, this could lead to a significant additional reduction in the amplitude of the BOs after the first CAP reflection, if not their complete disappearance (Section 4). This analysis provides the explanations about the fact that the first abrupt diminishing of the BOs amplitude, indicated in each part of Fig. 10 by a red empty triangle, is significantly larger than the one expected from the CAP reflection considerations, while a very strong reduction of the BOs amplitude in water-ice after the CAP reflection at the water-ice/diamond interface is the most common feature of the 3D TDBS experiments. Fig. 10(c) provides a rare example where the BOs associated with the CAP in the water-ice layer as well as their beating with the BOs associated with the CAP in the LN sample are detectable up to the time of the return of the water-ice CAP at the Ti transducer (at about 1 ns time delay). The TDBS signals with measurable ratio of the BOs amplitudes in the water-ice layer before and after the first reflection of the CAP are usable for the estimation of the Ti transducer inclination angle (see Section 4).

It is interesting to estimate the critical inclination angles for which the TDBS signal disappearance could be expected, when the CAP is reflected at the water-ice/diamond interface, for comparison with the previous equivalent analysis in Section 3.2.1. When the CAP propagates from the Ti transducer towards the water-ice/diamond interface, Fig. 9, the heterodyning by the probe light reflected from the Ti transducer should largely dominate over the heterodyning by the light reflected

from the diamond/water-ice interface. We call them here as the first and the second channel of heterodyning, respectively. The first channel dominates, not only because the reflectivities of the probe light at the mentioned interfaces are importantly different ($r_{\text{ice/Ti}} \approx 0.6 > r_{\text{diamond/ice}} \approx 0.2$), but also because of the difference in the scattered light direction relative to the two heterodyning directions. In the first channel, the angle γ between the directions of scattering and heterodyning is equal to zero, while along the second channel $\gamma = 2\alpha$, as in the earlier analysis in Section 3.2.1. After the CAP reflection, the angle in the first channel increases to $\gamma = 4\alpha$, while the angle in the second channel keeps the same value $\gamma = 2\alpha$ (see Fig. 9). The estimates of the critical inclinations for the detection of the TDBS after the CAP reflection suggest $\alpha_{cr} \approx 3.3°$ and $\alpha_{cr} \approx 6.5°$, respectively. These estimates suggest that, for any nonzero inclination angle, we could expect the diminishing of the BOs amplitude after the CAP reflection, which is additional to the expected diminishing due to the acoustic reflection of ~ 0.6-0.7 (depending on water-ice VII orientation) at the water-ice/diamond interface. However, the additional dependence on the inclination angle can be rather complex (see Section 4), because the transition of the dominant heterodyning channel from the first one to the second one occurs at $\alpha \leq \alpha_{cr} \approx 3.3°$.

Note that the evidence of the inclination of the Ti transducer caused by the LN sample rupture is also provided, in the TDBS experiments from the Ti side, via profilometry, i.e., by revealing the variations in the water-ice layer thickness. In fact, the increase in the BOs duration in Fig. 10 by about 50%, appreciable between the signals in (a)–(b) and (c)–(d), cannot be (fully) attributed to the lateral inhomogeneity in the acoustic velocities (revealed by the map of the BFs in Fig. 8(c)), because the maximal variation in the water-ice velocities observed in our experiments is only about 15%.

In the following Section 3.2.3, we discuss how else the TDBS experiments conducted from the opposite sides of the LN sample can be complementary.

3.2.3. Fruitful complementarity of the TDBS experiments conducted from the opposite sides of the LN sample

Unfortunately, our current experimental setup does not provide the opportunity to conduct 3D TDBS imaging experiments by directing the pump/probe laser beams from both sides of the LN sample to the exact
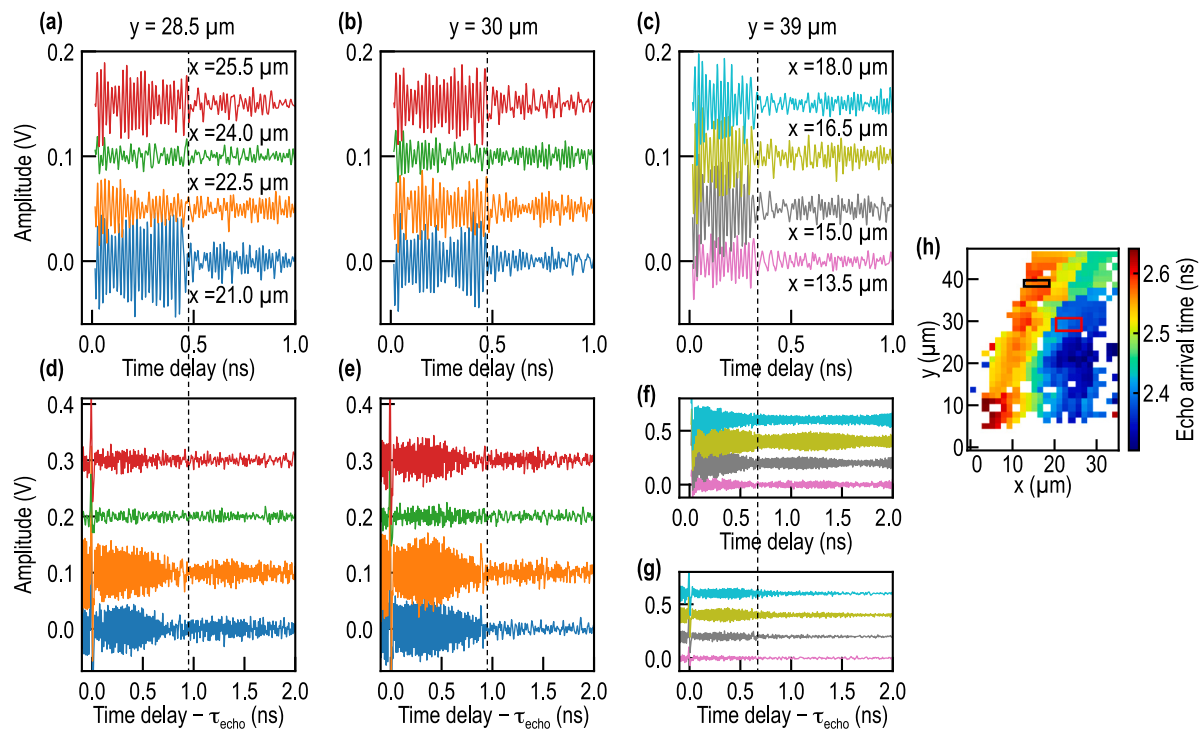
Fig. 11. (a)–(g) Fruitful complementarity of the TDBS signals detected from the opposite sides of the sample (in the upper (a)–(c) and lower (d)–(g) rows from Ti and LN sides, respectively). The experimental results from the areas marked on the echo arrivals time map (h) by red and black rectangles are presented in the first two and the third columns, respectively. The time in the lower row is scaled twice relative to the upper row and delayed by the first echo arrival time τ_{echo} to provide visual evidence for the presence of the features carrying the information on the second echo propagation in water-ice in the signals detected from the LN side (see main text). The vertical dotted lines stand for guiding the eyes over the corresponding features captured in signals from the opposite sides.

same positions on the Ti transducer. Therefore, certain estimates, which may necessitate measurements from both sides, such as the full local thickness of the sample (*i.e.*, water-ice plus Ti plus LN), might not be entirely convincing in the presence of lateral inhomogeneity. This is particularly true when the measurement points from opposite sides are separated by a distance up to, but less than, 1.5-2 μm. However, the combination of the measurements from both sides become much more convincing and useful, when it is possible to reveal, from the 3D TDBS measurements from opposite-side, 2D spatial clusters in (x,y)-planes of experimental points containing TDBS signals with similar characteristic features at practically the same temporal moments and partially overlapping. Then, inside these overlapping clusters, the complementary information in the signals detected from the opposite sides in neighbor points, although not completely coincident ones, can be considered as reliable.

In Fig. 11, for comparison and a joint analysis, we present the TDBS signals accumulated inside two of such overlapping clusters. The signals detected from the Ti and LN sides of the sample are presented in the upper and lower rows, respectively. Note that, for comparison convenience, the zero time in the lower row (except (f)) is shifted by subtracting the arrival time of the CAP on the right face of the LN sample and the time interval separating consecutive ticks on the abscissa axis is twice shorter than in the upper row. The signals in Figs. 11(a), (b), (d), and (e) are from the 2D area marked by a red rectangle in the map of the arrival times (Fig. 11(h), which duplicates Fig. 8(a) for convenience).

The comparison of the signals in Figs. 11(a) and (b) with those in Figs. 11(d) and (e) reveals, in the TDBS signals (d) and (e) measured from the LN side, the features corresponding to the arrival on the right face of the LN sample of the second CAP, which was initially launched

in the water-ice and that, after reflection at the water-ice/diamond interface, traveled back through the water-ice towards the Ti transducer, and continued its propagation through the LN sample after transmission through the Ti layer. The vertical dashed lines, used to guide the eyes, indicate the time of flight of the CAP propagating from the Ti transducer to the water-ice/diamond interface (the identification of such time of flight for the case of the upper row signals in Figs. 11(a) and (b) has been explained in Section 3.2.2). The echoes in the lower row signals are approximately at twice longer delay times, as it could be expected, because the first and the second echoes, in the general case of an inclined Ti transducer, are crossing the LN sample at different angles/directions. The signals in Figs. 11(c), (f) and (g) are from the 1D area marked by a black rectangle in the map of the arrival times (Fig. 11(h)). In this area, the signatures of the second echo are revealed not only when it arrives to the right face of the LN sample (Fig. 11(g)), but also when it reaches the Ti/LN interface after traveling in the water-ice layer (Fig. 11(f)). Note that the signals in Figs. 11(f) and (g) do not present the same part of the complete time scale as the zero time in (f) is the actual beginning of the signal while the zero time in (g), as explained before, is corresponding to the CAP arrival time at the right face of the LN sample.

We have used the signals from Fig. 11 to estimate the total thickness of the water-ice, Ti and LN layers between the diamond anvils. In fact, it is sufficient to use the signals detected from the LN side, because they contain the information on the propagation times of the CAP both in the LN and in water-ice. The local acoustic velocities were determined from the 2D maps of the disentangled BFs in the water-ice and LN (Appendix E). The estimates accomplished for the clusters presented in Fig. 11 confirmed that, despite the different thicknesses of the water-ice and LN layers, the total thicknesses of the materials confined between

the diamond anvils are very close, *i.e.*, 21.82 ± 0.5 μm and 21.79 ± 0.5 μm, for the red and black rectangles, respectively.

In view of the challenging inclined geometry of our sample and the poorly known optical properties in LN at high pressures, since only a theoretical prediction is available (see footnote j in Table 1, [43]), we believe that the correlation between the total materials thicknesses, estimated by us, and the distance between the diamond anvils, revealed by optical interferometry, is good.

4. Analytical theoretical description of TDBS signals in case of CAP propagating at an angle to probe light and heterodyning directions

For the theoretical description of the most interesting TDBS signals in our experimental geometries, schematically illustrated in Fig. 9, it is possible to adopt the following formula derived in [40] for TDBS in the case of non-diffracting probe light and CAP beams:

$$\frac{dR}{R} \propto \iint_{-\infty}^{+\infty} I_+^{probe}(x, y) \left[\int_0^{+\infty} \eta(t, x, y, z) \sin(2k_1 z) dz \right] dx dy. \quad (1)$$

The theory derived in [40], in the paraxial approximation of the diffraction theory, and adapted in the current study has a distinctive feature: it considers the lateral Gaussian distribution of both the probe light pulse and the CAP, which propagate at an angle to each other. The literature already offers some advanced analytical approaches, such as elasto-optical interaction in a two-layer structure with oblique probe light incidence [66] or for reflectometric detection of diffracted acoustic fields [67]. However, the former approach is based on the assumption of the probe light being a plane wave, while the latter one, rather general but semi-analytical, primarily focuses on collinear Gaussian pump and probe beams and lacks straightforward insights into the interaction of the non-diffracting probe light and acoustic beams. Moreover, the theory developed in [67] was applied to interpret experiments in which the strongly diffracted acoustic beams were detected near the surface of a medium opaque for the probe light, *i.e.*, of the experiments drastically different from ours. Ref. [40] is the only one, to our knowledge, that incorporates all the necessary assumptions in an analytical approach to describe the experimental results reported in the previous sections. The coordinate system in Eq. (1) corresponds to the one presented in the lower part of Fig. 1(a) and the right parts of Fig. 9. $I_+^{probe}(x, y)$ is the intensity distribution in the cross section of the probe beam, which is incident normally to the plane interface between two transparent media. Eq. (1) accounts for the acousto-optic interaction only in the positive half space (k_1 is the wavenumber of the probe light there), *i.e.*, it is valid only when the TDBS signal from negative half space is negligibly small in comparison with that of Eq. (1). The distribution of the acoustical strain field, $\eta(t, x, y, z)$, in Eq. (1) is arbitrary and, thus, Eq. (1) can be adopted for the description of the TDBS signals in the geometry presented in the right parts of Fig. 9, where both the direction of the CAP propagation relative to the probe laser beam and the position of incidence of the CAP beam on the interface, $z = 0$, is *a priori* arbitrary, *i.e.*, locally varying, depending on the inclination between the plate faces and on the plate thickness, for example. We remind here that the schemes in Fig. 9 present not the complete LN plate, but just a local piece of the LN plate with a particular inclination angle α between the plate surfaces. This means that the (x, z)-plane of the coordinate system, including the central rays of the probe light and CAP beams (the latter propagating normally to the inclined Ti optoacoustic transducer), constitutes a local coordinate system. This local coordinate system rotates around the z-axis of the laboratory coordinate system as the direction of CAP propagation changes from one experimental point to another. Note that, for the plane in which probe light and coherent CAP propagate collinearly, Eq. (1) reduces to a classical form (in the limiting case of real optical and acousto-optical constants) $\frac{dR}{R} \propto \int_0^{+\infty} \eta(t, z) \sin(2k_1 z) dz$ [24–26].

To get the analytical description of the TDBS signal from Eq. (1), we considered that both the probe intensity and CAP amplitude are Gaussian beams with radii a_{probe} and a_{CAP} at $1/e^2$ level, respectively, which

is a highly relevant assumption for our experiments. Additionally, we assumed Gaussian temporal profile of the CAP, which in space has the half-length l_{CAP}, also at $1/e^2$ level. Then, all integrations in Eq. (1) can be done with a single table integral (7.4.32 in [68]). We suggested that, at $t = 0$, the CAP beam axis intersects the probe beam axis at an angle α at coordinate $z = H$, with H representing the local thickness of the plate. As we were mostly interested in the description of the TDBS signal around the CAP arrival on the LN/diamond interface, we did not consider the CAP launched in water-ice VII, took into account that the CAP in LN propagates towards the LN/diamond at velocity v_1 and shifted, in the resulting formulas, the time axis by $\frac{H}{v_1 \cos \alpha}$, introducing the delayed time $\tau = t - \frac{H}{v_1 \cos \alpha}$. The analytical description of the TDBS signal due to the probe light scattering by the CAP in LN, which is incident on the LN/diamond interface, is:

$$\left. \frac{dR}{R} \right|_{inc} (\alpha, H, v_1) \propto \frac{a_{CAP}^2 l_{CAP} e^{-2 \left[\frac{v_1 \left(\tau + \frac{H}{v_1 \cos \alpha} \right)}{l_B(\alpha)} \right]^2} e^{-\frac{[k_1 d(\alpha)]^2}{2}}}{l_B(\alpha) |\sin \alpha| \sqrt{a_{probe}^2 + a_{CAP}^2}}$$

$$\Im \left\{ e^{2jk_1 H} e^{-j\Omega_B(\alpha) \left(\tau + \frac{H}{v_1 \cos \alpha} \right)} \right. \quad (2)$$

$$\times \left[1 - \mathrm{erf} \left[\frac{\sqrt{2}}{d(\alpha)} \left\{ \frac{\Omega_B(\alpha)}{\Omega_B(0)} v_1 \left(\tau + \frac{H}{v_1 \cos \alpha} \right) \right. \right. \right.$$

$$\left. \left. \left. \left. - H - j \frac{k_1 [d(\alpha)]^2}{2} \right\} \right] \right] \right\}.$$

In the derived formula, we introduced the following compact notations:

$$l_B(\alpha) \equiv \sqrt{\left(\frac{a_{probe}}{\sin \alpha} \right)^2 + \left(\frac{a_{CAP}}{\tan \alpha} \right)^2 + l_{CAP}^2}, \quad (3a)$$

$$d(\alpha) \equiv \frac{\sqrt{\left(\frac{a_{CAP} l_{CAP}}{\sin \alpha} \right)^2 + \left(\frac{a_{probe} l_{CAP}}{\tan \alpha} \right)^2 + a_{CAP}^2 a_{probe}^2}}{l_B(\alpha)}, \quad (3b)$$

$$\Omega_B(\alpha) \equiv 2k_1 v_1 \frac{a_{probe}^2 + a_{CAP}^2}{[l_B(\alpha) \sin \alpha]^2} \cos \alpha. \quad (3c)$$

All three parameters, $l_B(\alpha)$, $d(\alpha)$ and $\Omega_B(\alpha)$, were revealed for the first time in application of Eq. (1) to the analysis of the TDBS signals in the case of an interaction between the probe and the CAP beams (with the same parameters and mutual inclination angle, as described above) in free space, *i.e.*, in transparent media far from the interfaces [40]. The solution obtained in [40] predicted that the TDBS signal is a sinusoidal signal with a carrier frequency $\Omega_B(\alpha)$ and a Gaussian envelope of the length $l_B(\alpha)$. The characteristic length $d(\alpha)$ enters the Gaussian dependence, tightly controlling the amplitude of the wave packet. Note that these parameters depend on all the geometric parameters of the probe light and CAP beams in addition to the inclination angle α. We reveal here that they also show up in the derived solution in Eq. (2) and at the right places corresponding to their above described physical sense. The most important difference of the TDBS signal in Eq. (2) from that in free space comes from the additional modulation in time in the former, appearing from the square bracket containing the error function (denoted erf) with time dependent argument, which accounts for the transient effects related to the CAP arrival on the interface. It is straightforward to check that, in our case, the function $\mathrm{erfc} \equiv 1 - \mathrm{erf}$ in Eq. (2) describes the decay of the TDBS signal, when the incident CAP is crossing the interface at $z = 0$. Similar transient effects were revealed in [40] for the CAPs reflected and refracted by the interface, inclined relative to their propagation direction, but only in the asymptotic case of infinitely short (delta-localized) CAPs. As a consequence the theory in [40] described only transient modulation of the carrier wave at BF, but did not reveal any wide-frequency-band transients, which could correspond to the CAP profile detection

at the interfaces. The formula in Eq. (2) was derived for the CAPs of arbitrary length, with the expectations that it can describe both the detection of the BOs and the detection of CAPs at the interfaces, as it was observed in the experiments (Section 3.2.1). The simplest confirmation of these expectation can be obtained, by the analysis of Eq. (2) for zero inclination between the plate surfaces, $\alpha = 0$. In this case, $d(\alpha = 0) = l_{\text{CAP}}$ and the imaginary part of the erf function argument in Eq. (2) reduces to $-J\frac{k_1 l_{\text{CAP}}}{\sqrt{2}}$. Therefore, when $k_1 l_{\text{CAP}} \to 0$, the argument is purely real and the TDBS signal is a carrier wave at BF modulated in amplitude. When, $k_1 l_{\text{CAP}} \to +\infty$, the application of the asymptotic expansion of the erfc function (7.1.23 in [68]) predicts that the carrier disappears in Eq. (2) and it predicts a CAP profile. However, the latter conclusion is much easier to reveal by performing the integration over depth coordinate z by parts in Eq. (1):

$$\int_0^{+\infty} \eta(t, x, y, z)\sin(2k_1 z)\mathrm{d}z = \frac{1}{2k_1}\eta(t, x, y, 0)$$
$$- \frac{1}{(2k_1)^2}\int_0^{+\infty}\frac{\partial^2 \eta}{\partial z^2}(t, x, y, z)\sin(2k_1 z)\mathrm{d}z.$$

As $\partial/\partial z \sim 1/l_{\text{CAP}}$, the TDBS signal when $k_1 l_{\text{CAP}} \to +\infty$ is controlled by the temporal profile of the strain field at the interface, while the contribution of the BOs is negligibly small, i.e., $\int_0^{+\infty}\eta(t, x, y, z)\sin(2k_1 z)\mathrm{d}z \cong \frac{1}{2k_1}\eta(t, x, y, 0)$. This indeed corresponds to the limiting case of a CAP so long that it has negligibly small spectral amplitude at the Brillouin frequency. This asymptotic analysis supports the expectations that Eq. (2) describes the detection at the interface of the BOs and CAP simultaneously in the general case. In addition, it is expected that the formula in Eq. (2) accounts for the lateral shift at the probed interface $z = 0$ of the CAP center relative to the probe light center, as illustrated in Figs. 9(b) and (c).

For the description of the experimental TDBS signals, detected near the times of CAP arrival at the LN/diamond interface, the signal due to the reflected CAP should be added to the signal due to the incident CAP. The former can be evaluated as the signal from a CAP beam which is mirror symmetric to the incident CAP beam relative to the $z = 0$ interface. The description of the reflected signal can be obtained from the incident signal by the following transformation:

$$\alpha \to -\alpha, H \to -H, v_1 \to -v_1,$$

which leads to:

$$\left.\frac{\mathrm{d}R}{R}\right|_{\text{refl}}(\alpha, H, v_1) \propto \frac{a_{\text{CAP}}^2 l_{\text{CAP}} e^{-2\left[\frac{v_1\left(\tau + \frac{H}{v_1\cos\alpha}\right)}{l_B(\alpha)}\right]^2} e^{-\frac{[k_1 d(\alpha)]^2}{2}}}{l_B(\alpha)\,|\sin\alpha|\,\sqrt{a_{\text{probe}}^2 + a_{\text{CAP}}^2}}$$

$$\Im\left\{ r_{\text{LN/C}}^{\text{ac}}(\alpha)e^{-2jk_1 H}e^{+J\Omega_B(\alpha)\left(\tau + \frac{H}{v_1\cos\alpha}\right)} \right.$$

$$\times \left[1 + \text{erf}\left[\frac{\sqrt{2}}{d(\alpha)}\left\{ \frac{\Omega_B(\alpha)}{\Omega_B(0)}v_1\left(\tau + \frac{H}{v_1\cos\alpha}\right) \right.\right.\right.$$

$$\left.\left.\left.\left. - H + J\frac{k_1 [d(\alpha)]^2}{2} \right\}\right]\right]\right\} \tag{4}$$

where $r_{\text{LN/C}}^{\text{ac}}(\alpha)$ (first term in the imaginary function $\Im\{\}$) is the complex acoustic strain reflection coefficient at the LN/diamond interface. Particularly, the term:

$$\left[1 - \text{erf}\left[\frac{\sqrt{2}}{d(\alpha)}\left\{ \frac{\Omega_B(\alpha)}{\Omega_B(0)}v_1\left(\tau + \frac{H}{v_1\cos\alpha}\right) - H - J\frac{k_1 [d(\alpha)]^2}{2} \right\}\right]\right]$$

in Eq. (2), controlling the disappearance of the TDBS signal from the incident CAP, when it reaches the $z = 0$ interface, transforms into:

$$\left[1 + \text{erf}\left[\frac{\sqrt{2}}{d(\alpha)}\left\{ \frac{\Omega_B(\alpha)}{\Omega_B(0)}v_1\left(\tau + \frac{H}{v_1\cos\alpha}\right) - H + J\frac{k_1 [d(\alpha)]^2}{2} \right\}\right]\right]$$

in Eq. (4), describing the simultaneous emergence of the TDBS signal from the reflected CAP.

The TDBS signals, theoretically predicted above, could be rewritten more compactly for our particular experimental configuration, where the radii of the pump and probe laser beams are equal, $a_{\text{pump}} = a_{\text{probe}} \equiv a$, while the CAP is generated by the pump laser beam incident on the Ti generator, inclined relative to the pump incidence direction, and thus: $a_{\text{CAP}} = \frac{a_{\text{pump}}}{\cos\alpha} = \frac{a}{\cos\alpha}$. Under these conditions, the characteristic lengths and cyclic BF in Eq. (3) are described by:

$$l_B(\alpha) \equiv \sqrt{2\left(\frac{a}{\sin\alpha}\right)^2 + l_{\text{CAP}}^2},$$

$$d(\alpha) \equiv \frac{a}{l_B(\alpha)|\cos\alpha|}\sqrt{\left(1 + \cos^4\alpha\right)\left(\frac{l_{\text{CAP}}}{\sin\alpha}\right)^2 + a^2},$$

$$\Omega_B(\alpha) \equiv 2k_1 v_1 \frac{a^2\left(1 + \cos^2\alpha\right)}{\left[l_B(\alpha)\sin\alpha\right]^2\cos\alpha}.$$

The coefficient in front of the exponential functions in Eq. (2) takes the form:

$$\frac{al_{\text{CAP}}}{l_B(\alpha)|\sin\alpha\cos\alpha|\sqrt{1 + \cos^2\alpha}}.$$

For the easy visual comparison in the TDBS signals of the detection of the CAP and of the BOs, we find convenient to normalize the time variable by the period of BOs as follows: $\theta = \Omega_B(0)\tau = 2k_1 v_1 \tau$. Then, the TDBS signal in Eq. (2) depends on the angle α and three non-dimensional parameters: $k_1 l_{\text{CAP}}$, $k_1 H$, and $k_1 a$. In our experiments, $H > a \gg l_{\text{CAP}}$ and, therefore, $k_1 l_{\text{CAP}}$ can be omitted in several parts of Eq. (2), resulting in:

$$\left.\frac{\mathrm{d}R}{R}\right|_{\text{inc}} = \frac{k_1 l_{CAP}\,e^{-\frac{1}{4}\left(\frac{\sin\alpha\left(\theta + \frac{2k_1 H}{\cos\alpha}\right)}{k_1 a}\right)^2}e^{-\frac{[k_1 d(\alpha)]^2}{2}}}{|\cos\alpha|\sqrt{\left(1 + \cos^2\alpha\right)}}$$

$$\Im\left\{ \exp\left[-J\left(\frac{1 + \cos^2\alpha}{2\cos\alpha}\theta + k_1 H\tan^2\alpha \right) \right] \right.$$

$$\times \left[1 - \text{erf}\left[\frac{1}{\sqrt{2}k_1 d(\alpha)} \right.\right.$$

$$\left.\left.\left. \times \left\{ \frac{1 + \cos^2\alpha}{2\cos\alpha}\theta + k_1 H\tan^2\alpha - J\left[k_1 d(\alpha)\right]^2 \right\} \right]\right]\right\}, \tag{5}$$

where the relation $\frac{1+\cos^2\alpha}{2\cos\alpha}\left(\theta + \frac{k_1 H}{\cos\alpha}\right) - 2k_1 H = \frac{1+\cos^2\alpha}{2\cos\alpha}\theta + k_1 H\tan^2\alpha$ has been used and

$$k_1 d(\alpha) \equiv \sqrt{\frac{(k_1 a)^2\sin^2\alpha + (k_1 l_{\text{CAP}})^2\left(1 + \cos^4\alpha\right)}{2\cos^2\alpha}}.$$

Thus, in our experimental conditions, in addition to the proportionality of the TDBS signal to l_{CAP}, as in the case of the delta-localized CAPs [26,40], the finite length of the CAP contributes only to the non-dimensional parameter $k_1 d(\alpha)$. A similar expression to the one in Eq. (5) with non-dimensional parameters can be easily found for $\left.\frac{\mathrm{d}R}{R}\right|_{\text{refl}}$ from Eq. (4).

For a more quantitative comparison of the above theoretical predictions with our experimental observations, the above solutions should be differentiated over time to predict the TDBS signal due to a bipolar CAP with the shape described by the derivative of the Gaussian function. We have verified that numerical differentiation produces results consistent with analytical formulas obtained by analytical differentiation. Since the analytical formula is quite cumbersome, we will not present it here. For illustrating the theoretical predictions, we have estimated the contributing parameters at the pressure $P = 10.4$ GPa: $k_1 H \approx 504$ (using $H = 18.7$ μm, assumed earlier in Section 3.2), $k_1 a \approx 33.7$, $k_1 l_{\text{CAP}} \approx 2.18$, and $r_{\text{LN/C}}^{\text{ac}}(\alpha) \approx r_{\text{LN/C}}^{\text{ac}}(0) \approx 0.27$ when assuming this coefficient to be
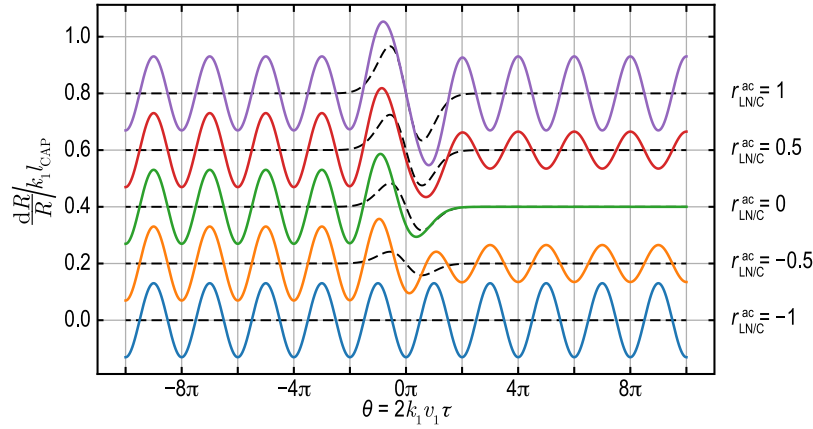
Fig. 12. Theoretical TDBS signals, $\frac{dR}{R}/k_1 l_{CAP}$ as a function of $\theta = 2k_1 v_1 \tau$, for different strain reflection coefficients, $r_{LN/C}^{ac}$, from −1 to 1. The black dashed lines stand for the asymptotic case $k_1 l_{CAP} \to +\infty$, *i.e.*, for the case of the CAP profile only, corresponding to the limiting case of a CAP so long that it has negligibly small spectral amplitude at Brillouin frequency.

real valued (the "C" in the index standing for diamond). The CAP half-length, l_{CAP}, was estimated from the measurement of the time, ≈ 11 ps, between the maximum and the minimum of the bipolar CAP profiles, which were revealed by zooming in the signals of the type shown in Fig. 7(f) near the CAP arrival at the LN/diamond interface. This type of signals is expected to correspond to measurements location with the smallest inclination angles and, thus, to demonstrate the shortest CAP duration ($l_{CAP} \approx 81$ nm in LN) not biased by the inclination angle. Note that, as it will be seen in the following, a precise estimate of the CAP length is not easy to be obtained just from an analysis "by eyes" of the temporal signal, since the value of the local reflection coefficient can play an important role in how the CAP and the BOs contributions superimpose to form the TDBS signal.

First, it is proposed to look on how the model is predicting different possible features in a TDBS signal depending on the choice of the parameters. Second, few qualitative comparisons between experimental signals and signals predicted from the analytical expression are presented and the need of using a complex reflection coefficient at the LN/diamond interface accounting for the presence of a thin layer of water-ice VII between both materials is motivated and discussed.

Using the previously given values of the non-dimensional parameters and $\alpha = 0°$, Fig. 12 presents the TDBS signals obtained by varying the strain reflection coefficient $r_{LN/C}^{ac}$ from −1 to 1, assuming it is real

valued. Note that the signals are plotted with respect to the normalized time θ. This figure, where solid lines depict $\frac{dR}{R}/(k_1 l_{CAP})$ (sum of contributions from the incident and reflected CAP) and dashed lines stand for the asymptotic case $k_1 l_{CAP} \to +\infty$, clearly explains why the CAP profile was not detected in our experiments conducted at $P = 1$ atm. for the free-standing LN crystal (Section 3.1). Indeed, when the CAP arrives at a mechanically free surface, the strain reflection coefficient is $r_{LN/air}^{ac} = -1$, hence preventing any CAP to be detectable because of the change of sign between the incident and reflected acoustic strain pulse canceling each other at the boundary.

Then, for the above listed parameters, the TDBS signals are presented in Figs. 13(a) and (b) with increasing inclination angle $\alpha \in [0, 10]°$, without (a) and with (b) normalization by the maximum of the signal. The meaning of the colored solid lines and of the black dashed lines are the same as in Fig. 12. Fig. 13 reveals that, when the inclination angle increases, the TDBS signals with the dominating BOs are transformed into the signals with dominating CAP profile. The strong diminishing of the signal amplitude with increasing α is also noticeable, as well as the shift towards earlier time for the time of arrival of the CAP as α increases. The former effect is a combination of the overlap mismatch both in real- and k-spaces which increases as α increases. The latter effect can be ascribed to the fact that the delayed time $\tau = t - \frac{H}{v_1 \cos \alpha}$ introduced in the theory indeed shifts the time
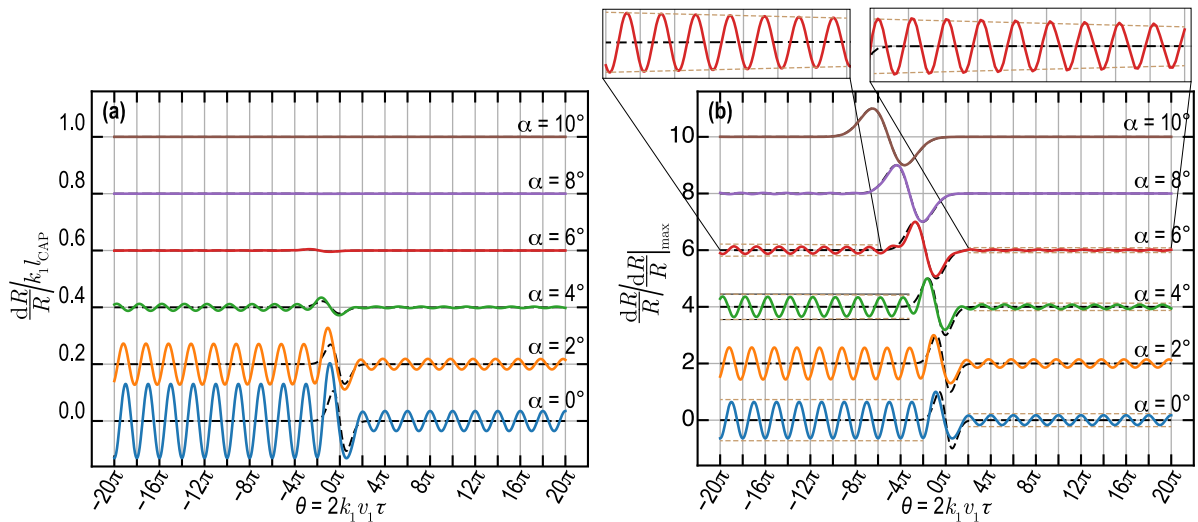

Fig. 13. Theoretical TDBS signals $\frac{dR}{R}$, normalized by (a) $k_1 l_{CAP}$ and (b) $\frac{dR}{R}\big|_{max}$, as a function of $\theta = 2k_1 v_1 \tau$, for different inclination angle α from 0 to 10°. The black dashed lines stand for the asymptotic case $k_1 l_{CAP} \to +\infty$, *i.e.*, for the case of the CAP profile only, corresponding to the limiting case of a CAP so long that it has negligibly small spectral amplitude at Brillouin frequency.

axis by the time of flight taken by the central ray of the CAP Gaussian beam to cover the distance from the Ti transducer to the LN/diamond interface. Yet, the lateral dimension of the CAP beam is not zero and increasing α leads to an earlier arrival of part of the CAP wavefront to the interface, hence an earlier interaction of the CAP and probe beams, which translates in Eqs. (2) and (4) into the expression of the real part of the argument in the erf function. Note that for small inclination angle, $\alpha < 8°$, the apparent asymmetry of the CAP profile seen on the TDBS signal is due to the superposition to form the signal of the CAP feature and BOs features. This also demonstrates, as discussed before, the difficulty one can face while trying to extract l_{CAP} directly "by eyes" from the experimental TDBS results. Not only this measurement will be biased by the superposition with the BOs, but the apparent CAP length increases with increasing inclination angle, precluding the feasibility of such naive and direct extraction of the CAP length.

Last but not least, the dependence of the TDBS signal on the thickness H, apart from the obvious dependence of the above-discussed temporal shift on H yet keeping a constant shape of the signals, is illustrated in the insets of Fig. 13(b). In those insets, the dashed–dotted lines before and after the CAP arrival time on the interface stand for the decay in amplitude controlled by the Gaussian factor $\exp\left\{-2\left[\frac{v_1}{l_B(\alpha)}\left(\tau + \frac{H}{v_1\cos\alpha}\right)\right]^2\right\}$, common to the contribution of incident and reflected CAP (see Eqs. (2) and (4)), that describes the diminishing of the BOs amplitude when approaching the reflecting (LN/diamond) interface and observed experimentally. The physical reason is the diminishing of the spatial overlap between the CAP and probe beams when the CAP approaches this interface for $\alpha \neq 0$, i.e., the shift of the CAP incidence spot relative to the probe spot (see Fig. 9), which increases with increasing α and is accounted for in our new formulas. The larger H and/or α, the stronger this effect. Note that the decay in amplitude after the CAP reflection deviates from the trend ascribed to the diminishing overlap, which might be due to the different directions of the light beam scattered by the incident or reflected CAPs: the position of the acoustically scattered beam after the CAP reflection will be always closer to the heterodyning light beam than its position before the CAP reflection from the interface. Further analysis, beyond the scope of this paper, is needed for deeper understanding of this effect.

The most striking effect of α on the TDBS signals is the change in the ratio between the amplitude associated to the CAP feature and the BOs amplitude, the ratio increasing with α. The significant dependence of the TDBS signals on the inclination angle α demonstrates that we can try to estimate the experimental α, locally, from the fit of an individual experimental TDBS signal measured from the LN side of the sample. The developed theory is oversimplified compared to the real complexity of the experimental geometry, as it is restricted to: (i) model a single channel of heterodyning expected to dominate in the right side of the sample for signals acquired from the LN side, (ii) account for the inclination of the Ti transducer only, (iii) consider that the strain reflection coefficient does not depend on α (partly true for small α variation), and (iv) disregard any effect of optical anisotropy in LN despite the uniaxial load to which the sample is subjected that might induce stress-related optical anisotropy and/or potential optical axis rotation upon pressure-induced sample degradation. Hence, the following estimations of α are meant to demonstrate this possibility more than to state the exact quantitative evaluation of α.

To perform the fit of a given experimental TDBS signal using the here-developed model, the slowly-varying background of the raw signal is filtered out by using 6th-order Butterworth band-pass filter (between 10 and 150 GHz). The fit is performed using the python module lmfit for non-linear least-squares minimization and curve fitting [69]. The model with non-dimensional parameters is used (see Eq. (5) for the part associated with the incident CAP and a similar expression for that associated with the reflected part), over a time window on the experimental data spanning from -0.2 to $+0.2$ ns around the CAP

arrival time at the LN/diamond interface. The following parameters are assumed to be known and fixed (see Tables 1 and A.2): $\lambda_{probe} = 535$ nm, $a = 1.25$ μm, ρ_{LN}, $n_{LN} = 2.295$ (mean of ordinary and extraordinary indices), $\rho_{water-ice}$, $n_{water-ice}$, ρ_C, v_C, and v_{Ti}.

In order to account for a thin layer of water-ice VII between the LN crystal and the diamond anvil, the complex strain reflection coefficient is assumed to be given by:

$$r_{LN/C}^{ac} = \frac{r_{01}e^{-j\varphi} + r_{12}e^{j\varphi}}{e^{-j\varphi} + r_{01}r_{12}e^{j\varphi}},$$

where $\varphi = k_{water-ice}^{ac}h_{water-ice}$ stand for the characteristic phase shift of the acoustic wave in the water-ice layer of thickness $h_{water-ice}$, while $k_{water-ice}^{ac}$ is the acoustic wave number in the water-ice medium. In the expression of $r_{LN/C}^{ac}$, the strain reflection coefficients at the LN(0)/water-ice(1) and water-ice(1)/diamond(2) interfaces (r_{01} and r_{12}, respectively) are assumed to be known and fixed:

$$r_{01} = -\frac{\rho_{LN}v_{LN} - \rho_{water-ice}v_{water-ice}}{\rho_{LN}v_{LN} + \rho_{water-ice}v_{water-ice}},$$

$$r_{12} = \frac{\rho_C v_C - \rho_{water-ice}v_{water-ice}}{\rho_C v_C + \rho_{water-ice}v_{water-ice}},$$

with $v_{water-ice} = 9.03 \pm 0.49$ μm/ns taken to be the mean of the acoustic velocity range estimated in the polycrystalline water-ice layer between the Ti transducer and the diamond anvil, by means of a fitting procedure described in details in Appendix E. In the previous expressions of r_{01} and r_{12}, the value of v_{LN} is deduced from the local estimation of the BF in LN for each signal, assuming $\alpha = 7°$ (mean value estimated from the time of flight analysis, Section 3.2.1). Note that it is assumed that the water-ice layer is homogeneous without adding an additional angle of inclination. Accounting for inhomogeneity and additional inclination, although possible, is too cumbersome for the current manuscript in which the point is that the inclination angle can be reasonably revealed by fitting the signals. However, accounting for the water-ice layer between LN and diamond provides the opportunities to: (i) describe the phase shift seen in the experimental data between the BOs associated to the incident and reflected CAPs, impossible to describe with a real-valued acoustic reflection coefficient, and (ii) explain why the initial fits (not shown) with real-valued reflection coefficients were converging either to positive or negative values of the acoustic reflection coefficient.

The four parameters fitted in the model are finally α, H, φ, and $\Omega_B(0)$. The lmfit module allows to define parameters from an expression of other parameters, which is used to define the time shift, introduced in the theory while defining the delayed time τ, the strain reflection coefficient, and the product $k_1 l_{CAP}$ defined by: $k_1 l_{CAP} = k_1 v_{LN}\frac{h_{Ti}}{v_{Ti}} = \frac{h_{Ti}}{2v_{Ti}}\Omega_B(0)$. In the previous expression, h_{Ti} is the thickness of the Ti transducer at $P = 10.4$ GPa which has been estimated to decrease by 3.3% compared to the nominal value at atmospheric pressure [70], leading to $h_{Ti} = 67.7$ nm. We assume that the length of the CAP is controlled by the thickness of the Ti transducer.

Signals that are possible to fit with this model have to present both CAP feature and BOs around the time of CAP arrival at the LN/diamond interface, such as those shown in Figs. 7(a), (f), and (g). Within the TDBS signals acquired in the 3D TDBS measurements from the LN side, it appears that such signals are located in the upper left triangle of the sample, defined by the straight line connecting the bottom left measured point to the top right measured point of the 2D scan (Fig. 8). Figs. 14(a) and (b) depict two examples of the fitting results for the signals shown in Figs. 7(a) and (f), at positions $(x = 6$ μm, $y = 12$ μm) and $(x = 27$ μm, $y = 36$ μm), respectively. Fig. 14(c) shows a third signal at position $(x = 18$ μm, $y = 39$ μm). These signals are hence from the lower left, upper right and upper middle parts of the LN sample, respectively, with an expected different local thickness of LN, H, according to the echo arrival time map in Fig. 8(a) (echo arrival time is longer for the first and third points than for the second one), and a measured slightly lower Brillouin frequency for the first point than for the second and third ones (~ 63 GHz and ~ 63.2 GHz, respectively).
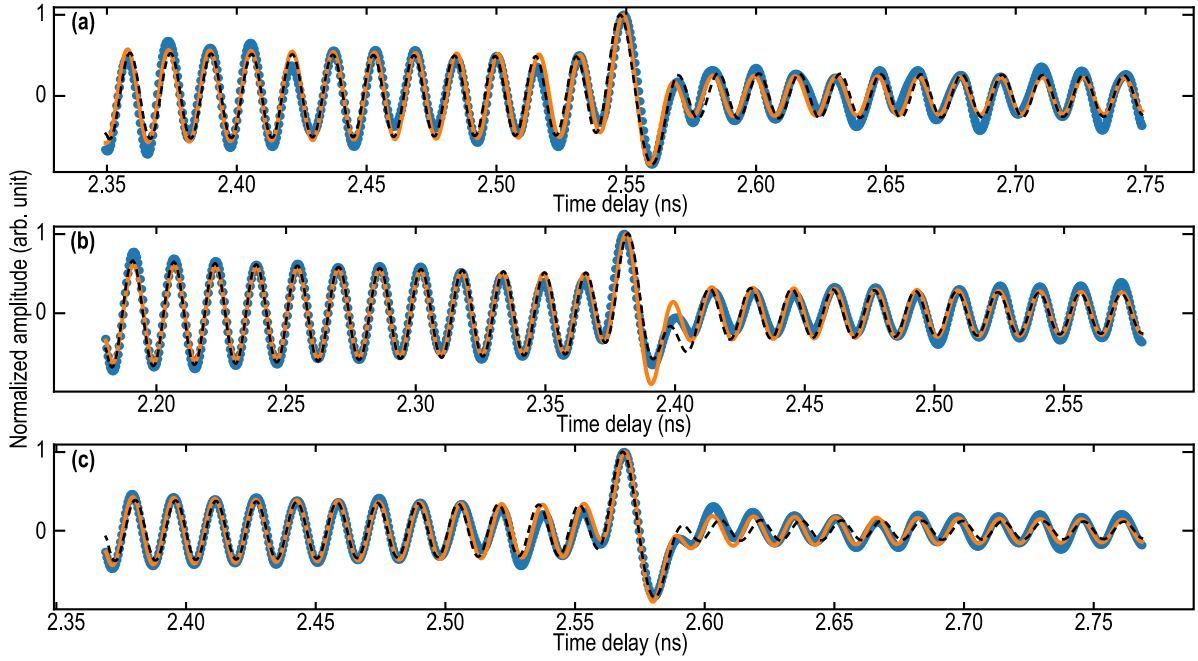
Fig. 14. Examples of fitted signals with complex valued (solid orange lines) or real valued (dashed black lines) strain reflection coefficient at positions: (a) ($x = 6$ μm, $y = 12$ μm), (b) ($x = 27$ μm, $y = 36$ μm), and (c) ($x = 18$ μm, $y = 39$ μm). The data are marked by blue disks in the figure.

In Fig. 14, the data are shown by the blue disks, the obtained fits by the orange solid lines, and the fits that do not account for the water-ice layer by the black dashed lines. The reduced chi-square values, giving a quantitative criterion of the goodness of the fit, are of 0.0084 (0.0169) for the result shown in solid (dashed) line in Fig. 14(a), of 0.0046 (0.0092) for the result shown in solid (dashed) line in Fig. 14(b) and of 0.0023 (0.0104) for the result shown in solid (dashed) line in Fig. 14(c). The improvement of the fit using the complete model accounting for the water-ice layer is mainly explained by a better match of phases, especially noticeable in Fig. 14(c). The fitted parameters, for the complete model, have values of $\alpha = 3.8°$, $H = 18.8$ μm, and $f_B(0) = 63.1$ GHz at ($x = 6$ μm, $y = 12$ μm); of $\alpha = 5.1°$, $H = 17.6$ μm, and $f_B(0) = 63.2$ GHz at ($x = 27$ μm, $y = 36$ μm); and of $\alpha = 5.55°$, $H = 19.0$ μm, and $f_B(0) = 63.3$ GHz at ($x = 18$ μm, $y = 39$ μm). The fitted local thicknesses are in good agreement with the echo arrival time map (Fig. 8(a)) and the Brillouin frequencies are consistent, since a small angle of inclination is not affecting much the BF value. The fitted values of φ vary for the three points and can lead, assuming the same local acoustic velocity in water-ice, to a very thin water-ice layer of about 11, 24, and 18 nm, respectively. Note that other signals have been fitted and that the water-ice layer thickness is seen not to vary much for neighbor points, consistent with our assumption of homogeneous water layer, at least locally. Note also that the difference in thicknesses might also be due to local varying acoustic velocity in water, the main point being that the water-ice might be slightly inhomogeneous but we do not think it is introducing a second angle of inclination at that LN/water-ice/diamond interface. For all presented fits, the value of l_{CAP} is 71 nm, 10 nm smaller than the value estimated "by eyes" previously.

In order to give an idea of the confidence interval on the values of α of the main interest here, the fits have been done by changing each fixed parameter in its own confidence interval in order to measure the influence of each parameter uncertainty on the value of α. This has been done over 159 points where the fitting procedure was possible and we have estimated that the locally estimated value of α can be trusted with a confidence of ±14% of its value, the most influential factor in this uncertainty being the acoustic velocity of Ti, assumed to be $\frac{\Delta v_{Ti}}{v_{Ti}} = ±10\%$. From the tested points, all located on the left triangle as said previously, the estimated inclination angles are shown to be in

the range between 3.5° and 7°, with a mean value of 5.6° and a standard deviation of 0.65°.

The theory, presented above in this Section 4, can be extended to provide the theoretical support for the qualitative interpretation of the TDBS signals in our experiments conducted from the Ti side in Section 3.2.2. The most important extension should account for the fact that, because of the small thickness of the water-ice layer, the two paths of heterodyning of the acoustically scattered light, *i.e.*, by the light reflected from the Ti transducer and from the diamond/water-ice interface (Fig. 9), are potentially effective simultaneously. The coherence length effect does not prevent this in contrast to the case of experiments conducted from the opposite side of the sample (Section 3.2.1). We do not think that the detailed theory, predicting the contributions of both CAP profile and BOs in the TDBS signal, is absolutely required for the estimates of the CAP arrival times on the surfaces of the water-ice layer in the experiments of Section 3.2.2, with further application to the evaluation of the lateral inhomogeneity of the layer thickness and of the inclinations of the Ti transducer. Sufficient for these purposes could be the estimates of the changes in the BO amplitude caused by the modification of the CAP propagation direction in reflection from the interfaces, confining the water-ice layer, and of the acoustic reflection coefficients at these interfaces. To predict the dependence of BO amplitude on the relative propagation angles of the probe, CAP and heterodyning beams, we extended the theory in [40], where the probe and heterodyning beams were anti-collinear, the CAP beam was at an angle α to both probe and heterodyning beams, and the interaction was far from the interfaces (in free space), to a more general situation where probe and heterodyning beams are not anti-collinear. For the case where the probe light and CAP propagate relative to the anti-collinear direction (opposite to the direction of heterodyning) at angles β and δ, respectively, both counted clockwise from the anti-collinear direction, we derived the following Gaussian factor controlling the amplitude of BO in TDBS signal: $D \cong \exp\left\{-\left(\frac{ka}{2}\right)^2 \frac{[\sin(\beta-\delta)-\sin\delta]^2}{2+\cos^2(\beta-\delta)+\cos^2\delta}\right\}$. In the derivation of this formula, we assumed that the CAP is delta-localized and that its radius is the same as the ones of the pump and probe beams. The latter approximation is very well satisfied for the rather small critical angles revealed by the estimates in Section 3.2.2. In the same approximation of small angles, the derived amplitude factor

can be approximated by $D \cong \exp\left\{-\left(\frac{ka}{4}\right)^2 [\sin(\beta-\delta)-\sin\delta]^2\right\}$. We apply this factor to compare the BOs amplitudes for different paths of heterodyning, as it has been discussed qualitatively in Section 3.2.2, via the evaluation of the divergence angles β and δ. Before the CAP reflection (Fig. 9(a)), the angles are $\beta = 2\alpha$ and $\delta = \pi + \alpha$ for the first heterodyning path, resulting in $D = 1$, while the angles are $\beta = 0$ and $\delta = \pi - \alpha$ for the second heterodyning path, resulting in $D \cong \exp\left[-\left(\frac{ka\sin\alpha}{2}\right)^2\right]$. Note that the latter result can be obtained, under the adopted assumptions, from the factor $\exp\left\{-\frac{[k_1 d(\alpha)]^2}{2}\right\}$ in Eq. (5), because the second path of heterodyning of the CAPs in water-ice VII is similar to the one assumed in Eq. (5), *i.e.*, with probe light beam direction anti-collinear to the heterodyning direction.

After the CAP reflection (Fig. 9(a)), the latter result for the second path does not change, *i.e.*, for the angles $\beta = 0$ and $\delta = \alpha$, while the result for the first path is significantly modified, as the angles are now $\beta = 2\alpha$ and $\delta = 3\alpha$, resulting in $D \cong \exp\left\{-\left(\frac{ka}{4}\right)^2 [\sin\alpha - \sin 3\alpha]^2\right\} \cong \exp\left[-4\left(\frac{ka\sin\alpha}{2}\right)^2\right]$. The derived expressions not only provide the opportunity to estimate the critical inclinations for significant diminishing of the TDBS signal, but also suggest the laws of the BOs amplitude changes with increasing α. They also provide the opportunity to estimate the transition angle α_{tr} when, with increasing α, the two heterodyning paths provide equal contributions to the TDBS signal. Neglecting the losses of the probe light transmission across the diamond/water-ice interface and back, the first heterodyning beam would be just $s \approx 3.2$ times stronger than the second, due to the difference in probe reflectivity at the water-ice/Ti and diamond/water-ice interfaces (estimated using properties listed in Table 1). Then the transition angle can be estimated from $3\exp\left[-3\left(\frac{ka\sin\alpha_{tr}}{2}\right)^2\right] = 1$, *i.e.*, $\sin\alpha_{tr} = \sqrt{\frac{\ln 3}{3}}\frac{\lambda_{probe}}{\pi a n_{water-ice}}$. The estimate results in $\alpha_{tr} \approx 0.05$, *i.e.*, $\alpha_{tr} \approx 2.9°$, confirming the expectations that the transition should take place before the disappearance of heterodyning via the first path, predicted in Section 3.2.2 to take place at $\alpha_{cr} \approx 3.3°$. Note, for comparison, that if the disappearance of heterodyning efficiency is defined at the level $D(\alpha = \alpha_{cr}) = 1/e^2$, then the above-derived formulas predict the disappearance of the first heterodyning path when $\alpha_{cr} \approx 3.4°$, demonstrating the validity of the simpler estimates undertaken in Section 3.2.2.

When the TDBS signals detected from the Ti side provide the opportunity to estimate the ratio of the BOs amplitude associated to the CAP propagating in the water-ice before and after the CAP reflection at the water-ice/diamond interface (reflection coefficient depicted by $r_{ice/C}^{ac}$), the suggested theoretical formulas provide the estimation of the Ti transducer inclination angles. As described above, the BOs amplitudes before and after the reflections are $A_< \approx \exp\left[-\left(\frac{ka\sin\alpha}{2}\right)^2\right] + s$ and $A_> \approx r_{ice/C}^{ac} \exp\left[-\left(\frac{ka\sin\alpha}{2}\right)^2\right] + s\exp\left[-4\left(\frac{ka\sin\alpha}{2}\right)^2\right]$, respectively. We remind that the s factor is the ratio of the heterodyning light amplitudes in the two channels. The ratio of the BOs amplitudes, *i.e.*, $A_</A_>$, contains a single unknown: the inclination angle α. For example, the examination of the signal presented in Fig. 10(c) suggests that, after the CAP reflection, the amplitudes of BOs in water-ice and LN are nearly equal (see after ~ 0.5 ns on the right part of Fig. 10(c) presenting the spectrogram). Thus, $A_>$ is half the beating amplitude. Before CAP reflection, $A_<$ is equal to the average of maximal and minimal amplitudes in the beating pattern, resulting in $A_</A_> \approx 3.3$, which is in good correlation with the estimates accomplished via the Fourier analysis ($A_</A_> \approx 3.1$). This leads to the estimation of the inclination angle of $\alpha \approx 2.3°$, which is smaller than the characteristic angles estimated above and therefore explaining the good detectability of the BOs after the CAP reflection at that specific location on the sample.

Using this approach of estimating the ratio $A_</A_>$ by a Fourier analysis, inclination angles α have been estimated at different locations on the sample using the signal acquired from the Ti side and where the amplitude of the BOs associated to the CAP propagating in the water-ice after the propagation was above the noise floor. These types of the signals were mainly located in the bottom right side of the sample, *i.e.*, where the previously discussed approach for estimating the inclination angles from the LN side is not applicable. The angles estimated on this bottom right part of the sample showed to be smaller than the one estimated from the LN side by the fit: $\alpha \lesssim 3.5 \pm 0.5°$, where the interval of confidence is mainly restricted by the estimation of the ratio $A_</A_>$ which depends on the window used for performing the Fourier transform around the CAP arrival time. Since the inclination angles estimated from the LN side are larger than about 4°, while the characteristic angle above which the CAP in the water-ice layer from the Ti side is expected to be undetectable is about 2.9–3.4°, this observation aligns well with all previously discussed estimates.

5. Discussions, conclusions and perspectives

The analytical theory from [40] is strongly required for the interpretation of uncommon observations in TDBS experiments, that can be due to lateral variations of the inclination angles. Indeed, the detections of TDBS signals depicting the Brillouin oscillations and the CAPs with comparable amplitudes when the CAP beam is incident on the optically probed plane interface between two transparent materials, are very unusual experimental observations. In fact, numerous TDBS experiments were earlier reported in thin single layers or multilayers of materials deposited/grown on the substrate, where the constitutive layers are of sub-micrometers to nanometers thicknesses. In these laterally homogeneous structures, the CAPs are launched by pump laser pulses absorption in one of the layers or in the substrate and the Brillouin oscillations can be caused by the CAPs traveling in one of the layer or simultaneously in several layers and/or substrate. The reflections of the CAPs at the surfaces/interfaces do not cause the variation in the BF [20,71–77], while the transmission of the CAPs across the interfaces can be accompanied by the variation in the BF and/or in the amplitude of the Brillouin oscillations [18,20,33–35,74,78–81]. However, the CAPs are usually not distinguishable inside the temporal intervals corresponding to CAPs reflections and transmissions, being "hidden" by the BOs whose amplitudes largely dominate the signals. The theory developed by us suggests that the above listed observations are due to the high parallelism of the surfaces and interfaces in the structures that are usually tested. The developed theory and our experimental observations indicate that the "hidden" CAPs can "emerge" and become comparable with BOs in amplitude if the detection of the BOs is suppressed by the deviation between the direction of the CAP beam, *i.e.*, the direction of the acoustically-scattered light, and the direction of the heterodyning probe beam. At the same time, it is worth noting another way to reveal the "hidden" CAPs. Earlier findings suggest that CAPs signals can be detected alongside BOs on the same signal when certain layers in the structure [82,83] or near-surface quantum wells [84,85] enable an efficient detection of these wide-frequency-band signals, thereby enhancing their detectability relative to that of the narrow-frequency-band BOs. Of course, the most known method enhancing the CAPs and suppressing the BOs, which was suggested by the initial theory of the detection in picosecond laser ultrasonics [24,25,74,86–88] and was realized experimentally [32], is the modification of the laser probe sensitivity function [24,25,86] through the variation of the probe wavelength in order to diminish the penetration depth of the probe light. In relation to this known tunability of the probe sensitivity, it is curious to mention that there are reported observations of the TDBS signals where the CAPs are visible together with the Brillouin oscillations [17,19,22] like in our experiments. However, the physical nature of these signals is completely different: the CAPs and the BOs are detected in two different materials forming the interface in the structure (for example, transparent and opaque), in which case the sensitivity function of the probe light is very different in different materials for the same probe wavelength. Note that, in Ref. [89], the

CAPs and the BOs are also detected in different spatially-separated parts of the structure.

Our observations of the CAPs only, *i.e.*, without BOs, also differ from the previously-reported works, although the observations of the CAPs arrivals on the surface/interface by the probe shifted laterally relative to the position of the pump and, thus, very inefficient in the detection of BOs, are rather common. However, the arrivals of the picosecond CAPs on the surface were only observed in opaque layers [19,90] or in transparent layers and structures, but only with the assistance of thin metallic films deposited on the surface [91,92] or incorporated in the structure [22].

The TDBS imaging revealed the lateral inhomogeneity of the plate thickness and related inclinations between the opposite surface of the plate, which provides opportunity to suggest plausible explanations for some features of the observed TDBS signals. For example, the observed absence of the features (CAPs or variations in BOs) in some lateral points, which corresponds to CAP crossing the plate once, or invisibility of CAP propagation in the right half of the plate, or even fast disappearance of the signal when the CAP is just emitted into the left part of the plate, could be partially explained purely geometrically by the diminishing overlap in space between the probe light beam and the CAP beam. Other types of signals, shown and discussed in Appendix D, incorporate features that are a clear sign of the LN crystal destruction such as the duration of the CAP propagation through the sample that change abruptly over a single lateral step of 1.5 μm. Another feature of sample splitting/cracking is the presence of two to several echoes in a single signal with a time delay between them shorter than that discussed previously in Section 3.2.3, which was the signature of the arrival of a second CAP (first propagating towards and reflected at the left water-ice/diamond interface before crossing the whole sample). Accurately quantifying the characteristics of this destruction (splits/cracks) requires conducting additional experiments, which is out of the scope of the current manuscript focusing in revealing the degradation of the LN crystal by the investigation of the inclination of the opposite surfaces extracted from TDBS signals.

We propose now to summarize the findings reported along the manuscript. We applied here the TDBS technique in order to monitor the degradation of a single crystal of LN to a polycrystal upon non-hydrostatic compression in a DAC. For the first time, the high pressure experiments were conducted in a DAC with the sample completely surrounded by another material, water-ice VII in our case. The experiments have been conducted from the two sides of the sample for allowing a better characterization of the sample shape through the interfaces. These opposite sides measurements have demonstrated the non parallelism of the interfaces compared to the diamond anvils which can be a general feature of high pressure experiments, even in the case of an hydrostatic loading. Using the different observations captured from the different measurements, several approaches have been used to reveal the inclination of the interfaces and qualitatively agree: analyses of time of flight and different analyses of the Brillouin oscillation amplitude variations, with a particular emphasis on the modification of the direction of the acoustically-scattered probe light relative to the direction of the reflected probe light heterodyning it. Note that, as a side product of our research, we have evaluated the dependence of the sound velocity in LN as a function of pressure (see Section 3.2.1.a and Appendix C for estimation at $P = 10.4$ GPa and $P = 3.8$ GPa, respectively). To our knowledge, we report here the first high-pressure experiments conducted on a birefringent sample. Although we initially chose the probe light polarization to avoid the effect of birefringence on our samples (beating), the non-hydrostatic deformation of the LN crystal, its rupture and local inclinations of crystal fragments together with their different levels of residual stress have led to the clear detection of birefringent effects in our 3D TDBS imaging experiments. The inclined geometry and the thickness of our sample, larger than the coherence length of the probe light, has also allowed us to elucidate several signal features of the time variation of the Brillouin oscillation

amplitude, such as the case where first the amplitude decreases and then increases again after crossing half the sample, to name but one feature. This lead to the understanding of the two possible channels of heterodyning in our sample, also at play at atmospheric pressure. Because of the challenging inclined geometry of our sample, we have further extended the analytical theory developed in [40] in order to describe the TDBS signals in the case of CAP propagation at an angle to the probe light and heterodyning direction. This theory accounts for both Brillouin oscillations and CAPs features in the signal, considers the CAP and probe light beam as finite Gaussian beam and include the effect of losing the spatial overlap between both beams. By fitting the experimental signals using this simplified, yet complete enough, model, we have demonstrated the possibility of evaluating the local inclinations of opposite surfaces of the sample. This type of local evaluation has been shown to agree quite well with other estimates of inclination provided all along the manuscript from different features.

The results and observations reported in this paper are numerous and pave the way to further extension of the use of the TDBS imaging technique to analyze the fascinating processes/phenomena occurring when materials are subjected to high pressure. Of course, further theory, to account for the here-neglected phenomena (elastic and optical anisotropy, acoustic and optical mode conversions, ...), as well as dedicated, more comprehensive signal processing technique are still to be developed in order to capture the complexity of such processes/phenomena and others. Yet, we believe that the TDBS technique will permit to extend our knowledge of single crystals to polycrystals evolution under plastic deformation. This information is of fundamental importance for several branches of the natural sciences, such as materials engineering, condensed-matter physics, physics of the Earth and planetology, as well as for the prediction of the consequences of earthquakes, tsunamis and explosions. The quantitative information obtained by the ASOPS-based 3D TDBS imaging technique on fracture, polycrystallization, and creep of materials with exceptional spatial resolution will extend the basis for successful development and application of highly developed micromechanical models of elastic and especially plastic deformation, which are necessary for the prediction of the behavior of the materials devoted to be used under extreme conditions such as ceramics.

Furthermore, the results presented in our research bear generality beyond the specific case of imaging of crystalline and polycrystalline materials and their evolution under the external mechanical loading or heating. They demonstrate that the TDBS technique can provide valuable information about medium inhomogeneity beyond the classical experimental geometries of samples with plane-parallel interfaces/layering, where both the probe light and CAPs are often treated as plane waves. Our experiments validate the theoretical expectations [40] that, in samples with inclined interfaces/layering, the TDBS signals depend on the radii of the probe light and CAP beams, as well as the length and profile of the CAP. The TDBS signals carry information about the interface distance(s) and inclination angle(s). Moreover, our experiments confirm the feasibility of TDBS experiments even when the acoustically scattered light propagates in a direction different from that of the heterodyning light. As a result, we discovered additional functionalities of the TDBS technique within the Rayleigh range of the probe light and CAP beams, which were applied for the first time to characterize sample spatial inhomogeneities. The application of the developed theoretical formalism is specially required for the understanding/interpretation of the TDBS signals that are detected when the CAP is overlapping/interacting with the interfaces inclined to its propagation direction. Our research results, along with the findings presented in [67], indicate that in the future, with efforts to overcome the increasing complexity in theoretical description and interpretation, the TDBS technique could be applied to the quantitative imaging of media with smooth spatial structuring, extending beyond the diffraction distances of the probe light and CAP beam. This application may not be limited to solids but could also be extended to liquids, as well as animal/biological tissues and cells.

Funding

Declaration of competing interest

The authors declare that they have no known competing financial interests or personal relationships that could have appeared to influence the work reported in this paper.

Data availability

Data will be made available on request.

Appendix A. Experimental parameters

In this appendix, the experimental parameters for each experimental condition tested using the JAX-M1 picosecond laser ultrasonics microscope are summarized in Table A.2.

Appendix B. Diminishing of the LN sample thickness with increasing pressure

In this appendix, we estimate the relative thickness change, $\delta H/H_0$, of our LN single crystal embedded in phase VII of water ice (H_2O-ice VII) and compressed in a DAC to $P = 10.4$ GPa. Because the thickness change is mostly controlled by the hydrostatic pressure, we used, at the first step, the equation of state (EOS) of LN [65]. Upon compression to $P = 10$ GPa, the volume of LN decreases by $\delta V/V_0 \sim 7\%$ and the thickness, accordingly, by $\delta H/H_0 \sim 2.4\%$. The latter value is nearly identical for any crystallographic direction in a $LiNbO_3$ single crystal because the crystal compressibility is nearly isotropic, i.e., the ratio of the lattice parameters c/a changes only insignificantly from 2.685 (at $P = 1$ atm.) to 2.715 (at $P = 10$ GPa). In order to estimate contribution of the non-hydrostatic/uniaxial stress component, t, we first had to compare yield strengths, σ_y, of H_2O-ice VII and of LN.

H_2O-ice VII is a high pressure phase not recoverable at atmospheric pressure and, for this reason, its σ_y is not established. However, the uniaxial stress component t' in a sample of H_2O-ice VII compressed in a DAC was reported to be $\sim 10\%$ of the measured pressure value [93], which corresponds to $t' \approx 1$ GPa in our experiment. The hardness of LN at atmospheric pressure was reported to be strongly anisotropic and vary, depending on the crystallographic orientation, between 5.3 GPa and 9.7 GPa. Taking the lowest hardness value and estimating it as $\sim 3\sigma_y$ [54], we obtained the yield strength for LN to be $\sigma_y \approx 1.77$ GPa, which is comparable with the uniaxial stress component t' in H_2O-ice VII at $P = 10$ GPa. Because one third of the uniaxial stress is already included in the hydrostatic pressure, the additional non-hydrostatic/uniaxial stress charging our single crystal of $LiNbO_3$ along the [001] direction is $t \approx 0.7$ GPa. Taking into account that Young's modulus of inorganic solids is typically greater than the bulk modulus, we applied the EOS reported in [65] and obtained the total change of thickness of our single crystal of LN plate to be $\delta H/H_0 \approx 2.5\%$. Thus, the thickness of the LN plate is expected to diminish from the nominal 20 μm to 19.5 μm, facilitating complete surrounding of LN plate by water ice between the diamond anvils, separated by 21.8 ∓ 0.3 μm.

Appendix C. On the experiments conducted with a fs Ti:sapphire laser at $P = 3.8$ GPa

The experimental TDBS signals presented in Fig. C.15(a) were accumulated from the LN side, i.e., when the pump and probe were incident on the Ti transducer through the LN. They correlate with those accumulated at $P = 1$ atm. and $P = 10.4$ GPa in terms of their overall structure, which reveals the presence of the maximal amplitudes of BOs when the CAP is in the vicinity of the faces of the LN sample, i.e., at delay times around 0 and 3 ns (Fig. C.15(a)). This confirms the role of the coherence effect, discussed in Sections 3.1 and 3.2.1. The spectra of the signals extracted in the time window from 0 to 2.9 ns (Fig. C.15(b)) indicate the effect of optical birefringence.

The evaluation of the signals in the vicinity of the CAP arrivals to the right face of the LN plate, presented in Fig. C.15(c), reveals a shift in the times of flight of the CAPs across the plate, which is less than 0.003 ns over the 20 μm-long scan. Sound velocity can be estimated by comparing the averaged measured BF of 37.5 GHz in Fig. C.15(c), assuming that the averaged refractive index of LN at 810 nm probe

Table A.2

Summary of experimental parameters for each experimental condition tested using the JAX-M1 picosecond laser ultrasonics microscope.

|				
Probe wavelength		535 nm		
Pump wavelength		517 nm		
Probe repetition frequency		42 MHz		
Pump repetition frequency		42.0005 MHz		
Pulse duration		< 130 fs		
Experimental condition	Atmospheric pressure ($P \simeq 0$ GPa)		Non-hydrostatic loading ($P \simeq 10.4$ GPa)	
TDBS experiment type	1D	2D	2D	3D
Number of points	1	12	12	24 × 32 (LN side) 26 × 32 (Ti side)
Lateral separation between points	–	2 μm	2 μm	1.5 μm
Probe polarization angle with respect to optical axis of LN	0°, 45°, 90°, 135°	0°		0°
Pump power		4 mW		6 mW
Probe power		4 mW		6 mW
Beam diameter ($1/e^2$)		2.5 μm		
Number of averages per point		30,000		
Acquisition time for 1000 averages		2 s		
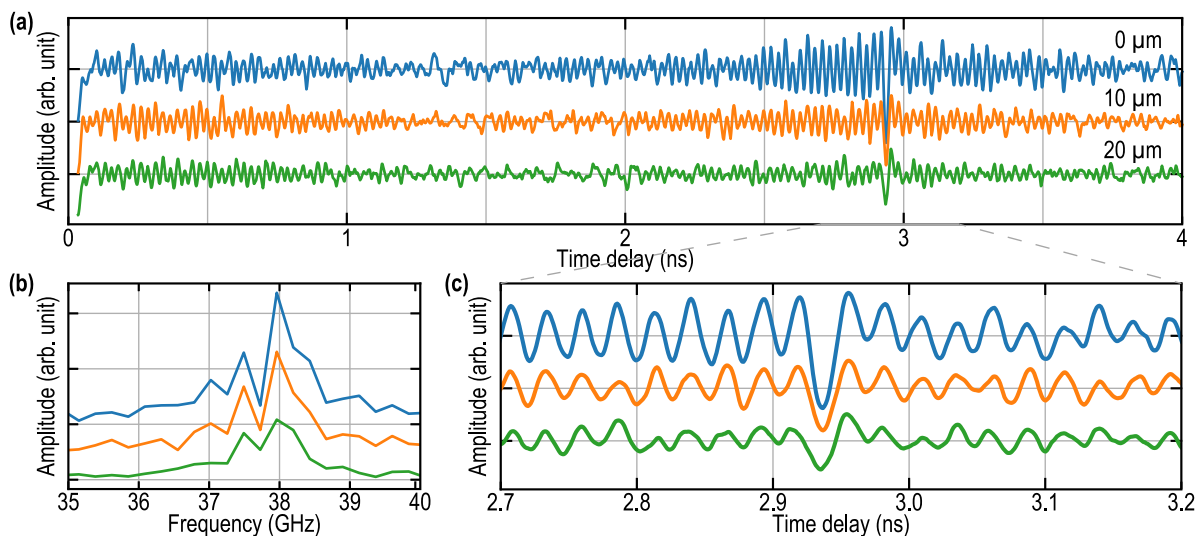
Fig. C.15. (a) TDBS signals in the 2D TDBS experiments, detected from the LN side of the sample compressed at $P = 3.8$ GPa and where the measurements were conducted with a step of 10 μm. (b) Frequency spectra of the BOs extracted in the time window from 0 to 2.9 ns. (c) Zoom in of the detected signals near the reflection moments of the laser-generated CAP at the right face of the LN plate. The blue, orange and green colors of the lines correspond to the positions of the scan at 0, 10 and 20 μm, respectively. The signals in (a), (b) and (c) are vertically shifted to facilitate their comparison.

wavelength is about 2.21 (2.17–2.25) [41,56]. The estimated $v_{LN}(P = 3.8$ GPa) = 6.87 μm/ns is 5% higher than that measured at atmospheric pressure in Section 3.1, $v_{LN}(P = 1$ atm.) = 6.56 μm/ns. This provides opportunity to estimate the thickness variation of about 0.023 μm along the scan and an inclination angle of less than 0.06°, revealing no significant changes relative to the inclination at $P = 1$ atm., estimated in Section 3.1.

Appendix D. Correlations of the optical and TDBS images: signatures of LN crystal splitting/cracking

In this appendix, we investigate the correlation between the optical images of the destructed LN sample and the features observed in 3D TDBS imaging. The destruction of the LN single crystal at $P = 10.4$ GPa, caused by non-hydrostatic loading and revealed by the appearance of lateral inhomogeneity in the optical image (Fig. 3(c) and Fig. D.16(a)), manifests itself in multiple specific features in the TDBS signals, such as the lateral inhomogeneity of the measured Brillouin frequency (see the BF maps in Figs. 8(b) and (c)) and the duration of the CAP propagation through the sample (see the map of the arrival times in Fig. 8(a) and Fig. D.16(c)). Furthermore, overlaying the optical image with the arrival time map (Fig. D.16(b)) demonstrates that the boundaries of the LN crystal destruction (presumably the signatures of LN crystal splitting or cracking) align with the boundaries of arrival time clusters.

The point-to-point analysis of the TDBS signals along these discussed boundaries strengthens the above hypothesis. In the vicinity of these boundaries, the TDBS signals often exhibit the detection of two to several echoes in a single lateral position (Figs. D.16(d) and (e)) or an abrupt and significant change in the measured arrival time of CAPs just after a single lateral step of 1.5 μm (Figs. D.16(f) and (g)). The detection of two significantly different CAP arrival times (*e.g.*, middle signal in Fig. D.16(d) or two upper signals in Fig. D.16(e)) is a clear signature of the simultaneously generated CAPs propagating simultaneously along two opposite sides of the LN crystal split, which are very differently stressed. The TDBS signals containing more than two echo arrivals (*e.g.*, middle signal in Fig. D.16(e)) can be associated with intersection of cracks. The signals in Figs. D.16(d)–(g) demonstrate that the difference in the CAP propagation times along the opposite sides of the LN crystal split can be on the order of 0.05 ns. Furthermore, Fig. D.16(e) illustrates a maximum time difference of 0.175 ns, which is approximately 2 to 7% of the characteristic time for the CAP to cross the LN sample.

Such a strong variation cannot be associated with the pressure-induced difference of LN parameters on the opposite faces, because the pressure values are expected to be nearly equal in the points separated by 1.5 μm or less lateral distances. Therefore, presumably, the effect is caused by differences in thicknesses of the crystal fragments due to different levels of residual stresses on the opposite sides of the splits inducing very different residual deformation. This would result in significantly different propagation path lengths of the CAPs along the opposite sides of the crystal split. As our experimental observations demonstrated that the thickness of water-ice VII, that is captured between the LN and diamond, is definitely sub-micrometric, not exceeding 50 nm according to our estimate (Section 4), the μm-sized jumps in the crystal thickness can only be accommodated by the water-ice layer between the diamond anvil and the Ti transducer which estimated thickness can be more than one order of magnitude larger. Such splitting of the LN crystal requires splitting and displacement of the Ti transducer.

Accurately quantifying the characteristics of this destruction (splits/cracks) requires conducting additional scans around the destruction boundaries with improved lateral spatial resolution. However, as these investigations extend beyond the scope of the present paper, they will be addressed in future studies. The major goal of the present work is different, *i.e.*, revealing degradation of the LN crystal via the validated inclination of the opposite surfaces which can be extracted from TDBS signals.

Appendix E. On the properties of the polycrystalline water-ice VII at $P = 10.4$ GPa

Although the evaluation of the state of the polycrystalline water-ice VII confined between the diamond anvil and the Ti transducer was not among the goals of the conducted research, we evaluated the 2D-map of the BFs in this layer with better quantification of the error than in Sections 3.2.1–3.2.2 (Figs. 8(c) and (d)) in order to conclude on its lateral heterogeneity and composition. Precise evaluation of the Brillouin frequencies is complicated because this squeezed water-ice is polycrystalline and, thus, could be inhomogeneous in depth, while the time window for the determination of the BOs frequency, even averaged over the layer thickness, is limited by a rather short time of flight of the CAP propagating between the Ti transducer and the diamond anvil. Because acoustic impedances of water-ice VII, Ti and LN match very well, the duration of the BOs in water-ice cannot significantly
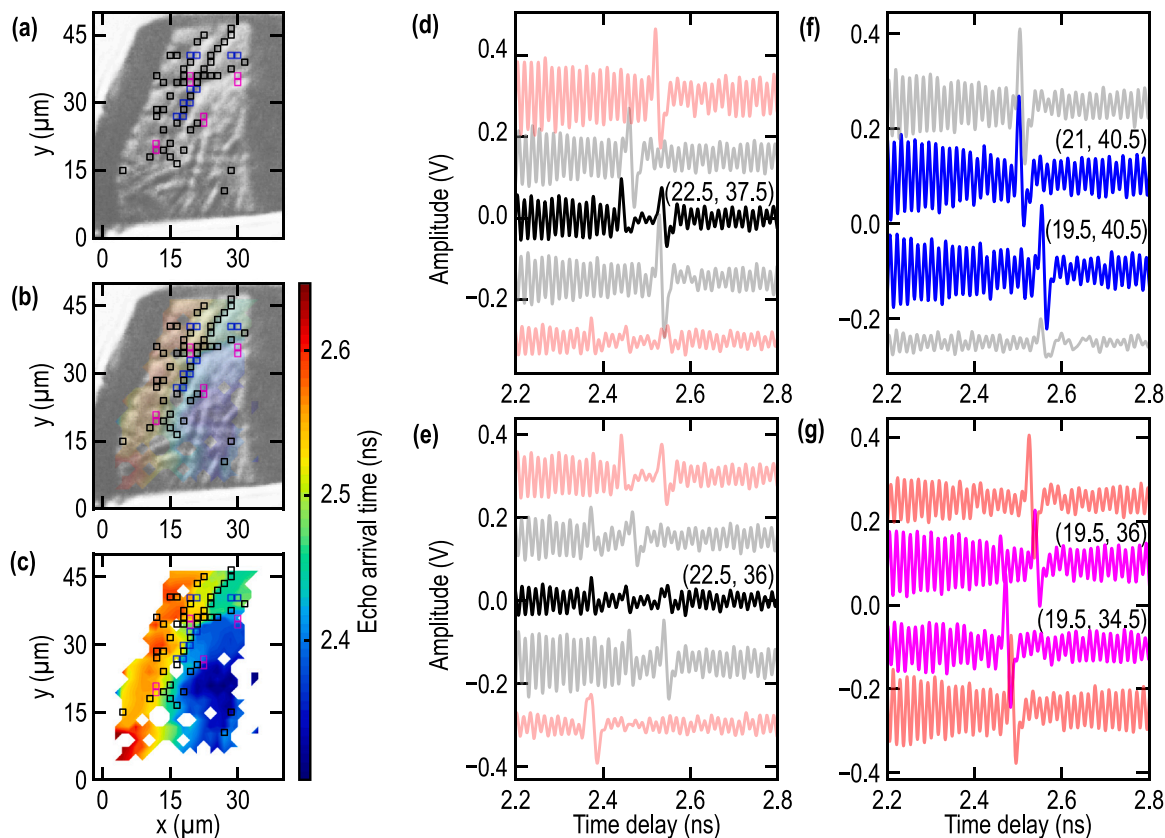
Fig. D.16. Illustrating the signatures of LN crystal splitting/cracking: (a) Optical image of LN at $P = 10.4$ GPa, converted to grayscale and contrast corrected. (b) Interpolated map of echo arrival time (Fig. 8(a) of the main text and reproduced in (c)) superimposed with the optical image shown in (a). (c) Interpolated map of echo arrival time, as measured from the LN side. (d)–(e) Examples of signals with multiple echoes shown as solid black lines, accompanied by surrounding points. Light gray points represent adjacent points along the *x*-direction, while light red points represent points along the *y*-direction in the 3D scan. The lighter colors below the black curve indicate points one step down, and the lighter colors above the curve indicate points one step up. (f) Solid blue lines represent abrupt jumps in the arrival time with a single step of 1.5 μm along the *x*-direction. Light gray signals indicate adjacent points along the same direction. (g) Solid magenta lines represent abrupt jumps in the arrival time with a single step of 1.5 μm along the *y*-direction. Light red signals indicate adjacent points along the same direction. The positions of the signals from the 3D scan depicting the same features as that of the solid black, blue, and magenta lines in (d)–(g) are represented as open squares with their respective colors in the left-side maps/images.

exceed the time for the CAP to cross this layer twice. Furthermore, an additional complexity arises in our experiments from the simultaneous detection of the BOs in LN, with BFs rather close to those in water-ice VII, which results in a beating phenomenon in the TDBS signal (Sections 3.2.1 and 3.2.2). To disentangle the BFs of water-ice VII from those of LN, we have applied the following fitting procedure. A signal that results from the mixing of two frequencies is modeled as the sum of two cosines modulated by a decreasing exponential on the first 400 ps. This model consists of seven parameters: the amplitude, frequency, and phase for each cosine, and the attenuation parameter for the exponential. To fit the signals, a non-linear least square method is used with the `curve_fit` function from the `scipy` Python library [94]. The first and second cosine parameters are constrained to the LN and water-ice VII Brillouin frequency (f_B) ranges, respectively, such that $f_B \in [60 - 69]$ GHz for the LN and $f_B \in [50 - 59]$ GHz for the water-ice VII. To evaluate the error of the fit, the residual normalized energy is calculated, and signals with more than 0.1 residual energy are rejected. The covariance matrix obtained from the least squares fit provides the estimation of the standard deviation for each parameter, indicating the error made on each parameter. The interval of confidence is set at two times the standard deviation. The average error on the frequency for the water-ice VII estimated from measurements done on the Ti side is ± 0.15 GHz, while the average error for that estimated from measurements done on the LN side is ± 1.4 GHz. The larger error in the

later case is due to the low amplitude of the component in the TDBS signal associated to the CAP propagating in the water-ice VII layer seen (probed) from the LN side.

In Fig. E.17(a)–(b), we present the BFs distributions in water-ice VII extracted from the experimental signals detected from the LN side and from the Ti side, respectively. Comparison of both distributions demonstrates a high level of correlation between the results obtained with TDBS measurements from opposite sides. The frequency distribution histogram (Fig. E.17(c)) illustrates a shift of approximately 1 GHz in the frequency distributions, which, however, is within the error of the BF determination from the LN side. The range of the measured BFs from ~ 50.5 to ~ 58.5 GHz (Fig. E.17(c)) provides opportunity to estimate the range of the acoustic velocities in this polycrystalline water-ice layer. The refractive index at our green probe wavelength, $n_{\text{water-ice}} \approx 1.63 \pm 0.01$, of the optically isotropic water-ice VII at $P = 10.4$ GPa can be obtained from the linear extrapolation of the data presented in [59,64] only up to 7 and 7.5 GPa, respectively, and agrees with [53]. Therefore, the longitudinal velocities of the water-ice VII in our observations can be estimated as $v_{\text{water-ice}} = \lambda_{BO} f_B^{\text{water-ice}} = \frac{\lambda_{\text{probe}} f_B^{\text{water-ice}}}{2 n_{\text{water-ice}}} \approx 8.3$-9.6 μm/ns. This velocity range is nearly entirely above the range of the velocities of water-ice VII, $v_{\text{water-ice}} \approx 6.03$-8.6 μm/ns, reported earlier for the significantly thicker (30 μm) water-ice VII layer squeezed between two diamond anvils [29]. It contains the velocities in the single
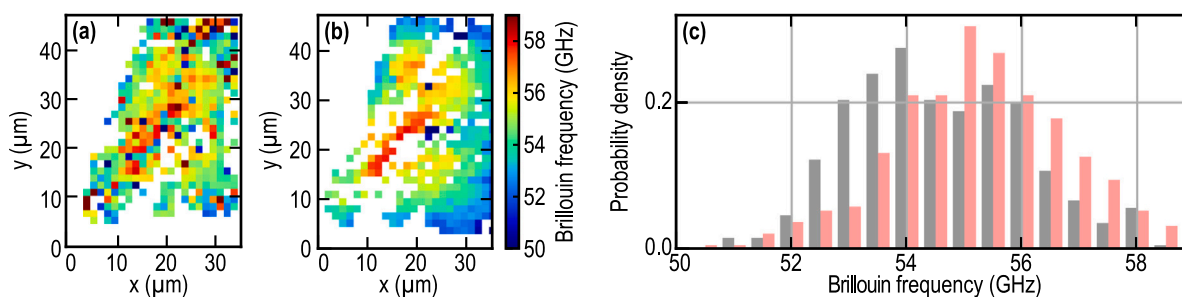
Fig. E.17. Water-ice VII Brillouin frequency maps extracted using a least squares fit method on the TDBS signals detected from the LN side (a) and from the Ti side (b) where direction of the *x*-axis was mirrored in order to make the comparison with (a) easier. (c) Histogram of the Brillouin frequency distributions revealed from the LN side (in red) and from the Ti side (in gray).

crystal water-ice VII along $\langle 110 \rangle$ and $\langle 111 \rangle$ directions and not the velocity along $\langle 010 \rangle$ direction, $v_{\langle 110 \rangle}^{\text{water-ice}} \approx 8.0$ μm/ns, $v_{\langle 111 \rangle}^{\text{water-ice}} \approx 8.5$ μm/ns and $v_{\langle 010 \rangle}^{\text{water-ice}} \approx 7.0$ μm/ns, respectively, which can be estimated by linear extrapolation of the data presented in Fig. 3 of [95] for single crystal of water-ice VII and from Ref. [29]. Further interesting experimental result for the dedicated analysis and physical interpretation in the future is the revealed lateral inhomogeneity of the ice texture, with tendency of a larger amount of "fast" crystallites (with higher BFs) closer to the center of the LN plate and a larger amount of "slow" crystallites (with lower BFs) near the LN plate edges (Figs. E.17(a) and (b)). This effect is better revealed by the TDBS experiments from the Ti side (Fig. E.17(b)), because in these experiments the BOs in the water-ice were dominated over those in the LN in the fitted temporal window.

These observations could be fully explained by a strong pressure gradient in the thin ice layer between the diamond and the hard LN crystal: if we agree that the highest longitudinal acoustic velocity in the central part of the ice layer (around the coordinates $x = 20$ μm and $y = 20$ μm) corresponds to $v_{\langle 111 \rangle}^{\text{water-ice}} \approx 9.5$ μm/ns then the pressure in this point should be $P \approx 13$ GPa [29] while the pressure just at the crystal edge is $P = 10.4$ GPa, revealing the inhomogeneity of the pressure lateral distribution caused by the non-hydrostatic loading of the LN crystal. Taking the characteristic distance to the LN-edge of d$l = 10$ μm, we obtain: d$P/$d$l = (13 - 10.4)$ GPa/10 μm = 0.26 GPa/μm. This permits the extraction of the yield strength of the water-ice VII, $\sigma_y = 0.6$ GPa, using the well-known expression d$P/$d$l = \sigma_y/h$ (*e.g.*, p. 21 in [96]), where $h = 2.3$ μm is the water-ice layer thickness. The here-obtained $\sigma_y = 0.6$ GPa for the water-ice VII agrees reasonably well with the value earlier measured at $P = 10$-14 GPa, $\sigma_y = 0.5$-0.8 GPa, using radial X-ray diffraction (XRD) [97]. Because the velocities corresponding to the $\langle 010 \rangle$ direction in water-ice VII at $P = 13$ GPa, $v_{\langle 010 \rangle}^{\text{water-ice}} = 6.95$ μm/ns, were not detected in the central region of the ice layer, we expect the preferred orientation (texture) of the water-ice crystals with the axis $\langle 111 \rangle$ along the DAC axis and the sound wave propagation direction. Thus, we have experimentally confirmed that the pressure gradient in a DAC is back-proportional to the sample thickness as well as the earlier estimation of σ_y of water-ice VII from XRD measurements. Moreover, we have accidentally discovered a method to measure pressure dependencies of yield strengths of transparent cubic solids, $\sigma_y(P)$, to very high pressures.

References

[1] R.J. Dewhurst, C. Edwards, A.D.W. McKie, S.B. Palmer, A remote laser system for ultrasonic velocity measurement at high temperatures, J. Appl. Phys. 63 (4) (1988) 1225–1227, http://dx.doi.org/10.1063/1.339987.

[2] C.B. Scruby, L.E. Drain, Laser Ultrasonics Techniques and Applications, CRC Press, 1990.

[3] K. Telschow, Material property measurement in hostile environments using laser acoustics, in: IEEE 2004 Ultrasonics Symposium, Vol. 1, 2004, pp. 662–671, http://dx.doi.org/10.1109/ULTSYM.2004.1417811, ISSN: 1051-0117.

[4] R.S. Schley, K.L. Telschow, J.B. Walter, D.L. Cottle, Real-time measurement of material elastic properties in a high Gamma irradiation environment, Nucl. Technol. 159 (2) (2007) 202–207, http://dx.doi.org/10.13182/NT07-A3865.

[5] L. De Dominicis, M. Carta, M. Ciaffi, L. Falconi, M. Ferri de Collibus, M. Francucci, M. Guarneri, M. Nuvoli, F. Pollastrone, Radiation tolerant 3D laser scanner for structural inspections in nuclear reactor vessels and fuel storage pools, Sci. Technol. Nucl. Ins. 2021 (2021) e8237946, http://dx.doi.org/10.1155/2021/8237946.

[6] A. Jayaraman, Diamond anvil cell and high-pressure physical investigations, Rev. Modern Phys. 55 (1) (1983) 65–108, http://dx.doi.org/10.1103/RevModPhys.55.65.

[7] N. Dubrovinskaia, L. Dubrovinsky, N.A. Solopova, A. Abakumov, S. Turner, M. Hanfland, E. Bykova, M. Bykov, C. Prescher, V.B. Prakapenka, S. Petitgirard, I. Chuvashova, B. Gasharova, Y.-L. Mathis, P. Ershov, I. Snigireva, A. Snigirev, Terapascal static pressure generation with ultrahigh yield strength nanodiamond, Sci. Adv. 2 (7) (2016) e1600341, http://dx.doi.org/10.1126/sciadv.1600341.

[8] J.M. Brown, L.J. Slutsky, K.A. Nelson, L.-T. Cheng, Velocity of sound and equations of state for methanol and ethanol in a diamond-anvil cell, Science 241 (4861) (1988) 65–67, http://dx.doi.org/10.1126/science.241.4861.65.

[9] B.J. Baer, J.M. Brown, J.M. Zaug, D. Schiferl, E.L. Chronister, Impulsive stimulated scattering in ice VI and ice VII, J. Chem. Phys. 108 (11) (1998) 4540–4544, http://dx.doi.org/10.1063/1.475882.

[10] E.H. Abramson, J.M. Brown, L.J. Slutsky, Applications of impulsive stimulated scattering in the earth and planetary sciences, Annu. Rev. Phys. Chem. 50 (1) (1999) 279–313, http://dx.doi.org/10.1146/annurev.physchem.50.1.279.

[11] J.C. Crowhurst, E.H. Abramson, L.J. Slutsky, J.M. Brown, J.M. Zaug, M.D. Harrell, Surface acoustic waves in the diamond anvil cell: An application of impulsive stimulated light scattering, Phys. Rev. B 64 (10) (2001) 100103, http://dx.doi.org/10.1103/PhysRevB.64.100103.

[12] J.C. Crowhurst, A.F. Goncharov, J.M. Zaug, Impulsive stimulated light scattering from opaque materials at high pressure, J. Phys.: Condens. Matter 16 (14) (2004) S1137, http://dx.doi.org/10.1088/0953-8984/16/14/023.

[13] S.A. Akhmanov, V.É. Gusev, Laser excitation of ultrashort acoustic pulses: New possibilities in solid-state spectroscopy, diagnostics of fast processes, and nonlinear acoustics, Sov. Phys. Usp. 35 (3) (1992) 153, http://dx.doi.org/10.1070/PU1992v035n03ABEH002221.

[14] N. Chigarev, P. Zinin, L.-C. Ming, G. Amulele, A. Bulou, V. Gusev, Laser generation and detection of longitudinal and shear acoustic waves in a diamond anvil cell, Appl. Phys. Lett. 93 (18) (2008) 181905, http://dx.doi.org/10.1063/1.3013587.

[15] N. Chigarev, P. Zinin, D. Mounier, A. Bulou, A. Zerr, L.C. Ming, V. Gusev, Laser ultrasonic measurements in a diamond anvil cell on Fe and the KBr pressure medium, J. Phys.: Conf. Ser. 278 (1) (2011) 012017, http://dx.doi.org/10.1088/1742-6596/278/1/012017.

[16] M.R. Armstrong, J.C. Crowhurst, E.J. Reed, J.M. Zaug, Ultrafast high strain rate acoustic wave measurements at high static pressure in a diamond anvil cell, Appl. Phys. Lett. 92 (10) (2008) 101930, http://dx.doi.org/10.1063/1.2898222.

[17] F. Decremps, L. Belliard, B. Perrin, M. Gauthier, Sound velocity and absorption measurements under high pressure using picosecond ultrasonics in a diamond anvil cell: Application to the stability study of alpdmn, Phys. Rev. Lett. 100 (3) (2008) 035502, http://dx.doi.org/10.1103/PhysRevLett.100.035502.

[18] S.M. Nikitin, N. Chigarev, V. Tournat, A. Bulou, D. Gasteau, B. Castagnede, A. Zerr, V.E. Gusev, Revealing sub-μm and μm-scale textures in H2O ice at megabar pressures by time-domain Brillouin scattering, Sci. Rep. 5 (1) (2015) 9352, http://dx.doi.org/10.1038/srep09352.

[19] F. Decremps, M. Gauthier, S. Ayrinhac, L. Bove, L. Belliard, B. Perrin, M. Morand, G. Le Marchand, F. Bergame, J. Philippe, Picosecond acoustics method for measuring the thermodynamical properties of solids and liquids at high pressure and high temperature, Ultrasonics 56 (2015) 129–140, http://dx.doi.org/10.1016/j.ultras.2014.04.011.

[20] M. Kuriakose, N. Chigarev, S. Raetz, A. Bulou, V. Tournat, A. Zerr, V.E. Gusev, In situ imaging of the dynamics of photo-induced structural phase transition at high pressures by picosecond acoustic interferometry, New J. Phys. 19 (5) (2017) 053026, http://dx.doi.org/10.1088/1367-2630/aa6b3d.

[21] S. Sandeep, T. Thréard, E. De Lima Savi, N. Chigarev, A. Bulou, V. Tournat, A. Zerr, V.E. Gusev, S. Raetz, 3D characterization of individual grains of coexisting high-pressure H_2O ice phases by time-domain Brillouin scattering, J. Appl. Phys. 130 (5) (2021) 053104, http://dx.doi.org/10.1063/5.0056814.

[22] S. Boccato, M. Gauthier, N.C. Siersch, P. Parisiades, Y. Garino, S. Ayrinhac, S. Balugani, C. Bretonnet, T. Delétang, M. Guillot, K. Verbeke, F. Decremps, Y. Guarnelli, M. Morand, P. Rosier, B. Zhao, D. Antonangeli, Picosecond acoustics: a new way to access elastic properties of materials at pressure and temperature conditions of planetary interiors, Phys. Chem. Mineral. 49 (6) (2022) 20, http://dx.doi.org/10.1007/s00269-022-01194-6.

[23] S. Li, Z. Qin, H. Wu, M. Li, M. Kunz, A. Alatas, A. Kavner, Y. Hu, Anomalous thermal transport under high pressure in boron arsenide, Nature 612 (7940) (2022) 459–464, http://dx.doi.org/10.1038/s41586-022-05381-x.

[24] C. Thomsen, H.T. Grahn, H.J. Maris, J. Tauc, Picosecond interferometric technique for study of phonons in the Brillouin frequency range, Opt. Commun. 60 (1) (1986) 55–58, http://dx.doi.org/10.1016/0030-4018(86)90116-1.

[25] H. Grahn, H. Maris, J. Tauc, Picosecond ultrasonics, IEEE J. Quantum Electron. 25 (12) (1989) 2562–2569, http://dx.doi.org/10.1109/3.40643.

[26] V.E. Gusev, P. Ruello, Advances in applications of time-domain Brillouin scattering for nanoscale imaging, Appl. Phys. Rev. 5 (3) (2018) 031101, http://dx.doi.org/10.1063/1.5017241.

[27] J.G. Dil, Brillouin scattering in condensed matter, Rep. Progr. Phys. 45 (3) (1982) 285, http://dx.doi.org/10.1088/0034-4885/45/3/002.

[28] M. Kuriakose, S. Raetz, N. Chigarev, S.M. Nikitin, A. Bulou, D. Gasteau, V. Tournat, B. Castagnede, A. Zerr, V.E. Gusev, Picosecond laser ultrasonics for imaging of transparent polycrystalline materials compressed to megabar pressures, Ultrasonics 69 (2016) 259–267, http://dx.doi.org/10.1016/j.ultras.2016.03.007.

[29] M. Kuriakose, S. Raetz, Q.M. Hu, S.M. Nikitin, N. Chigarev, V. Tournat, A. Bulou, A. Lomonosov, P. Djemia, V.E. Gusev, A. Zerr, Longitudinal sound velocities, elastic anisotropy, and phase transition of high-pressure cubic H_2O ice to 82 GPa, Phys. Rev. B 96 (13) (2017) 134122, http://dx.doi.org/10.1103/PhysRevB.96.134122.

[30] S. Raetz, M. Kuriakose, P. Djemia, S.M. Nikitin, N. Chigarev, V. Tournat, A. Bulou, A. Lomonosov, V.E. Gusev, A. Zerr, Elastic anisotropy and single-crystal moduli of solid argon up to 64 GPa from time-domain Brillouin scattering, Phys. Rev. B 99 (22) (2019) 224102, http://dx.doi.org/10.1103/PhysRevB.99.224102.

[31] F. Xu, P. Djemia, L. Belliard, H. Huang, B. Perrin, A. Zerr, Influence of elastic anisotropy on measured sound velocities and elastic moduli of polycrystalline cubic solids, J. Appl. Phys. 130 (3) (2021) 035903, http://dx.doi.org/10.1063/5.0053372.

[32] A. Devos, R. Côte, Strong oscillations detected by picosecond ultrasonics in silicon: Evidence for an electronic-structure effect, Phys. Rev. B 70 (12) (2004) 125208, http://dx.doi.org/10.1103/PhysRevB.70.125208.

[33] A. Devos, R. Côte, G. Caruyer, A. Lefèvre, A different way of performing picosecond ultrasonic measurements in thin transparent films based on laser-wavelength effects, Appl. Phys. Lett. 86 (21) (2005) 211903, http://dx.doi.org/10.1063/1.1929869.

[34] F. Hudert, A. Bartels, T. Dekorsy, K. Köhler, Influence of doping profiles on coherent acoustic phonon detection and generation in semiconductors, J. Appl. Phys. 104 (12) (2008) 123509, http://dx.doi.org/10.1063/1.3033140.

[35] T. Dehoux, N. Tsapis, B. Audoin, Relaxation dynamics in single polymer microcapsules probed with laser-generated GHz acoustic waves, Soft Matter 8 (9) (2012) 2586–2589, http://dx.doi.org/10.1039/C2SM07146K.

[36] M. Khafizov, J. Pakarinen, L. He, H.B. Henderson, M.V. Manuel, A.T. Nelson, B.J. Jaques, D.P. Butt, D.H. Hurley, Subsurface imaging of grain microstructure using picosecond ultrasonics, Acta Mater. 112 (2016) 209–215, http://dx.doi.org/10.1016/j.actamat.2016.04.003.

[37] Y. Wang, D.H. Hurley, Z. Hua, T. Pezeril, S. Raetz, V.E. Gusev, V. Tournat, M. Khafizov, Imaging grain microstructure in a model ceramic energy material with optically generated coherent acoustic phonons, Nature Commun. 11 (1) (2020) 1597, http://dx.doi.org/10.1038/s41467-020-15360-3, URL https://www.nature.com/articles/s41467-020-15360-3.

[38] S. La Cavera, F. Pérez-Cota, R.J. Smith, M. Clark, Phonon imaging in 3D with a fibre probe, Light Sci. Appl. 10 (1) (2021) 91, http://dx.doi.org/10.1038/s41377-021-00532-7.

[39] T. Thréard, E. de Lima Savi, S. Avanesyan, N. Chigarev, Z. Hua, V. Tournat, V.E. Gusev, D.H. Hurley, S. Raetz, Photoacoustic 3-D imaging of polycrystalline microstructure improved with transverse acoustic waves, Photoacoustics 23 (2021) 100286, http://dx.doi.org/10.1016/j.pacs.2021.100286.

[40] V.E. Gusev, T. Thréard, D.H. Hurley, S. Raetz, Time-domain Brillouin scattering theory for probe light and acoustic beams propagating at an angle and acousto-optic interaction at material interfaces, under review in Photoacoustics (2023) arXiv:2107.05294, [cond-mat, physics:physics].

[41] R.S. Weis, T.K. Gaylord, Lithium niobate: Summary of physical properties and crystal structure, Appl. Phys. A 37 (4) (1985) 191–203, http://dx.doi.org/10.1007/BF00614817.

[42] T. Goto, Y. Syono, Shock-induced phase transformation in lithium niobate, J. Appl. Phys. 58 (7) (1985) 2548–2552, http://dx.doi.org/10.1063/1.335934.

[43] D.-D. Sang, Q.-L. Wang, C. Han, K. Chen, Y.-W. Pan, Electronic and optical properties of lithium niobate under high pressure: A first-principles study, Chin. Phys. B 24 (7) (2015) 077104, http://dx.doi.org/10.1088/1674-1056/24/7/077104.

[44] M. Akaogi, Crystal chemistry, phase relations, and energetics of high-pressure ABO_3 perovskites, in: High-Pressure Silicates and Oxides, Springer Nature Singapore, Singapore, 2022, pp. 115–132, http://dx.doi.org/10.1007/978-981-19-6363-6_7, Series Title: Advances in Geological Science.

[45] T. Ishii, R. Sinmyo, T. Komabayashi, T.B. Ballaran, T. Kawazoe, N. Miyajima, K. Hirose, T. Katsura, Synthesis and crystal structure of $LiNbO_3$-type $Mg_3Al_2Si_3O_{12}$: A possible indicator of shock conditions of meteorites, Am. Mineral. 102 (9) (2017) 1947–1952, http://dx.doi.org/10.2138/am-2017-6027.

[46] M. Akaogi, T. Tajima, M. Okano, H. Kojitani, High-pressure and high-temperature phase transitions in Fe_2TiO_4 and Mg_2TiO_4 with implications for titanomagnetite inclusions in superdeep diamonds, Minerals 9 (10) (2019) 614, http://dx.doi.org/10.3390/min9100614.

[47] O. Tschauner, C. Ma, A. Lanzirotti, M.G. Newville, Riesite, a new high pressure polymorph of TiO_2 from the ries impact structure, Minerals 10 (1) (2020) 78, http://dx.doi.org/10.3390/min10010078.

[48] A. Ródenas, J.A. Sanz García, D. Jaque, G.A. Torchia, C. Mendez, I. Arias, L. Roso, F. Agulló-Rueda, Optical investigation of femtosecond laser induced microstress in neodymium doped lithium niobate crystals, J. Appl. Phys. 100 (3) (2006) 033521, http://dx.doi.org/10.1063/1.2218991.

[49] Z. Mi, S.R. Shieh, A. Kavner, B. Kiefer, H.-R. Wenk, T.S. Duffy, Strength and texture of sodium chloride to 56 GPa, J. Appl. Phys. 123 (13) (2018) 135901, http://dx.doi.org/10.1063/1.5022273.

[50] J. Kushibiki, I. Takanaga, M. Arakawa, T. Sannomiya, Accurate measurements of the acoustical physical constants of $LiNbO_3$ and $LiTaO_3$ single crystals, IEEE Trans. Ultrason. Ferroelect. Freq. Control 46 (5) (1999) 1315–1323, http://dx.doi.org/10.1109/58.796136.

[51] MolTech GmbH Molecular technology, Table of properties of $LiNbO_3$ (lithium niobate), 2023, URL http://www.mt-berlin.com/frames_ao/descriptions/lnb.htm.

[52] D.R. Lide, CRC Handbook of Chemistry and Physics, 85th Edition, CRC Press, 2004.

[53] C.-S. Zha, R.J. Hemley, S.A. Gramsch, H.-k. Mao, W.A. Bassett, Optical study of H_2O ice to 120 GPa: Dielectric function, molecular polarizability, and equation of state, J. Chem. Phys. 126 (7) (2007) 074506, http://dx.doi.org/10.1063/1.2463773.

[54] J.T. Busby, M.C. Hash, G.S. Was, The relationship between hardness and yield stress in irradiated austenitic and ferritic steels, J. Nucl. Mater. 336 (2) (2005) 267–278, http://dx.doi.org/10.1016/j.jnucmat.2004.09.024.

[55] M. Lejman, G. Vaudel, I.C. Infante, I. Chaban, T. Pezeril, M. Edely, G.F. Nataf, M. Guennou, J. Kreisel, V.E. Gusev, B. Dkhil, P. Ruello, Ultrafast acousto-optic mode conversion in optically birefringent ferroelectrics, Nature Commun. 7 (1) (2016) 12345, http://dx.doi.org/10.1038/ncomms12345.

[56] D.E. Zelmon, D.L. Small, D. Jundt, Infrared corrected Sellmeier coefficients for congruently grown lithium niobate and 5 mol. % magnesium oxide–doped lithium niobate, J. Opt. Soc. Amer. B 14 (12) (1997) 3319–3322, http://dx.doi.org/10.1364/JOSAB.14.003319.

[57] H.-N. Lin, R.J. Stoner, H.J. Maris, J. Tauc, Phonon attenuation and velocity measurements in transparent materials by picosecond acoustic interferometry, J. Appl. Phys. 69 (7) (1991) 3816–3822, http://dx.doi.org/10.1063/1.348958.

[58] S.A. Self, Focusing of spherical Gaussian beams, Appl. Opt. 22 (5) (1983) 658–661, http://dx.doi.org/10.1364/AO.22.000658.

[59] A. Polian, M. Grimsditch, Brillouin scattering from H_2O: Liquid, ice VI, and ice VII, Phys. Rev. B 27 (10) (1983) 6409–6412, http://dx.doi.org/10.1103/PhysRevB.27.6409.

[60] H.J. McSkimin, J. Andreatch, Elastic moduli of diamond as a function of pressure and temperature, J. Appl. Phys. 43 (7) (1972) 2944–2948, http://dx.doi.org/10.1063/1.1661636.

[61] Y. Hao, J. Zhu, L. Zhang, J. Qu, H. Ren, First-principles study of high pressure structure phase transition and elastic properties of titanium, Solid State Sci. 12 (8) (2010) 1473–1479, http://dx.doi.org/10.1016/j.solidstatesciences.2010.06.010.

[62] M.I. Eremets, V.V. Struzhkin, J.A. Timofeev, I.A. Trojan, A.N. Utjuzh, A.M. Shirokov, Refractive index of diamond under pressure, High Pressure Res. 9 (1–6) (1992) 347–350, http://dx.doi.org/10.1080/08957959208245659.

[63] Q. Cridling, R. Charriere, D. Jamon, M. Lenci, M. Pedeferri, D. Delafosse, Anodized titanium oxide thickness estimation with ellipsometry, reflectance spectra extrema positions and electronic imaging: importance of the interfaces electromagnetic phase-shift, Thin Solid Films 709 (2020) 138181, http://dx.doi.org/10.1016/j.tsf.2020.138181.

[64] H. Shimizu, T. Nabetani, T. Nishiba, S. Sasaki, High-pressure elastic properties of the VI and VII phase of ice in dense H_2O and D_2O, Phys. Rev. B 53 (10) (1996) 6107–6110, http://dx.doi.org/10.1103/PhysRevB.53.6107.

[65] J.a.H. da Jornada, S. Block, F.A. Mauer, G.J. Piermarini, Phase transition and compression of $LiNbO_3$ under static high pressure, J. Appl. Phys. 57 (3) (1985) 842–844, http://dx.doi.org/10.1063/1.334682.

[66] O. Matsuda, O. Wright, Laser picosecond acoustics in a two-layer structure with oblique probe light incidence, Ultrasonics 42 (1) (2004) 653–656, http://dx.doi.org/10.1016/j.ultras.2004.01.052, Proceedings of Ultrasonics International 2003.

[67] T. Dehoux, N. Chigarev, C. Rossignol, B. Audoin, Three-dimensional elasto-optical interaction for reflectometric detection of diffracted acoustic fields in picosecond ultrasonics, Phys. Rev. B 76 (2007) 024311, http://dx.doi.org/10.1103/PhysRevB.76.024311.

[68] M. Abramowitz, I.A. Stegun, Handbook of Mathematical Functions: with Formulas, Graphs, and Mathematical Tables, Courier Corporation, 1965.

[69] M. Newville, R. Otten, A. Nelson, T. Stensitzki, A. Ingargiola, D. Allan, A. Fox, F. Carter, Michał, R. Osborn, D. Pustakhod, lneuhaus, S. Weigand, A. Aristov, Glenn, C. Deil, Mark, A.L.R. Hansen, G. Pasquevich, L. Foks, N. Zobrist, O. Frost, Stuermer, azelcer, A. Polloreno, A. Persaud, J.H. Nielsen, M. Pompili, S. Caldwell, A. Hahn, lmfit/lmfit-py: 1.1.0, 2022, http://dx.doi.org/10.5281/zenodo.7370358.

[70] A. Dewaele, V. Stutzmann, J. Bouchet, F. Bottin, F. Occelli, M. Mezouar, High pressure-temperature phase diagram and equation of state of titanium, Phys. Rev. B 91 (2015) 134108, http://dx.doi.org/10.1103/PhysRevB.91.134108.

[71] O.B. Wright, T. Hyoguchi, Ultrafast vibration and laser acoustics in thin transparent films, Opt. Lett. 16 (19) (1991) 1529–1531, http://dx.doi.org/10.1364/OL.16.001529.

[72] O.B. Wright, Thickness and sound velocity measurement in thin transparent films with laser picosecond acoustics, J. Appl. Phys. 71 (4) (1992) 1617–1629, http://dx.doi.org/10.1063/1.351218.

[73] A.M. Lomonosov, A. Ayouch, P. Ruello, G. Vaudel, M.R. Baklanov, P. Verdonck, L. Zhao, V.E. Gusev, Nanoscale noncontact subsurface investigations of mechanical and optical properties of nanoporous low-k material thin film, ACS Nano 6 (2) (2012) 1410–1415, http://dx.doi.org/10.1021/nn204210u, PMID: 22211667.

[74] A. Devos, Colored ultrafast acoustics: From fundamentals to applications, Ultrasonics 56 (2015) 90–97, http://dx.doi.org/10.1016/j.ultras.2014.02.009.

[75] O.B. Wright, B. Perrin, O. Matsuda, V.E. Gusev, Ultrafast carrier diffusion in gallium arsenide probed with picosecond acoustic pulses, Phys. Rev. B 64 (2001) 081202, http://dx.doi.org/10.1103/PhysRevB.64.081202.

[76] A.V. Scherbakov, M. Bombeck, J.V. Jäger, A.S. Salasyuk, T.L. Linnik, V.E. Gusev, D.R. Yakovlev, A.V. Akimov, M. Bayer, Picosecond opto-acoustic interferometry and polarimetry in high-index GaAs, Opt. Express 21 (14) (2013) 16473–16485, http://dx.doi.org/10.1364/OE.21.016473.

[77] S. Sandeep, S. Raetz, J. Wolfman, B. Negulescu, G. Liu, J.-L. Longuet, T. Thréard, V.E. Gusev, Evaluation of optical and acoustical properties of $Ba_{1-x}Sr_xTiO_3$ thin film material library via conjugation of picosecond laser ultrasonics with X-ray diffraction, energy dispersive spectroscopy, electron probe micro analysis, scanning electron and atomic force microscopies, Nanomaterials 11 (11) (2021) http://dx.doi.org/10.3390/nano11113131.

[78] K.E. O'Hara, X. Hu, D.G. Cahill, Characterization of nanostructured metal films by picosecond acoustics and interferometry, J. Appl. Phys. 90 (9) (2001) 4852–4858, http://dx.doi.org/10.1063/1.1406543.

[79] V.É. Gusev, A.A. Karabutov, Laser Optoacoustics, American Inst. of Physics, 1993.

[80] P. Ruello, V.E. Gusev, Physical mechanisms of coherent acoustic phonons generation by ultrafast laser action, Ultrasonics 56 (2015) 21–35, http://dx.doi.org/10.1016/j.ultras.2014.06.004.

[81] D. Brick, E. Emre, M. Grossmann, T. Dekorsy, M. Hettich, Picosecond photoacoustic metrology of SiO_2 and $LiNbO_3$ layer systems used for high frequency surface-acoustic-wave filters, Appl. Sci. 7 (8) (2017) http://dx.doi.org/10.3390/app7080822.

[82] H.-Y. Hao, H.J. Maris, Experiments with acoustic solitons in crystalline solids, Phys. Rev. B 64 (2001) 064302, http://dx.doi.org/10.1103/PhysRevB.64.064302.

[83] A.V. Scherbakov, A.S. Salasyuk, A.V. Akimov, X. Liu, M. Bombeck, C. Brüggemann, D.R. Yakovlev, V.F. Sapega, J.K. Furdyna, M. Bayer, Coherent magnetization precession in ferromagnetic (Ga,Mn)As induced by picosecond acoustic pulses, Phys. Rev. Lett. 105 (2010) 117204, http://dx.doi.org/10.1103/PhysRevLett.105.117204.

[84] A.V. Akimov, A.V. Scherbakov, D.R. Yakovlev, C.T. Foxon, M. Bayer, Ultrafast band-gap shift induced by a strain pulse in semiconductor heterostructures, Phys. Rev. Lett. 97 (2006) 037401, http://dx.doi.org/10.1103/PhysRevLett.97.037401.

[85] I.-J. Chen, P.-A. Mante, C.-K. Chang, S.-C. Yang, H.-Y. Chen, Y.-R. Huang, L.-C. Chen, K.-H. Chen, V. Gusev, C.-K. Sun, Graphene-to-substrate energy transfer through out-of-plane longitudinal acoustic phonons, Nano Lett. 14 (3) (2014) 1317–1323, http://dx.doi.org/10.1021/nl404297r, PMID: 24559107.

[86] C. Thomsen, J. Strait, Z. Vardeny, H.J. Maris, J. Tauc, J.J. Hauser, Coherent phonon generation and detection by picosecond light pulses, Phys. Rev. Lett. 53 (1984) 989–992, http://dx.doi.org/10.1103/PhysRevLett.53.989.

[87] V. Gusev, Laser hypersonics in fundamental and applied research, Acustica 82 (1996) S37–S45.

[88] O. Matsuda, M.C. Larciprete, R. Li Voti, O.B. Wright, Fundamentals of picosecond laser ultrasonics, Ultrasonics 56 (2015) 3–20, http://dx.doi.org/10.1016/j.ultras.2014.06.005.

[89] F. Yang, T.J. Grimsley, S. Che, G.A. Antonelli, H.J. Maris, A.V. Nurmikko, Picosecond ultrasonic experiments with water and its application to the measurement of nanostructures, J. Appl. Phys. 107 (10) (2010) 103537, http://dx.doi.org/10.1063/1.3388283.

[90] C. Rossignol, J.M. Rampnoux, M. Perton, B. Audoin, S. Dilhaire, Generation and detection of shear acoustic waves in metal submicrometric films with ultrashort laser pulses, Phys. Rev. Lett. 94 (2005) 166106, http://dx.doi.org/10.1103/PhysRevLett.94.166106.

[91] S. Zhang, E. Péronne, L. Belliard, S. Vincent, B. Perrin, Three-dimensional acoustic wavefront imaging in anisotropic systems by picosecond acoustics, J. Appl. Phys. 109 (3) (2011) 033507, http://dx.doi.org/10.1063/1.3532034.

[92] C. Jean, L. Belliard, T.W. Cornelius, O. Thomas, Y. Pennec, M. Cassinelli, M.E. Toimil-Molares, B. Perrin, Spatiotemporal imaging of the acoustic field emitted by a single copper nanowire, Nano Lett. 16 (10) (2016) 6592–6598, http://dx.doi.org/10.1021/acs.nanolett.6b03260, PMID: 27657670.

[93] E. Wolanin, P. Pruzan, J.C. Chervin, B. Canny, M. Gauthier, D. Häusermann, M. Hanfland, Equation of state of ice VII up to 106 GPa, Phys. Rev. B 56 (10) (1997) 5781–5785, http://dx.doi.org/10.1103/PhysRevB.56.5781.

[94] P. Virtanen, R. Gommers, T.E. Oliphant, M. Haberland, T. Reddy, D. Cournapeau, E. Burovski, P. Peterson, W. Weckesser, J. Bright, S.J. van der Walt, M. Brett, J. Wilson, K.J. Millman, N. Mayorov, A.R.J. Nelson, E. Jones, R. Kern, E. Larson, C.J. Carey, İ. Polat, Y. Feng, E.W. Moore, J. VanderPlas, D. Laxalde, J. Perktold, R. Cimrman, I. Henriksen, E.A. Quintero, C.R. Harris, A.M. Archibald, A.H. Ribeiro, F. Pedregosa, P. van Mulbregt, A. Vijaykumar, A.P. Bardelli, A. Rothberg, A. Hilboll, A. Kloeckner, A. Scopatz, A. Lee, A. Rokem, C.N. Woods, C. Fulton, C. Masson, C. Häggström, C. Fitzgerald, D.A. Nicholson, D.R. Hagen, D.V. Pasechnik, E. Olivetti, E. Martin, E. Wieser, F. Silva, F. Lenders, F. Wilhelm, G. Young, G.A. Price, G.-L. Ingold, G.E. Allen, G.R. Lee, H. Audren, I. Probst, J.P. Dietrich, J. Silterra, J.T. Webber, J. Slavič, J. Nothman, J. Buchner, J. Kulick, J.L. Schönberger, J. de Miranda Cardoso, J. Reimer, J. Harrington, J.L.C. Rodríguez, J. Nunez-Iglesias, J. Kuczynski, K. Tritz, M. Thoma, M. Newville, M. Kümmerer, M. Bolingbroke, M. Tartre, M. Pak, N.J. Smith, N. Nowaczyk, N. Shebanov, O. Pavlyk, P.A. Brodtkorb, P. Lee, R.T. McGibbon, R. Feldbauer, S. Lewis, S. Tygier, S. Sievert, S. Vigna, S. Peterson, S. More, T. Pudlik, T. Oshima, T.J. Pingel, T.P. Robitaille, T. Spura, T.R. Jones, T. Cera, T. Leslie, T. Zito, T. Krauss, U. Upadhyay, Y.O. Halchenko, Y. Vázquez-Baeza, SciPy 1. 0 Contributors, SciPy 1.0: fundamental algorithms for scientific computing in Python, Nature Methods 17 (3) (2020) 261–272, http://dx.doi.org/10.1038/s41592-019-0686-2.

[95] H. Shimizu, M. Ohnishi, S. Sasaki, Y. Ishibashi, Cauchy relation in dense H_2O ice VII, Phys. Rev. Lett. 74 (14) (1995) 2820–2823, http://dx.doi.org/10.1103/PhysRevLett.74.2820.

[96] M.I. Eremets, M.I. Eremets, High Pressure Experimental Methods, Oxford University Press, Oxford, New York, 1996.

[97] M. Somayazulu, J. Shu, C.-s. Zha, A.F. Goncharov, O. Tschauner, H.-k. Mao, R.J. Hemley, In situ high-pressure x-ray diffraction study of H2O ice VII, J. Chem. Phys. 128 (6) (2008) 064510, http://dx.doi.org/10.1063/1.2813890.

Sathyan Sandeep obtained his Ph.D. in Physics in 2019 from the Indian Institute of Science Education and Research (IISER) Thiruvananthapuram, India, specializing in picosecond acoustic studies of semiconductor nano-cavities. He holds a Master's degree in Physics from the Indian Institute of Technology (IIT), Madras, India. Since 2019, he has been a postdoctoral researcher at the Le Mans University, France, focusing on nano- to microscale imaging of polycrystalline materials and material transformations using time-domain Brillouin scattering (TDBS). Additionally, he investigates the mechanical properties of single carbon fiber using picosecond ultrasonics.

Email: sandeep.sathyan@univ-lemans.fr.

Samuel Raetz received his Ph.D. degree in mechanics (physical acoustics) in 2012 from Bordeaux University, France. He is currently an Associate Professor at Le Mans University. Since 2009, his research interests were focused on the applications of laser ultrasonics. His most recent research has focused on applications of picosecond acoustic (especially time-domain Brillouin scattering) for non-destructive testing/evaluation (NDT&E) of polycrystalline materials and microstructures. He is also working on the NDT&E of composite materials, bonding structures, fatigued and cracked materials using guided elastic waves with a particular focused on zero-group-velocity Lamb modes.

Email: samuel.raetz@univ-lemans.fr.

Nikolay Chigarev is a research engineer in the Acoustic laboratory of university of Le Mans, France. After the defending of Ph.D. thesis in laser physics (1998, Lomonosov Moscow State University), he has worked at several post-doctoral positions in France (2003–2007) and USA (1999, 2002). During his scientific work he has published about 55 articles in scientific journals and 25 articles in the proceedings of conferences. His area of scientific research is linear and nonlinear opto-acoustics with pulsed and modulated continues wave lasers.

Email: Nikolay.Chigarev@univ-lemans.fr.

Nicolas Pajusco has been a Ph.D. student since 2022 in acoustics at Le Mans University. He received his M.S. degree in wave physics and acoustics at the Institute d'Acoustique—Graduate School of Le Mans University in 2022, where he studied guided waves in anisotropic media. His main focus is on nanoscale imaging using time-domain Brillouin scattering.

Email: nicolas.pajusco@univ-lemans.fr.

Théo Thréard received his Ph. D. degree in Acoustics in 2021 from Le Mans University, France. His thesis focuses on the development of experimental and signal processing methods for 3-D imaging of transparent materials at the nanoscale via time-domain Brillouin scattering (TDBS). He is currently working on hydro-acoustic topics for the french ministry of army.

Email: threard.theo@gmail.com.

Mathieu Edely received his Ph.D. degree in physics in 2016 from Le Mans University. He is currently a Research Engineer at Le Mans University. He has developed expertise in materials science, including the production of thin films by physical vapor deposition techniques and surface nanostructuring using atomic force microscopy. His research interests is focused on enhanced spectroscopies and biomolecular interaction.

Email: mathieu.edely@univ-lemans.fr.

Alain Bulou received his Ph.D degree in Solid State Physics in 1979, and State Ph.D in 1985 from University Pierre and Marie Curie, Paris (France). He was CNRS researcher, research fellow at Los Alamos National Laboratory (USA), and, since 1993, a professor at Le Mans University (France). His research background, in material science, was mainly devoted to structural phase transitions (temperature/pressure), symmetry breaking, lattice dynamics, and vibrational spectroscopies (neutrons, Raman). He is currently emeritus professor at Le Mans University.

Email: alain.bulou@univ-lemans.fr.

Andreas Zerr received his doctorate of natural sciences from Johannes Gutenberg University of Mainz (Germany) in 1995 and Habilitation in Science and Engineering from Sorbonne Paris North University (France) in 2020. He is currently a CNRS researcher at Process and Material Sciences Laboratory (LSPM, Villetaneuse, France). He studies chemical and physical behavior of condensed matter at high pressures and temperatures using different techniques including diamond anvil cells and CW- or pulsed laser radiation. He explores paths for the synthesis of novel advanced compounds and develops approaches aiming detailed examination of mechanical and optoelectronic properties of solids in-situ and of the novel compound after recovery at ambient conditions.

Email: zerr@univ-paris13.fr.

Vitalyi E. Gusev received his Ph.D. degree in physics and mathematics (laser physics) in 1982 from M. V. Lomonosov Moscow State University, Russia. He received Habilitations in Moscow State University in mathematics and physics (acoustics) in 1992 and in Le Mans University, France, in 1997. He is currently a Professor at Le Mans University. Since 1980, his research interests were in the development of the theoretical foundations of nonlinear acoustic, optoacoustic, photothermal and thermoacoustic phenomena. His most recent research has focused on applications of time-domain Brillouin scattering for imaging, on nonlinear laser ultrasonics, acoustics of granular media and nondestructive testing and evaluation of nanomaterials and nanostructures.

Email: vitali.goussev@univ-lemans.fr.